Physik Department

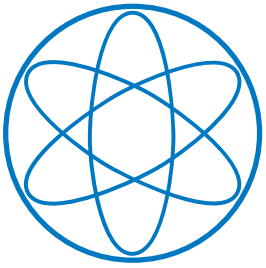

Production of ultracold neutrons in superfluid helium under pressure

Philipp Anton Schmidt-Wellenburg

Technische Universität München

Fakultät für Physik der Technischen Universität München

Physik Department E18

Production of ultracold neutrons in superfluid helium under pressure

Philipp Anton Schmidt-Wellenburg

Vollständiger Abdruck der von der Fakultät für Physik der Technischen Universität München zur Erlangung des akademischen Grades eines

Doktors der Naturwissenschaften (Dr. rer. nat.)

genehmigten Dissertation.

Vorsitzender: Univ.-Prof. Dr. A. J. Buras

Prüfer der Dissertation:

1. Univ.-Prof. Dr. O. Zimmer

2. Univ.-Prof. Dr. K. Schreckenbach

Die Dissertation wurde am 15. Januar 2009 bei der Technischen Universität München eingereicht und durch die Fakultät für Physik am 05. März 2009 angenommen.

Pour Stéphanie

Contents

1 Introduction **1**

2 Theory and phenomenology **4**
2.1 Ultracold neutrons and their properties 4
2.2 From fast neutrons to ultracold neutrons 8
2.3 UCN production in superfluid helium 10
2.3.1 Superfluid helium - phenomenology and terminology . 10
2.3.2 Ultracold neutrons from inelastic scattering on superfluid Helium 13
2.3.3 Up-scattering of UCN 16

3 Calculations of UCN production rates from inelastic neutron scattering **20**
3.1 Inelastic neutron scattering 20
3.1.1 Measuring the dynamic structure factor *S(q,E)* 21
3.1.2 Time-of-flight neutron inelastic scattering 21
3.2 Pressure Dependence of the Dynamic Scattering Function . . . 23
3.3 Pressure Dependence of the UCN Production Rate 25
3.4 Temperature Dependence of Multiphonon Scattering 32
3.5 Up-scattering 33

4 A versatile cryostat to investigate UCN production **36**
4.1 Cooling a large volume of He-II 36
4.2 The cryogenic apparatus 37
4.3 Operation 41

5 Experiments on the extraction of UCN from superfluid helium **49**
5.1 Experimental setup 49
5.2 Measurements 50
5.3 Data analysis 57
5.3.1 Time constants 57
5.3.2 Continuous and build-up measurements 58
5.3.3 Change of lossrate with holding time 61
5.3.4 Temperature dependence of the storage time 61

5.3.5 Production rate and extraction efficiency 62
5.3.6 Comparison with calculated UCN production rate . . . 65
5.4 Comparison with stainless steel converter vessel 66
5.5 Discussion 67

6 UCN Production in Helium Under Pressure 68
6.1 Experimental method and setup 68
6.1.1 Overview of the setup 69
6.1.2 PF1b – an intense source of cold neutrons 69
6.1.3 The neutron velocity selector 71
6.1.4 Conversion volume 74
6.1.5 UCN extraction line 74
6.1.6 Time-of-Flight setup 76
6.1.7 Neutron detector and monitors 76
6.2 Measurement 80
6.2.1 Beam profile measurements 80
6.2.2 Gold foil activation 80
6.2.3 Time-of-flight measurement 83
6.2.4 Weather of the converter vessel 83
6.2.5 UCN production rate measurements 83
6.2.6 Control measurements at SVP 87
6.2.7 Measurement of time constants and background 89
6.3 Data Analysis 90
6.3.1 Background 90
6.3.2 Temporal decrease of UCN count rates 92
6.3.3 Conversion from time-of-flight to wavelength 95
6.3.4 Cold neutron spectrum inside the converter volume . . 96
6.3.5 UCN conversion rates in superfluid helium under pressure 97
6.3.6 Comparison with UCN production rates calculated from inelastic scattering data 99
6.4 Discussion 102

7 Implementation of a new UCN source at the ILL 104
7.1 A UCN source for GRANIT and maybe more 104
7.2 Source concept 105
7.2.1 Neutron monochromator 105
7.2.2 Secondary neutron guide, UCN converter and cryostat 108
7.2.3 UCN selection with semidiffuse channel 110
7.3 Outlook 111

8 Summary and outlook 113

Abstract

The goal of this work was to further develop techniques for the production of ultracold neutrons using superfluid helium. This included experiments at the "Neutronenquelle Heinz-Maier-Leibnitz" as well as at the Institut Laue Langevin. UCN produced in a fomblin coated vessel filled with superfluid helium were extracted to the vacuum with an efficiency of close to 50%. In a further step I looked into the properties of UCN production using superfluid helium under pressure ($\leq$ 20 bar) as converter. Results from calculations of the pressure dependent differential UCN production rate, based on inelastic neutron scattering data, agree very well with measurements made directly on the cold neutron beam PF1b at the Institut Laue Langevin. An increase in production rate, compared to UCN converters with superfluid helium at saturated vapour pressure, was not found.

Acknowledgements

It is a pleasure to thank the people who have made this work possible.

In particular I would like to thank my supervisor, Professor Oliver Zimmer who has provided support, enthusiasm and encouragement for my work. I was also fortunate to have had the opportunity to work with Dr. P. Geltenbort, Professor C. Plonka-Spehr, and Dr. V.V. Nesvizhevsky.

I am grateful to Dr. Ken H. Andersen, who had always an open door, for all the discussions and advise on neutron scattering techniques.

I am indebted to my colleagues M. Fertl, K. Leung and S. Mironov, who have invested lot of time in this work before, during or after measurements.

Without the technical support from D. Berruyer and T. Brenner most of the experimental work would have been impossible.

For the much needed proof-reading I am very grateful to Torsten Soldner; but also for his excellence advise, support, and encouragement.

My wife and my son gave me often the strongly needed moral support, as did Jochen Krempel my office mate. Thanks also to my parents for their unfailing encouragement.

Chapter 1

Introduction

In 1908 Heike Kamerlingh-Onnes liquefied for the first time ^{4}He in his laboratory at the University of Leiden. In the following years his group dominated entirely low-temperature physics and also discovered the λ-transition to the superfluid phase. Although H. Kammerlingh-Onnes and L. J. Dana did measure the anomalous increase in specific heat at about 2 K already in the 1920's they did not believe in their data. Only in 1932 W. H. Keesom and K. Clusius did believe in their measurements and realized that a phase transition occurs at 2.17 K. The characteristic λ-shape of the specific heat maximum at this temperature gives the name to this transition point.
Nearly 40 years after the discovery of the λ-transition R. Golub and J. M. Pendlebury [Gol75] developed ideas based on superfluid helium (He-II) for the production of ultracold neutrons (UCN). The characteristic phonon dispersion curve of superfluid helium provides an ideal two-level system for superthermal cooling. An incident neutron excites a phonon in the liquid and thus looses all its energy and momentum, whereas the inverse process is thermally surpressed. First attempts in the 1970's and 1980's [Age78, Kil87] to use this technique were not very successful, as the extraction from the converter to the detector posed problems. At the same time Steyerl developed a phase space transforming UCN turbine [Ste75] which was then installed on the level D [Ste86] of the research reactor at the Institut Laue Langevin. These developments were the base of a long tradition of fundamental research with ultracold neutrons at the Institut Laue Langevin. The two most prominent kinds of experiments performed here are the search for an electric dipole moment of the neutron [Bak06] and precision measurements of the neutron lifetime [Arz00, Ser05]. In the last ten years UCN also were used to show quantised energy states of neutrons in the earth gravitational field, an experimental technique which might become important in the search for deviations from gravity or in the quest for additional short range forces [Nes02].

In recent years several institutes around the world have developed or are still developing new UCN sources. The most promising concepts for new

sources, superfluid helium [Mas02, Bak03] and solid deuterium [Liu98, Tri00, Sau04, Atc05a, Fre07], have been used. The ILL will have to work hard to maintain its exceptional position in science with UCN. The work of this PhD thesis was dedicated to further develop techniques of UCN production for a new generation UCN source at the ILL. In Chapter 2 I give a brief overview of properties of UCN and will discuss more thoroughly UCN production with superfluid helium.

A prototype cryostat, described in Chapter 4, was developed to investigate UCN production and the extraction of UCN to vacuum. In two experiments at the "Neutronenquelle Heinz Maier-Leibnitz" in Garching, Germany, we produced and efficiently extracted UCN to vacuum. The second of these experiment is described in Chapter 5. An efficient extraction to vacuum opens the door to use superfluid helium as source medium and still performe precision experiments in vacuum and at room temperature.

Motivated by the pressure dependence of the properties of He-II, in particular its dispersion curve and density, we developed the idea to investigate in detail UCN production in superfluid helium under pressure. Applying pressure to He-II increases the velocity of sound, such that the dispersion curves of He-II and of the free neutron cross at shorter neutron wavelength. For neutron beams from a neutron guide coupled to a liquid deuterium cold source, the differential flux density $\mathrm{d}\Phi/\mathrm{d}\lambda$ in the range 8Å$-$9 Å normally increases for decreasing wavelength. The density of He-II also increases with pressure. These two facts may lead to the expectation that the single phonon UCN production increases with pressure. Furthermore, the multiphonon contributions might be favourably affected by applying pressure. In Chapter 3 I investigate in detail, using inelastic scattering data measured by Gibbs and colleagues [Gib96], the UCN production in superfluid helium under pressure. Additionally, I derive an analytical expression [Sch08b] to predict UCN production rates for any kind of incident cold neutron spectrum.

The wavelength resolved UCN production rate of a superfluid helium converter under pressure was then directly measured in late Summer 2008 on the intense neutron beam for fundamental physics, PF1b, of the Institut Laue Langevin. In the preparations to the experiment the prototype cryostat was modified to meet the requirements posed by pressure. The experimental setup, the measurements, and their analysis are described in Chapter 6. Already during the experimental run it became clear that the intensity of the single phonon peak decreases and that it moves to shorter wavelength for increasing pressure, a behaviour expected from the analysis of the inelastic neutron scattering data.

This research is related to the development of a dedicated UCN source for the new gravitational UCN spectrometer, GRANIT [Nes06]. Further developments, described in Chapter 7, were made to provide a monochromatic 8.9Å neutron beam for an UCN source based on the prototype cryostat and

to optimise the connection between source and spectrometer. In particular a monochromator for the 8.9Å beam was developed and a loss free UCN collimation technique was pioneered for the interface source-spectrometer. These developments are included into the design of the dedicated source, scheduled to start operation in March 2009.

Chapter 2

Theory and phenomenology of UCN production in superfluid helium

In this chapter the properties of neutrons and their interactions with materials and fields are discussed. A special focus will be on the scattering of neutrons from superfluid helium and the resulting UCN production rates. A more comprehensive depiction can be found in books on neutron scattering, e.g. [Lov84, Ign90, Gol91] but also in H. Glydes book on excitations in solid and liquid helium [Gly95].

2.1 Ultracold neutrons and their properties

After the discovery of the free neutron by Chadwick in 1932 it took over 30 years until neutrons were stored in material bottles for the first time. These neutrons with energies in the range of some hundreds neV, which are reflected under any incident angle, are referred to as ultracold neutrons (UCN). It was Zeldovich [Zel59] in 1959 who, after the observation of neutrons reflected under small gracing angles, first put the idea to paper. But it took another 10 years until first UCN were extracted from reactor cores, both in Dubna by the group of F.L. Shapiro [Lus69] and in Munich by A. Steyerl [Ste69]. Today, UCN are a widely used tool in particle physics, for example in the search of the neutron electric dipole moment and a more precise determination of the neutron lifetime.

Neutrons are often distinguished by temperatures (see Tab. 2.1), which refer to the temperature of the moderator. Different though for the term ultracold, it is used for any neutron whose energy is low enough to be totally reflected

under any incident angle from a material surface. As kinetic energies are a factor 10^{-6} smaller as for cold neutrons (meV) gravitation plays a more pronounced role in experiments. An ultracold neutron with $E_{\mathrm{kin}} = 100$ neV can rise about one meter in the earth gravitational field. For completion I will briefly describe the most important properties of ultracold neutrons.

Weak interaction

The weak interaction is responsible for the finite lifetime of the neutron. A free neutron decays by the reaction

$$\mathrm{n} \longrightarrow \mathrm{p} + \mathrm{e} + \bar{\nu} \tag{2.1}$$

with a decay energy of 782 keV and a decay time of $\tau_{\mathrm{n}} = 885.7 \pm 0.8$ s [Yao06]. The combination of the neutron lifetime, the correlation coefficient A (describing the beta asymmetry in neutron decay), and the Fermi weak coupling constant G_{F} gives a value for the up-down quark mixing matrix element V_{ud} in the Cabbibo-Kobayashi-Maskawa (CKM) matrix. This opens the door to a non-nuclear check of the unitarity of the first row of the CKM matrix. The neutron lifetime is also of interest as important parameter for astrophysical calculations of primordial abundances of ^{4}He and other light elements.

Magnetic interaction

In a magnetic field $\boldsymbol{B}$ the motion of a neutron can be described with the coupled equation:

$$\frac{\mathrm{d}^2\boldsymbol{r}}{\mathrm{d}t^2} = -\frac{\mu_{\mathrm{n}}}{m_{\mathrm{n}}} \nabla \left(\boldsymbol{\sigma}_{\mathrm{n}} \cdot \boldsymbol{B}\right), \tag{2.2}$$

with the magnetic moment $\mu_{\mathrm{n}} = 1.91304273(45)\mu_{\mathrm{N}} \approx -60.3$ neV/T and a mass $m_{\mathrm{n}} = 939.565360(81)$ [Yao06]. Therefore the force on the neutron depends on the field gradient and the projection of the spin vector $\boldsymbol{\sigma}_{\mathrm{n}}$ on the applied magnetic field. For an ultracold neutron moving in a static magnetic field we are generally in the adiabatic limit:

$$\left|\frac{1}{\boldsymbol{B}}\right| \cdot \left|\frac{\mathrm{d}\boldsymbol{B}}{\mathrm{d}t}\right| \ll \omega_{\mathrm{L}} = \frac{|\mu_{\mathrm{n}}\boldsymbol{B}|}{\hbar}, \tag{2.3}$$

the time dependence of the field seen by the moving neutron is much slower then the Lamor precession frequency. In this case the orientation of $\boldsymbol{\mu}_{\mathrm{n}}$ is

parallel or antiparallel to the applied field. The force acting on a neutron in the adiabatic limit is

$$\boldsymbol{F} = -\nabla\mu_{\mathrm{n}} |\boldsymbol{B}| = \pm\mu_{\mathrm{n}}\nabla |\boldsymbol{B}|, \tag{2.4}$$

where a field of 1 T corresponds to a potential energy of 60.3 neV. The equation of motion is simplified to

$$\frac{\mathrm{d}^2\boldsymbol{r}}{\mathrm{d}t^2} = \pm\frac{\mu_{\mathrm{n}}}{m_{\mathrm{n}}}\nabla |\boldsymbol{B}|. \tag{2.5}$$

Gravity

Gravity acts on any particle, nevertheless it is often neglected in high energy physics as the interaction plays only a very minor role. Having only velocities of some meters per second the effect on ultracold neutrons is more pronounced then on faster particles. The potential of a neutron at height h is

$$V_{\mathrm{G}} = m_{\mathrm{n}}gh \approx 102 \text{ neV/m} \cdot h, \tag{2.6}$$

where $g \approx 9.8\mathrm{m/s}^2$ is the gravitational acceleration on the earth's surface. A neutron falling 1 m in the earth gravitational field will gain 102 neV. This is often used to increase the transmission through thin aluminium foils in front of UCN detectors.

Interaction with matter – neutron optics

The strong interaction is responsible for interactions of neutrons with protons or heavier nuclei. The basic system to describe the interaction of a neutron with matter via strong interaction is the scattering of the neutron from a sole nucleus. The force between a nucleus and a slow neutron ($E_{\mathrm{kin}} \leq 25$ meV) can be represented approximately by a square well potential with a depth of $V_0 \approx 40$ MeV and a radius of $r \approx 2A^{1/3}$ fm, where A is the number of nucleons. Therefore, the perturbed wavelength of the incident neutron is very different in the proximity of the nucleus and a solution of the scattering problem with perturbation techniques is impossible. Fortunately, the wavefunction outside the direct interaction region is only slightly disturbed. This allows one to reformulate and solve the problem in perturbation theory with an equivalent potential:

$$U_{\mathrm{F}}(\boldsymbol{r}) = \frac{2\pi\hbar^2}{m_{\mathrm{n}}}a\delta(\boldsymbol{r}), \tag{2.7}$$

where a is the unbound scattering length of the nucleus. In neutron physics it is customary to use this pseudo potential with experimentally measured values of a to calculate scattering events.

The concept of neutron optics elucidates nicely the phenomenological principles of matter–neutron interaction, where matter can be considered as a spatially extended collection of many nuclei. An optical description of particle motion in medium can be used in the range of de Broglie wavelength with amplitudes where the state of the medium is unchanged. In these cases the wavefunction of the neutron is determined by a one-body Schrödinger equation:

$$\left(\frac{-\hbar^2}{2m_{\mathrm{n}}}\Delta + V_{\mathrm{opt}}(\boldsymbol{r})\right)\psi(\boldsymbol{r}) = E\psi(\boldsymbol{r}), \tag{2.8}$$

where $\psi(\boldsymbol{r})$ is the coherent wave and $V_{\mathrm{opt}}(\boldsymbol{r})$ the optical potential. In general the potential is energy independent and can be approximated by:

$$V_{\mathrm{opt}} = \frac{2\pi\hbar^2}{m_{\mathrm{n}}}\sum_i N_i b_i, \tag{2.9}$$

where b_i is the bound coherent scattering length, and N_i the number density of the isotope i in the medium. This potential is the volume average of the pseudo potential in Eq.(2.7). Analogously, one can describe spin-dependent contributions from magnetic interaction of the neutron magnetic moment with magnetic fields. The effect of this potential on the neutron is that inside the medium the neutron will have a changed wave vector $\boldsymbol{k'}$. One can therefore define a neutron index of refraction as in light optics by the relative change in the magnitudes of the wave vectors $n = k'/k$. Conservation of energy determines the relation to the optical potential:

$$n^2 = 1 - \frac{V_{\mathrm{opt}}}{E}. \tag{2.10}$$

In contrast to light optics the neutron index of refraction for most materials is smaller than one. Thus, a neutron can be totally reflected on the external boundary of a material–vacuum interface, a property used in neutron guides. Furthermore neutrons with kinetic energies below the optical potential are reflected under all incident angles (UCN). Such neutrons can be trapped inside material bottles. Only evanescent waves will penetrate into the confining medium. This brief interaction together with the absorption cross section of most elements leads to an absorption probability per reflection η in both, guides and storage volumes.

Today neutrons are stored for several hundred seconds, using traps from

	T [K]	λ [Å]	v [m/s]	E [meV]
thermal	300	1.8	2200	25
cold	$0.6 \leq T < 300$	$1.8 < \lambda \leq 40$	$100 \leq v < 2200$	$0.05 < E \leq 25$
very cold	$0.002 \leq T < 0.6$	$40 < \lambda \leq 564$	$7 \leq v < 100$	$0.3 \cdot 10^{-3} \leq 0.5$
ultracold	< 0.002	> 564	< 7	$\leq 300 \cdot 10^{-6}$

Table 2.1: Neutrons from a fission reaction have much higher energies and have to be moderated to thermal and cold energies. After moderation the velocity spectrum resembles a Maxwellian at slightly higher temperature as the moderator temperature T. This shift arrises from the finite interaction time with the moderator limited by absorption, neutron life time, and finite geometric source size. There is no efficient thermal moderation process for very cold and ultracold neutrons as wavelengths of the neutrons exceed the interparticle distance of the moderator. Furthermore the finite lifetime due to absorption limits the interaction time with a potential moderator.

materials with very small absorption cross sections or by replacing the "optical potential" by a magnetic field gradient acting on the magnetic moment (see magnetic interaction). The possibility of making measurements on a gas-like neutron ensemble in a closed bottle, for extended observation times, is a great advantage in the quest for a more accurate determination of the neutron life time and the search for a neutron electric dipole moment.

2.2 From fast neutrons to ultracold neutrons

In a fission reaction of a research reactor a neutron is absorbed by a uranium–235 nucleus. The nucleus enters a highly excited state before it disintegrates into medium heavy nuclei and up to six fast neutrons. In average 2.5 neutrons are liberated in each reaction. One is used to sustain the chain reaction, 0.5 are absorbed by other elements and can be used for the control of the reactor. The rest is in principle available for reseach, however the thermal capture flux of the ILL is $1.5 \cdot 10^{15}\mathrm{cm}^{-2}\mathrm{s}^{-1}$. At the Institut Laue Langevin a heavy water tank at 50° C is used to moderate the neutrons to thermal energies.

In two cold sources the spectrum is shifted to lower energies. From integration over the UCN energy range of a entirely moderated cold neutron spectrum the UCN density inside a cold source is given by:

$$\rho_{\mathrm{UCN}} = \frac{2}{3}\frac{\Phi_0}{\alpha}\left(\frac{V_{\mathrm{c}}}{k_{\mathrm{B}}T}\right)^{3/2}, \tag{2.11}$$

where T is the source temperature and $\alpha = \sqrt{2k_{\mathrm{B}}T_{\mathrm{n}}/m}$ with T_{n} the temperature of the neutron before moderation. For $T = 25$ K, $V_{\mathrm{c}} = 252$ neV (beryllium), and $\alpha = 2.3 \cdot 10^3$ m/s ($T_{\mathrm{n}} = 320$ K)

$$\rho_{\mathrm{UCN}} \approx 5500\mathrm{cm}^{-3},$$

where $\Phi_0 \approx 1.5 \cdot 10^{15}\mathrm{cm}^{-2}\mathrm{s}^{-1}$ is the continuous thermal flux density of the reactor at the cold source position. However, transportation losses in guides and windows reduce the density available for experiments tremendously. This is why several techniques have been pioneered in the last 30 years to increase the density of ultracold neutrons available inside experiments.

The phase space transformation of higher energy neutrons to ultracold neutrons was pioneered by Steyerl and coworkers [Ste75] at the Forschungsreaktor in Garching before it came to maturity at the ILL [Ste86]. Neutrons from the vertical cold source are extracted via a 12.8 m long vertical bend guide. The curvature of the guide helps to remove faster neutrons which are not reflected by the nickel coating. The vertical extraction leads to a deceleration of the neutrons due to gravity. Once they have passed through the guide they enter the turbine and are Doppler-shifted to the UCN energy range. The turbine consists of a 1.7 m diameter wheel with 690 bend and polished copper mirrors. The mirrors rotate in flight direction with a radial speed of 25 m/s which causes a velocity shift of the reflected neutrons and an increase in divergence. This technique provides an UCN density of $\rho \approx 50\mathrm{cm}^{-3}$ [Ste86].

The currently most promising technique, superthermal production of UCN, is based on a concept first proposed in 1977 by R. Golub and M. Pendlebury [Gol77]. The principle of superthermal production of UCN in solid deuterium or superfluid helium is based on inelastic neutron scattering. Superthermal indicates that the underlying cooling mechanism is not a thermal multi collision process, but that the density of UCN corresponds to a temprature much lower than the actual moderator temperature. The most intuitive case is a two level system with an energy gap E^*. A neutron can excite a quasi-particle from the lower state to the higher state by transfering the energy E^*; a quasi-particle from the higher state can fall down to the lower state by transfer of the energy E^* to a neutron. The equation of detailed balance links both processes:

$$\begin{aligned}\sigma(E_{\mathrm{UCN}} + E^* \rightarrow E_{\mathrm{UCN}}) \cdot (E_{\mathrm{UCN}} + E^*) \exp\left(-\tfrac{E_{\mathrm{UCN}}+E^*}{k_{\mathrm{B}}T}\right) = \\ \sigma(E_{\mathrm{UCN}} \rightarrow E_{\mathrm{UCN}} + E^*) \cdot E_{\mathrm{UCN}} \exp\left(-\tfrac{E_{\mathrm{UCN}}}{k_{\mathrm{B}}T}\right),\end{aligned} \tag{2.12}$$

where T is the moderator temperature and σ the total neutron scattering cross section of the converter.

The transfer of energy from the system to the neutron, in UCN physics called up-scattering, gets negligible for converter temperatures $T \ll E^*/k_{\mathrm{B}}$.

This allows to build up high UCN densities in corresponding converters if other loss mechanism, absorption on impurities or converter nuclei, are negligible. This is only the case in pure helium-4. By contrast, UCN sources based on deuterium with an absorption cross section of 0.000519 barn can not accumulate UCN inside the converter. Therefore all existing projects based on deuterium employ systems where the conversion to UCN is separated from their storage by a fast shutter, or the converter is a thin crystaline film in a small fraction of the entire storage volume.

2.3 UCN production in superfluid helium

2.3.1 Superfluid helium - phenomenology and terminology

In the rest of the work I will only consider UCN production in superfluid helium. It is therefore worthwhile to introduce at this point the required terminology of superfluid helium. I follow Ref. [Wil87] in the first part on macroscopic properties, whereas Ref. [Gly95] describes in more detail excitations in superfluid helium.

Macroscopic properties

As indicated on the phase diagram of helium, shown in Fig. 2.1, normal helium liquefies at 4.2 K (1013 mbar). Cooling the liquid further, there is an abrupt change of all its properties at $T_\lambda = 2.17$ K. This second order phase transition is known as λ–transition from the characteristic form of the specific heat curve and decreases with pressure (see Tab. 2.2). The liquids have so different properties above and below this point that one refers to them in the two region as *helium I* (He-I) and *helium II* (He-II) respectively. Most remarkable, cooling the liquid further it remains liquid under saturated vapour pressure down to lowest accessible temperature.

Excitations in superfluid helium

The basic concept to understand the macroscopic properties of He-II is that of elementary excitations. For small wave vector transfers q these excitations are conceptually similar to longitudinal phonons in solids. Additional to these there are excitations at large wave vectors $q \gtrsim 1.5$ Å^{-1} called rotons. The dispersion relation of excitations in He-II is shown in Fig. 2.2. In "The theory of superfluidity of Helium-II", Landau [Lan41] quantises an arbitrary system of interacting particles (liquid) by the means of introducing an op-

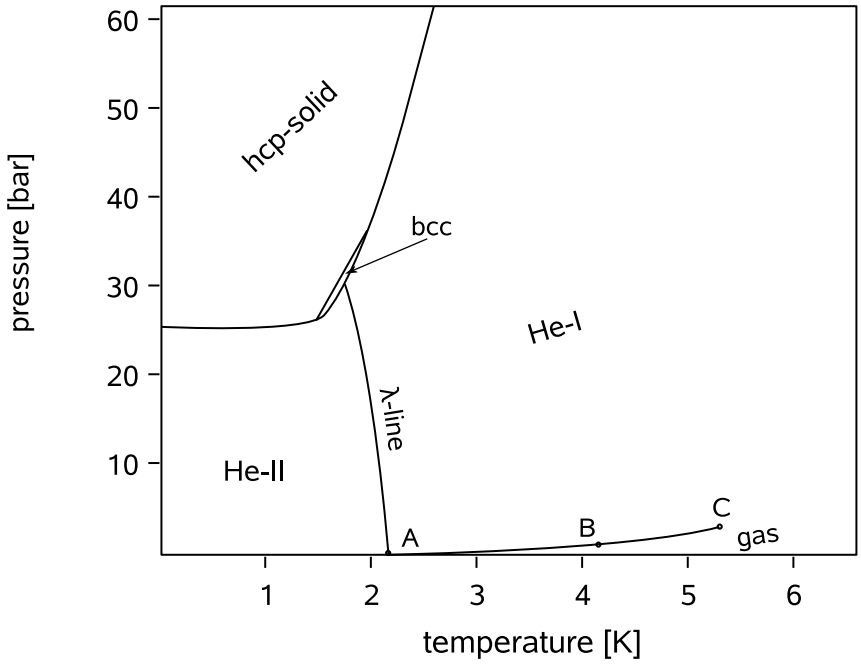

Figure 2.1: Phase diagram of ^{4}He, showing three characteristic points: A) λ–point (2.17 K), B) liquefaction under saturated vapour pressure (4.2 K), C) critical point (5.2 K). (Following Ref. [Lon54])

.

erator of the density and of the velocity of the liquid. This theory leads to two superimposed continuous energy spectra of the liquid. In the short wave vector region the energy spectrum derived from the quantisation of the density correspond to phonons or sound waves and their energy is a linear function of q:

$$E_{\mathrm{ph}} = \hbar\alpha q \tag{2.13}$$

where α is the velocity of sound. The lowest level of spectrum from quantisation of the velocity operator, called vortex spectrum, is situated above the lowest level of the phonon spectrum with $E \approx 0$ for $q \to 0$. They are separated by an energy gap Δ. The lowest elementary excitation of the vortex spectrum, often called roton, has an energy of:

$$E_{\mathrm{r}} = \Delta + \frac{\hbar^2 Q_{\mathrm{r}}^2}{2\mu}, \tag{2.14}$$

where μ is the "effective mass" of the roton, and $\hbar Q_{\mathrm{r}}$ its momentum. Both spectra combine to one single energy curve, which gives the dispersion curve of He-II. In such a combined spectrum it is impossible to distinguish the elementary excitations in two types. It would be more reasonable to talk of

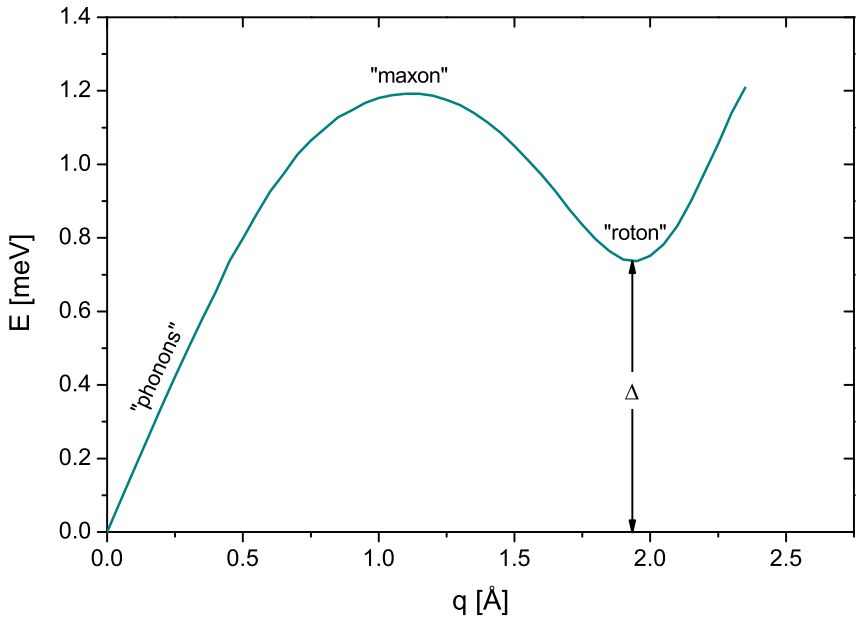

Figure 2.2: The phonon–roton dispersion relation of superfluid helium. $\Delta = 0.7426(21)$ meV [Gib96] at SVP and 0.5 K is the energy gap of the roton.

short wave vector and long wave vector excitations. However, in this work I will use the established vocabular of phonons and rotons.
This absence of excited states below the roton is defining the criterion for dispersive free flow — superfluidity; the fluid may flow past an obstacle at a given velocity and be unable to disperse energy via excitations which would create friction and viscosity. At a critical velocity $v > \Delta/\hbar q$, excitation may be created in the roton region of the dispersion relation. When this happens the fluid becomes resitant to flow. A decade later Cohen and Feynman [Coh57] proposed to measure the dispersion relation of superfluid helium using neutron scattering techniques. In Tab. 2.2, the Landau parameters $(\Delta, Q_\mathrm{r}\ \mu)$, from neutrons scattering data, and the first velocity of sound are listed for various pressures.

The linewidth of the excitation depends on the available decay modes. In regions where the group velocity v_g exceeds the first velocity of sound α, the excitation can decay in short wave vector phonons. The linewidth will be broadened. There are two region where this is the case: the very short wave vector range up to 0.5 $\mathrm{Å}^{-1}$ and the long wave vector range above 2.3 $\mathrm{Å}^{-1}$. Otherwise the excitation decays via a very well understood four quasi-particle decay mode which was theoretically introduced for the roton Landau and Khalatnikov [Lan49] and refined later by Bedell, Pines, and Zawadowski [Bed84] for all excitations. The excitation combines with a ther-

	SVP	5 bar	10 bar	15 bar	20 bar
T_λ [K]	2.172	2.122	2.063	1.998	1.928
ρ [gcm^{-3}]	0.14531	0.15301	0.15891	0.1642	0.16866
α [m/s]	238.3	274.38	302.75	326.71	347.62
u	2.84	2.61	2.46	2.35	2.27
Δ [meV]	0.7426(21)	0.7174(20)	0.6916(15)	0.6675(19)	0.6409(21)
Q_r [Å^{-1}]	1.929(2)	1.972(2)	2.005(2)	2.029(2)	2.056(2)
μ [m_He]	0.1613(39)	0.1457(31)	0.1302(25)	0.1230(28)	0.1124(33)

Table 2.2: Important helium parameters and their change with pressure [Abr70, Gib96] at 0.5 K. (Density ρ, first velocity of sound α, Grüneisen constant u, roton energy gap Δ, roton wave vector Q_r, roton reduced mass μ)

mally excited phonon and then decays into two new quasi-particles.

The linewidth was first precisely measured for the roton by Mezei [Mez80] ($\Gamma_\mathrm{R} \leq 0.1$ K $= 0.86$ μeV for 1 K) on IN11 of the ILL using the then newly developed neutron–spin-echo technique. Later a measurement by Andersen and colleagues [And96], in the same wave vector region with a neutron backscattering instrument (IN10B at the ILL), confirmed a linewidth of $\Gamma_\mathrm{R} <$ 1 μeV for $T < 1.0$ K with an improved instrument resolution. The sudden decrease in linewidth at ~ 0.5 $\mathring{A}^{-1}$ (phonon region) with increasing wave vector was first measured by Mezei [Mez91]. His result for 0.7 Å^{-1} is: $\Gamma_\mathrm{P} =$ 2(1) μeV at $T = 1.2$ K. In 1998 Keller and colleagues [Kel98] measured in this range again at $T = 1.1$ K and have found: $\Gamma_\mathrm{P} = 1.0(3)$ μeV. This is in the region of the four quasi-particle decay mode. This means the linewidth at 0.7 Å^{-1} decreases similar as for the roton with decreasing temperature. At temperatures below 0.7 K the excitation can be approximated by a δ-function.

The process in the phonon branch below 0.5 Å^{-1} is described by a three phonon decay mode by Maris [Mar77]. The experimental data do confirm the effect of a sudden decrease in linewidth at 0.5 Å^{-1}, but not the magnitude predicted in the model [Kel04].

2.3.2 Ultracold neutrons from inelastic scattering on superfluid Helium

The underlying mechanism of ultracold neutron sources based on He-II is the excitation of phonons in the superfluid by incident cold neutrons (CN) — the neutron is inelastically scattered.

In any neutron scattering experiment incident neutrons with wave vector $\boldsymbol{k}_\mathrm{i}$ are scattered by a sample into an outgoing neutron with wave vector $\boldsymbol{k}_\mathrm{f}$.

In this process momentum is conserved:

$$\hbar \boldsymbol{q} = \hbar \boldsymbol{k}_\mathrm{i} - \hbar \boldsymbol{k}_\mathrm{f}, \tag{2.15}$$

where $\hbar \boldsymbol{q}$ is the momentum transfered to the sample. In isotropic materials as glasses and liquids the direction of the momentum transfer is not important and therefore I will only use its magnitude $q = |\boldsymbol{q}|$. The energy transfer is

$$E = E_\mathrm{i} - E_\mathrm{f} = \frac{\hbar^2}{2m_\mathrm{n}} \left(k_\mathrm{i}^2 - k_\mathrm{f}^2 \right), \tag{2.16}$$

with the magnitudes of momenta k_i and k_f.

The inelastic neutron scattering for any sample can be described by the van Hove relation [Pla54]. It describes the scattering per nucleus of a neutron into the solid angle $\mathrm{d}\Omega$ and the energy interval $\mathrm{d}E$ and is called the double differential scattering cross section, given by:

$$\frac{\mathrm{d}^2\sigma}{\mathrm{d}\Omega \mathrm{d}E} = b^2 \frac{k_\mathrm{f}}{k_\mathrm{i}} S\left(q, E\right). \tag{2.17}$$

It is proportional to the square of the coherent scattering length b and the dynamic structure factor $S\left(q, E\right)$. For the UCN production only downscattered neutrons with total kinetic energy smaller than the wall potential V_c of the converter volume are of interest. Therefore the dynamic structure factor is evaluated for values on the dispersion curve of the free neutron. For this special scattering geometry, where $k_\mathrm{i} \gg k_\mathrm{f}$, one can take $q = k_\mathrm{i} = 2\pi/\lambda$. As the angular distribution of the scattered neutrons is of no importance one can integrate equation Eq.(2.17) over 4π which yields:

$$\frac{\mathrm{d}\sigma}{\mathrm{d}E_\mathrm{f}} \left(E_\mathrm{i}, E_\mathrm{f}\right) = \sigma \frac{\lambda_\mathrm{i}}{\lambda_\mathrm{f}} s(\lambda_\mathrm{i}), \tag{2.18}$$

where $\sigma = 4\pi b^2 = 1.34(2)$ barn [Sea92] is the helium scattering cross section and

$$s(\lambda_\mathrm{i}) = \int S\left(\lambda, E\right) \delta \left(E - \frac{h^2}{2\lambda_\mathrm{i}^2 m_\mathrm{n}} \right) \mathrm{d}E \tag{2.19}$$

the UCN scattering function, which can be divided into a single phonon and multiphonon part, $s(\lambda_\mathrm{i}) = s_\mathrm{I}(\lambda_\mathrm{i}) + s_\mathrm{II}(\lambda_\mathrm{i})$. For an incoming neutron beam with the flux $\Phi(E_\mathrm{i})$:

$$P_\mathrm{UCN}(V_\mathrm{C}) = \int_0^\infty \mathrm{d}E_\mathrm{i} \int_0^{V_\mathrm{C}} N \frac{\mathrm{d}\Phi(E_\mathrm{i})}{\mathrm{d}E_\mathrm{i}} \cdot \frac{\mathrm{d}\sigma}{\mathrm{d}E_\mathrm{f}} \left(E_\mathrm{i}, E_\mathrm{f}\right) \mathrm{d}E_\mathrm{f}, \tag{2.20}$$

where N is the number density of superfluid helium. It can be further transformed to:

$$\begin{aligned} P_{\mathrm{UCN}}(V_{\mathrm{C}}) &= N\,\sigma \int_0^{\infty} \mathrm{d}E_{\mathrm{i}} \int_0^{V_{\mathrm{C}}} \frac{\mathrm{d}\Phi}{\mathrm{d}E_{\mathrm{i}}} \frac{\lambda_{\mathrm{i}}}{\lambda_{\mathrm{f}}}\, s\left(\lambda_{\mathrm{i}}\right)\, \mathrm{d}E_{\mathrm{f}} \\ &= N\,\sigma \int_0^{\infty} \mathrm{d}E_{\mathrm{i}} \int_0^{\lambda_{\mathrm{c}}} \frac{\mathrm{d}\Phi}{\mathrm{d}E_{\mathrm{i}}}\, s\left(\lambda_{\mathrm{i}}\right) \lambda_{\mathrm{i}}\, \frac{h^2}{m_{\mathrm{n}} \lambda_{\mathrm{f}}^4}\, \mathrm{d}\lambda_{\mathrm{f}} \\ &= N\,\sigma \frac{h^2}{3 m_{\mathrm{n}} \lambda_{\mathrm{c}}^3} \int_0^{\infty} \frac{\mathrm{d}\Phi}{\mathrm{d}\lambda_{\mathrm{i}}}\, s\left(\lambda_{\mathrm{i}}\right) \lambda_{\mathrm{i}}\, \mathrm{d}\lambda_{\mathrm{i}}. \end{aligned} \tag{2.21}$$

The most prominent excitation is the strong response along the one-phonon dispersion relation of superfluid helium. This single phonon can be approximated by a delta function as its width is of the order of 1μeV at 1 K (see Sec. 2.3.1), small compared to the spectral width of a typical neutron beam. The intensity, which is the single excitation weight $Z(Q)$ in scattering literature, is given by the integral over the single phonon peak

$$S^* = \int S(q = 2\pi/\lambda^*, E)\mathrm{d}E$$

where λ^* is the intersection of the dispersion curve of superfluid helium and the free neutron. Evaluating the UCN production rate from single phonon excitations at λ^* with $s_{\mathrm{I}}(\lambda_{\mathrm{i}}) = \beta S^* \delta(\lambda_{\mathrm{i}} - \lambda^*)$ gives:

$$P_{\mathrm{I}}(V_{\mathrm{c}}) = N\sigma \left(\frac{V_{\mathrm{c}}}{E^*}\right)^{3/2} \frac{\lambda^*}{3} \cdot \beta\, S^* \cdot \frac{\mathrm{d}\Phi}{\mathrm{d}\lambda}\Big|_{\lambda^*}, \tag{2.22}$$

where

$$\beta = \frac{\frac{\mathrm{d}E_{\mathrm{n}}}{\mathrm{d}q}\Big|_{q^*}}{\frac{\mathrm{d}E_{\mathrm{n}}}{\mathrm{d}q}\Big|_{q^*} - \frac{\mathrm{d}E_{\mathrm{He}}}{\mathrm{d}q}\Big|_{q^*}}$$

accounts for the inclination between the two dispersion curves, $E_{\mathrm{n}}(q)$ and $E_{\mathrm{He}}(q)$.

The differential multiphonon production rate in $\mathrm{cm}^{-3}\mathrm{s}^{-1}\text{Å}^{-1}$ is then:

$$\frac{\mathrm{d}P_{\mathrm{II}}\left(V_{\mathrm{c}}\right)}{\mathrm{d}\lambda_{\mathrm{i}}} = N\sigma\, V_{\mathrm{c}} \frac{2}{3\lambda_{\mathrm{c}}} \frac{\mathrm{d}\Phi}{\mathrm{d}\lambda_{\mathrm{i}}} \lambda_{\mathrm{i}} \cdot s_{\mathrm{II}}(\lambda_{\mathrm{i}}), \tag{2.23}$$

which depends explicitly on the form of $s_{\mathrm{II}}(\lambda_{\mathrm{i}})$. Calculations for UCN production through single and multiphonon processes are presented in Sec. 3.

2.3.3 Up-scattering of UCN

The inverse process, where a neutron almost at rest inside the superfluid helium absorbs a thermal excitation, is called up-scattering. In general the neutron will gain enough energy to immediately leave the storage volume and therefore will be lost. In sources based on pure ^{4}He this is a very important loss mechanism. From the equation of detailed balance Eq.(2.12) it is clear that up-scattering from an absorption of a single phonon is suppressed by the factor $\exp(-E^*/k_{\mathrm{B}}T)$. By the same argument the simultaneous absorption of two or more excitations contributes even less (E^* is larger and the effective cross section is smaller). An important contribution comes from processes in which one excitation is absorbed and another one emitted. In the following considerations the final neutron momentum can be approximated with the momentum transfer of the scattering event ($\hbar\boldsymbol{k}_{\mathrm{f}} = \hbar\boldsymbol{Q}$), as the initial neutron is nearly at rest ($\boldsymbol{k}_{\mathrm{i}} \ll \boldsymbol{Q}$).

Following the general hydrodynamic approach of Landau and Khalatnikov [Lan49], Golub has shown in Ref. [Gol79b] how to calculate UCN loss rates for single phonon absorption and for phonon or roton absorption with immediate reemission of a phonon. Here I will only give the starting points of the calculations and the final results.

Single-phonon absorption

The simplest process is the absorption of a thermally excited phonon with wave vector $\boldsymbol{K}$ by a neutron, wave vector $\boldsymbol{k}_{\mathrm{i}}$. This process is exactly the inverse of the single phonon down-scattering, and shown schematically in Fig. 2.3a. The phonon is described, following [Lan49], as a fluctuation $N_1(\boldsymbol{r})$ of the equilibrium density of He-II. The potential V_{pan} is the optical potential of Eq.(2.9) for neutron–matter interaction where the number density $N(\boldsymbol{r})$ is replaced by $N_0 + N_1(\boldsymbol{r})$ for helium. The fluctuation $N_1(\boldsymbol{r})$ is written as:

$$N_1(\boldsymbol{r}) = \left(\frac{N_0\hbar}{2\alpha m_{\mathrm{He}}}\right)^{1/2} \sum_{\boldsymbol{K}} \sqrt{K}\left(a_{\boldsymbol{K}} e^{i\boldsymbol{K}\boldsymbol{r}} + a^{\dagger}_{\boldsymbol{K}} e^{-i\boldsymbol{K}\boldsymbol{r}}\right), \tag{2.24}$$

where N_0 is the equilibrium density, α the speed of sound in a linear approximation ($\omega = \alpha q$) of the low q dispersion relation of superfluid helium, and $a_{\boldsymbol{K}}, a^{\dagger}_{\boldsymbol{K}}$ the usual annihilation and creation operators. One then calculates the matrix element for plane wave neutron states ($e^{i\boldsymbol{k}_{\mathrm{i,f}}\boldsymbol{r}}/\sqrt{V}$), where V is an arbitrary integration volume which will later cancel out, with the interaction potential V_{pn}. Using the matrix element one can calculate with the "golden rule" the rate of one-phonon upscattering from

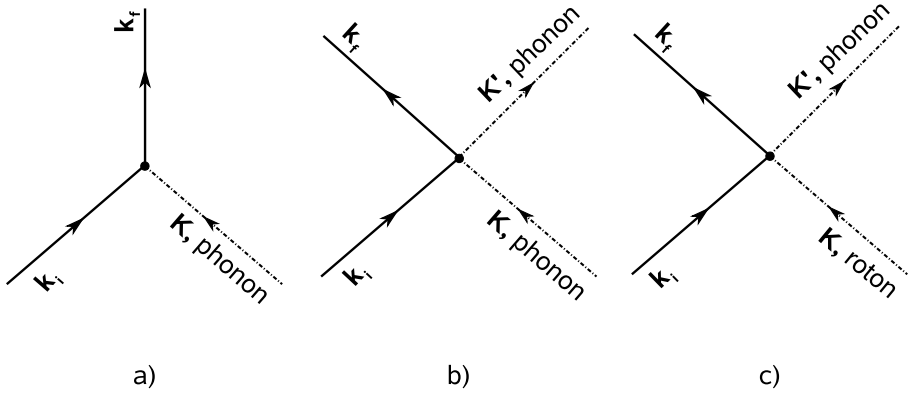

Figure 2.3: Schematic scattering diagrams for single phonon absorption (a), phonon absorption and reemission (b), and roton absorption and phonon emission (c).

$$\begin{aligned} 1/\tau_{1-\mathrm{ph}} &= \frac{2\pi}{\hbar} \int V \mathrm{d}^3Q \int V \mathrm{d}^3K \, |\langle f|V_{\mathrm{pn}}|i\rangle|^2 \, \delta\left(\hbar\alpha\left(\boldsymbol{K} - \frac{\hbar k^2}{2m_{\mathrm{n}}\alpha}\right)\right) \\ &= N_0\sigma\,(\hbar Q/m_{\mathrm{n}})\left(E^*/m_{\mathrm{He}}\alpha^2\right) e^{-E^*/k_{\mathrm{B}}T}, \end{aligned} \tag{2.25}$$

where $\hbar\boldsymbol{Q} = \hbar\boldsymbol{K} = \hbar\boldsymbol{k}_{\mathrm{f}}$ is the momentum transfer to the neutron and E^* the energy transfer, which is equal to the energy at the intersection of the free neutron and He-II dispersion relations. For saturated vapour pressure and a first velocity of sound of 238.3 m/s (see Tab. 2.2) the up-scattering rate is:

$$\begin{aligned} 1/\tau_{1-\mathrm{ph}} &= 557.64 \cdot e^{-E^*/k_{\mathrm{B}}T} \\ &= \quad 1/246 \text{ s}^{-1} \qquad (1 \text{ K}) \\ &= 1/(6.7 \cdot 10^5) \text{ s}^{-1}. \quad (0.6 \text{ K}) \end{aligned}$$

These figures are slightly smaller as the ones in Ref. [Gol79b], as I use a different value for σ [Sea92] and for $\boldsymbol{Q}$ the experimental value from the intersection of the dispersion curves of the free neutron and of He-II.

Two phonons

A more substantial contribution to the overall loss rate at temperatures close to 1 K is caused by processes in which a phonon is absorbed and another emitted (see Fig. 2.3b). Let $\boldsymbol{K}, \boldsymbol{K}'$ be the wave vectors of the incident and final phonon and $\boldsymbol{Q}$ the momentum transfer, which is nearly identical with the final momentum $\boldsymbol{k}_{\mathrm{f}}$ of the neutron. Following Golub [Gol79b] and Landau and Khalatnikov [Lan49] only processes in which V_{pn} and the cubic part of the hydrodynamic Hamilton:

$$V_3(r) = m_{\mathrm{He}} \left[\frac{\boldsymbol{v}(\boldsymbol{r}) \cdot N_1(\boldsymbol{r}) \boldsymbol{v}(\boldsymbol{r})}{2} + \frac{1}{3!} \frac{\partial}{\partial N} \frac{\alpha^2}{N} N_1^3(\boldsymbol{r}) \right] \tag{2.26}$$

each operate once contribute to low-temperature up-scattering. Without going into details the upscattering rate is given by:

$$\begin{aligned} \frac{1}{\tau_{\mathrm{pp}}} &= \frac{\sigma \alpha k_{\mathrm{B}}^7}{(4\pi)^2} \left(\frac{T}{m_{\mathrm{n}} \alpha^2} \right)^2 \left(\frac{T}{m_{\mathrm{He}} \alpha^2} \right)^2 \left(\frac{T}{\hbar \alpha} \right)^3 \cdot I \\ &= 9.32 \cdot 10^{-7} T^7 \cdot I, \end{aligned} \tag{2.27}$$

where I is a dimensionless integral:

$$\begin{aligned} I = & \int\limits_{|z_1 - z_2| \leq Q \leq |z_1 + z_2|} \mathrm{d}z_Q \frac{z_Q^3 z_Q'^2}{\left[z_Q'^2 - (z_Q^2 / z^*)^2 \right]} \\ & \cdot \int \mathrm{d}z_1 \frac{z_1^2 z_2^2 n_1 (n_2 + 1)}{1 + \tilde{f}'(z_2)} \\ & \cdot \left[\sum_{i \neq j} \cos \Theta_{ik} + 2u_0 - 1 \right]^2, \end{aligned} \tag{2.28}$$

with $z_j = \hbar \alpha k_j / k_{\mathrm{B}} T \, (j = \mathrm{i}, \mathrm{f}, Q, *)$ and where Θ_{ik} are the angle between the momenta and $u_0 = (N/\alpha)(\partial \alpha / \partial N) \approx 2.84$. The difference of the real He-II dispersion relation to a linear phonon dispersion relation is given by $f(k)$ from Maris [Mar73], which translates to $\tilde{f}(z) = \hbar f(k) / k_{\mathrm{B}} T$. The integral was solved numerically by Golub with the assumption of a neutron at rest. It is neither independent of temperature nor of changes in the number density of the liquid or in the first velocity of sound. The values obtained in Ref. [Gol79a] for SVP are $I(0.6\,K) = 1.22 \cdot 10^4$ and $I(1.0\,K) = 1.06 \cdot 10^4$. Calculating with these values and Eq.(2.27) the loss rate at 0.6 and 1.0 K yields:

$$
\begin{aligned}
1/\tau_{\mathrm{pp}} = &\ 1/3142\ \mathrm{s}^{-1} \quad (0.6\ \mathrm{K}) \\
= &\ 1/101\ \mathrm{s}^{-1}. \quad (1.0\ \mathrm{K})
\end{aligned}
$$

Roton–phonon process

The last process contributing considerably to the UCN loss rate through up-scattering is the absorption of a roton and the subsequent emission of a phonon (see Fig. 2.3c). The dominant part of the interaction potential for scattering a neutron from a roton through one-phonon exchange can be written as (see again Ref. [Gol79b]):

$$
V_{\mathrm{rp}} = -\frac{1}{2}\left(\boldsymbol{p}\cdot\boldsymbol{v} + \boldsymbol{v}\cdot\boldsymbol{p}\right), \tag{2.29}
$$

where $\boldsymbol{p}$ is the roton momentum operator and $\boldsymbol{v}$ the phonon velocity-field operator. The result for the up-scattering rate is:

$$
\begin{aligned}
\frac{1}{\tau_{\mathrm{rp}}} &= \frac{3\sigma}{8(\pi)^{3/2}}\frac{\mu^2}{m_{\mathrm{n}}m_{\mathrm{He}}}\left(\frac{Q_{\mathrm{R}}^3}{m_{\mathrm{n}}\alpha}\right)\left(\frac{k_{\mathrm{B}}T}{m_{\mathrm{He}}\alpha^2}\right)\sqrt{2\mu\alpha^2 k_{\mathrm{B}}T}\,e^{-\Delta/k_{\mathrm{B}}T}, \quad (2.30) \\
&= 14.8\cdot T^{3/2}e^{-\Delta/k_{\mathrm{B}}T}\,\mathrm{K}^{-3/2}\mathrm{s}^{-1} \\
&= 1/369\ \mathrm{s}^{-1} \qquad (1\ \mathrm{K}) \\
&= 1/(2.46\cdot 10^6)\ \mathrm{s}^{-1} \qquad (0.6\ \mathrm{K})
\end{aligned}
$$

where Δ, μ and Q_{R} are the Landau parameters (see Tab. 2.2) describing the roton minimum of the dispersion relation.

The most important contribution at SVP and $T = 1$ K comes from the two-excitation processes. However, at temperatures below 0.6 K up-scattering becomes negligible and losses on wall collisions will dominate. In the following chapter the dependence of UCN production and up-scattering on pressure is discussed, using the data from Gibbs [Gib96].

Chapter 3

Calculations of UCN production rates from inelastic neutron scattering

3.1 Inelastic neutron scattering

The neutron is an ideal probe of condensed matter. The absence of charge and weak absorption allows it to investigate properties of the bulk, rather than near surface properties as it is usually the case with X-rays and other methods using electromagnetic interactions. Neutrons interact with the nuclei of the atoms. The magnetic moment of the neutron can interact with an overall magnetic moment of the shell electrons. Their sensitivity to magnetism and specific isotopes are important advantages. With neutron scattering techniques, both the static structure and the dynamics of materials can be studied. A moderated neutron has typically a wavelength of the order of interatomic distances ($\sim$ Å). As a wave it is therefore diffracted from the atomic structure and gives measureable informations on the positions of the atoms within the probe. Today neutrons have found a wide field of applications. The study of crystalline structures, disorder within materials, large scale structures such as biological macro molecules, liquids and amorphous materials are only examples of these applications. The simultaneous study of atomic structure and dynamics is highly useful in the investigation of excitations (e.g. phonons and magnons) in solid matter but also for collective excitations in liquids. The collective excitations of superfluid helium have been the centre of interest for a long time, their behaviour under pressure is described in great detail in the PhD thesis of M.R. Gibbs [Gib96].

3.1.1 Measuring the dynamic structure factor *S(q,E)*

In general inelastic neutron scattering observes the double differential of the scattering cross section described by the van Hove equation Eq.(2.17). Apart from kinematic terms and the total scattering cross section it also includes the dynamic structure facture $S(\boldsymbol{q}, E)$; a function which contains all information of the atomic structure and dynamics of the sample. This makes inelastic scattering a so powerful tool to investigate superfluid helium, but also any other liquid or solid, for UCN production. The essential observables needed to learn something about the dynamic structure factor are the incident neutron energy E_i, the scattered neutron energy E_f, and the angles Φ and Θ in spherical coordinates between the incident and final momentum. For liquids and glasses the scattering is isotropic in Θ and one only measures Φ. With the precise knowledge of these values a spectrometer can pin out any point in the $(\boldsymbol{q} - E)$ space and measure its scattering amplitude. This is most often done in one of the following two ways:

1. With a three axis spectrometer reflections from a single crystal (e.g. Cu, Ge, or pyrolytic graphite), satisfying the Bragg condition, are used to select the incident neutron energy (first axis) and then analyse the final energy (third axis). The second axis is the rotation axis of the sample around which the analyser can be turned (see Fig. 3.1).

2. In a time-of-flight spectrometer time is used to determine the energy transfer to the scattered neutron. The incident energy is selected with a single crystal or a system of choppers. A chopper sets the start signal of the time of flight. The total flight time and angle is recorded for each neutron scattered from the sample into the surrounding detector array with angular resolution.

The three-axis spectrometer allows one to choose exactly any combination of $\boldsymbol{q}$ and E within the kinematic limits. Therefore it is perfectly appropriate to measure the UCN down scattering function, as one could follow the dispersion parabola of the free neutron ($E = \frac{\hbar^2 q^2}{2m_\mathrm{n}}$). In general they only play a minor role in investigations of liquids, as the orientation of the sample is of no importance (no crystal structure). In the following I will only discuss in detail aspects of time-of-flight spectrometers as the raw data available for this analysis was measured with this kind of spectrometer.

3.1.2 Time-of-flight neutron inelastic scattering

Time-of-flight spectrometers' main advantages are the fast and simultaneous observation of a large part of the entire $(\boldsymbol{q} - E)$ space. This is achieved by

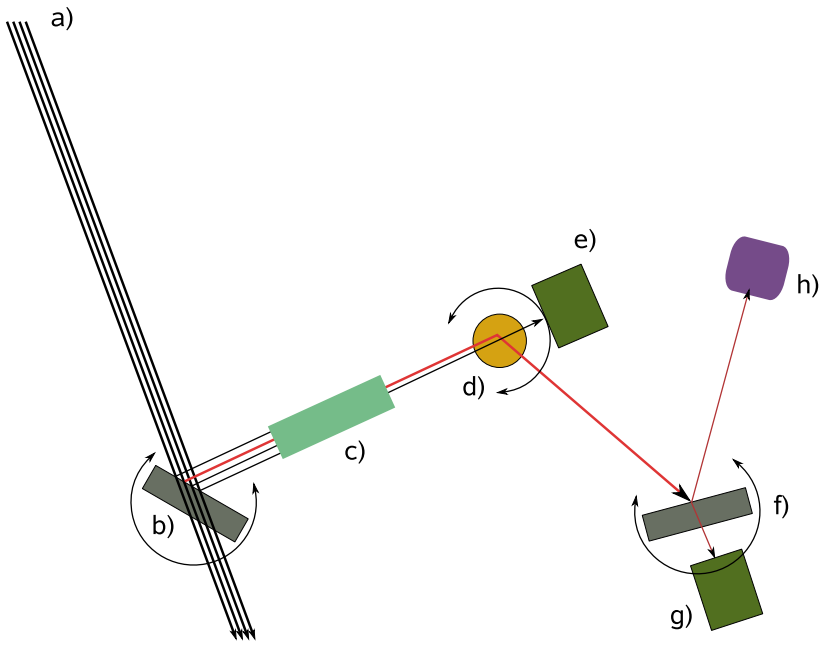

Figure 3.1: Schematic view of a typical triple-axis spectrometer. (a) incident ploychromatic neutron beam, (b) Bragg monochromator (1^{st}–axis), (c) collimator and apertures, (d) sample (2^{nd}–axis), (e and g) beam stops, (f) Bragg analyser (3^{rd}–axis), (h) detector.

measuring angle and energy transfer of each scattered neutron, whereas three-axis spectrometers accept only one point in $(\boldsymbol{q} - E)$. On the other hand, one is accepting a bigger incertitude in the angular resolution as with three-axis spectrometers. If either E_i or E_f is known the other can be calculated from the measured time-of-flight of the neutron from a point before the sample to the detector. These two modes of operation are known as direct (E_i known, E_f calculated) and indirect (inverse) operation. An example for the direct case is shown in Fig. 3.2. The total flight time is given by

$$t = \frac{L_\mathrm{i}}{v_\mathrm{i}} + \frac{L_\mathrm{f}}{v_\mathrm{f}}, \tag{3.1}$$

where v_i and v_f are the respective initial and final velocities, and L_i, L_f are the corresponding flight path lengths. Thereafter the calculation of the final neutron energy is straight-forward. The angular resolution is provided by the division of the sample circumjacent detector in smaller subdetectors.

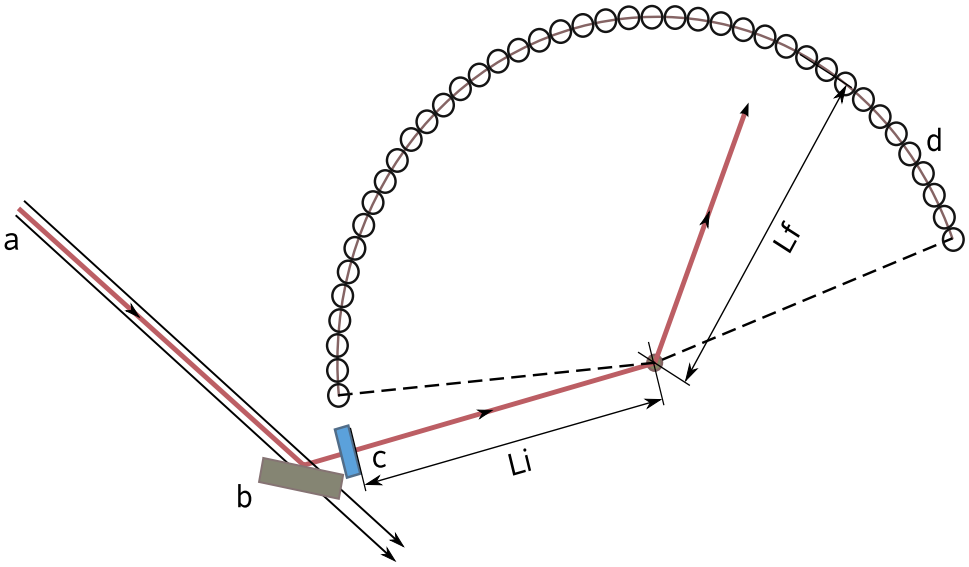

Figure 3.2: Sketch of time–of–flight spectrometer with crystal monochromator. Neutrons from the reactor a) pass through a crystal b). Only one wavelength is reflected out of the beam under the Bragg condition. A chopper divides the monochromatic beam in short bunches and triggers the clock. The time-of-flight for each neutron is measured when it is detected in one of the subdetectors d). This allows one to measure simultaneously the energy transfer to the probe and the scattering angle of the neutron.

3.2 Pressure Dependence of the Dynamic Scattering Function

The dynamic scattering function of superfluid helium at saturated vapour pressure (SVP), and $p = 2, 5, 10, 15$ bar and 20 bar has been measured by Gibbs and colleagues [Sti94, Gib96, Gib99, Gib00] on the IN6 time-of-flight spectrometer. For most of the measurements an incident neutron wavelength of $\lambda_\mathrm{i} = 4.15$ Å was chosen, this allows covering the entire phonon-roton dispersion relation as shown in Fig. 3.3 in a single measurement. Only for the study of SVP an incident wavelength of $\lambda_\mathrm{i} = 4.463$ Å was selected to have a narrower resolution. The counting time of each measurement was approximately four hours. For details of the measurement please refer to the PhD thesis of Gibbs [Gib96], in which the exact calibration procedure is described. In a comparative analysis of the static structure and the static response function of He-II, by Caupin and colleagues [Cau08], it is pointed out, that Gibbs most likely forgot to correct for the increased number density with pressure.

The most evident change with increasing pressure is the shift in position of the helium dispersion relation as shown in Fig. 3.3. In the phonon region, the gradient of the dispersion ($\mathrm{d}E/\mathrm{d}Q$) is larger at pressure, according to the

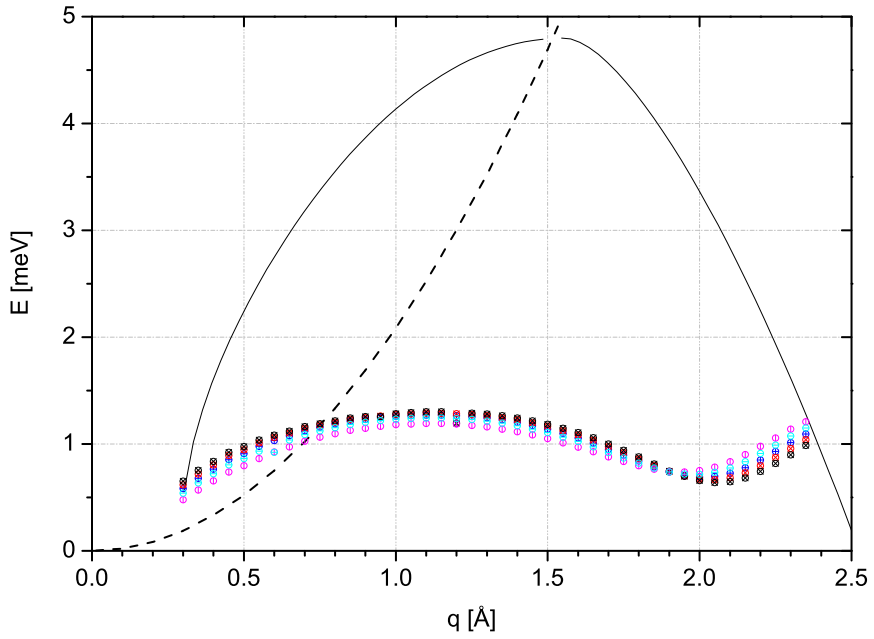

Figure 3.3: Range in $(\boldsymbol{q} - E)$ space covered by the IN6 spectrometer with an incident energy of 4.87 meV. The region is delimited by the constant scattering angle Jacobean of the largest and smallest detector angles (—). Also shown are the phonon dispersion relations for superfluid helium at SVP, 5, 10, 15 bar, and 20 bar and of the free neutron (- - -).

increase in the first sound velocity. The excitation energies increase for the same wavevectors up to nearly the roton minimum, thereafter they decrease with pressure. The wavevector of the roton Q_r is larger for higher pressures.

In Secs 3.3–3.5 I will use the data from Gibbs and colleagues [Sti94, Gib96, Gib99, Gib00] to calculate UCN production. For this purpose I have treated the existing raw data to obtain a higher resolution in q. Existing data points, corrected for the change in number density with pressure, from Ref. [Gib96] where used as benchmark for our analysis. A typical measurement of the dynamic scattering function $S(q, \hbar\omega)$ is shown in Fig. 3.4. For the analysis the $(q - \hbar\omega)$-plane is divided into slices with width $\Delta q = 0.2$ Å^{-1} (Fig. 3.5) to extract the value of $s(\lambda = 2\pi/q)$ for each q.

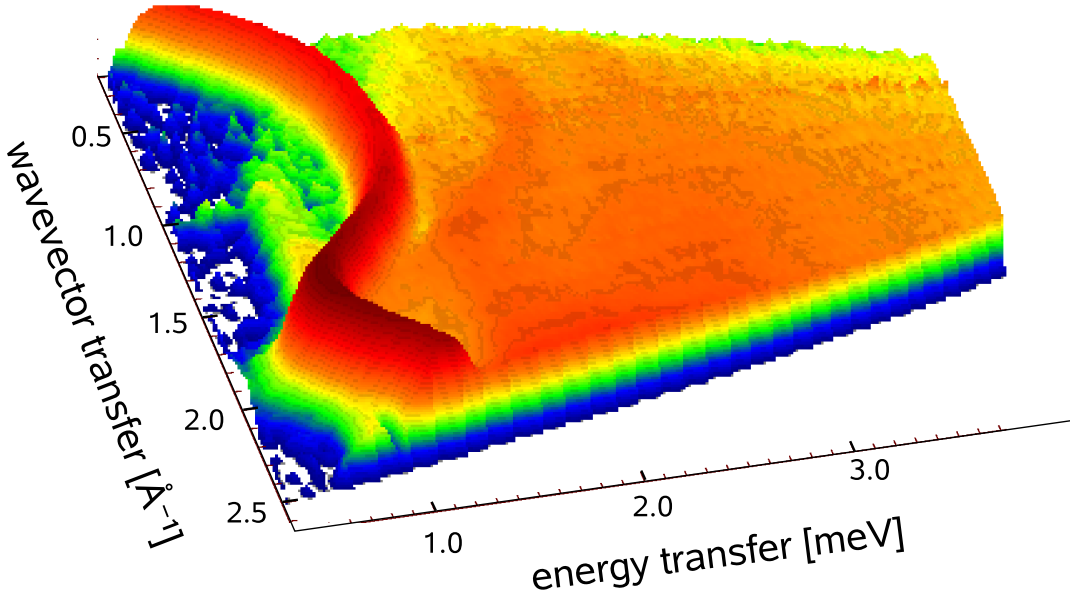

Figure 3.4: The dynamic scattering function $S(q, \hbar\omega)$, for helium at $T = 0.5$ K and $p = 10$ bar, measured by Gibbs and binned for the present purpose. For analysis the plane is divided along the q-axis into slices of width $\Delta q = 0.2$ Å^{-1} (see Fig. 3.5 for examples).

3.3 Pressure Dependence of the UCN Production Rate

In this part of the work I will use the method derived in Sec. 2.3.2 to calculate explicitly UCN conversion rates. Originally calculations have focused only on the single phonon process, where incident 8.9 Å neutrons are downscattered to the UCN energy domain [Gol77, Abe01]. The multiphonon contribution was deemed to be much less important [Pen82]. Later two publications [Kor02, Sch03] have set out to calculate the expected UCN production rate from processes involving the emission of two or more excitations, with inconsistent results. In a different approach Yoshiki [Yos03] calculated the total scattering cross section σ for UCN production from single-phonon excitations.

For both, the calculation of the single and the multiphonon production rate from inelastic neutron scattering experiments it is required to know precisely the dynamic scattering function along the dispersion curve of the free neutron. These values (see Eq.2.19):

$$s(\lambda) = \hbar \int S(q, \hbar\omega, p)\delta(\hbar\omega - \hbar^2 q^2/2m_\mathrm{n})\mathrm{d}\omega,$$

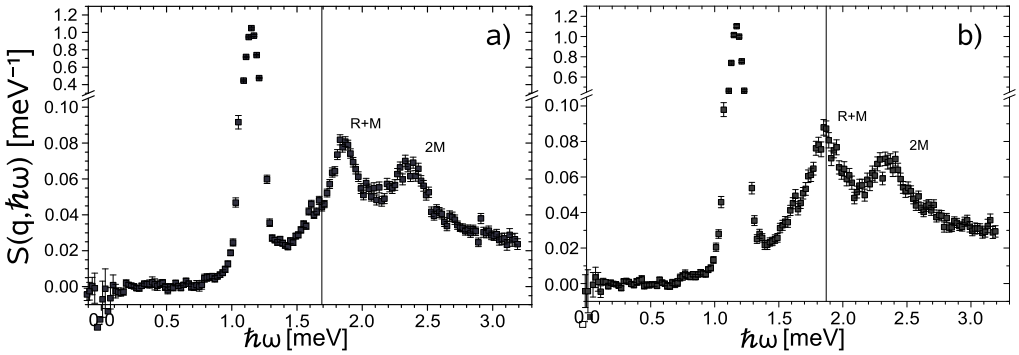

Figure 3.5: $S(q, \hbar\omega)$ for $q = 0.90$ Å^{-1} and $q = 0.95$ Å^{-1}. The vertical lines indicate the energy of an incident neutron with $E = \hbar^2 q^2 / 2m_\mathrm{n}$ that can be downscattered to the UCN energy range. The width of the single phonon excitation is dominated by the finite resolution of the instrument. The higher-energy roton-maxon (R+M) and two maxon (2M) resonances are significantly lower in intensity.

can be extracted from ToF data.

As argued in Sec. 2.3.1 the single excitation of $S(q, E)$ of He-II in the range $0.5 < q < 0.9$ can be approximated by a delta function at $E_{1-\mathrm{ph}}$. The convolution of the excitation with the instrumental resolution gives a Lorentzian like peak, whose surface is the scattering intensity S^*. For each q the single phonon peak is fitted with a Lorentzian peak at $E_{1-\mathrm{ph}}$ and is subtracted from $S(q, E)$. This subtraction method was proposed by Miller and colleagues [Mil62]. Thus the scattering function $s(\lambda)$ can be divided into a single, $s_\mathrm{I}(\lambda)$ and a multi-phonon part, $s_\mathrm{II}(\lambda)$. In the case where $E_\mathrm{n} = E_{1-\mathrm{ph}}$ and $q \approx k_\mathrm{i}$ the neutron excites exactly one phonon and is scattered to the UCN energy range.

UCN production from single phonon processes

With pressure the intersection of the dispersion relations of the free neutron and of helium moves to higher values of the momentum transfer q. In Fig. 3.6 the decrease in intensity of the one-phonon peak with pressure is shown. Furthermore, the relative inclination of both dispersion relation at the intersection described by β point decreases with pressure.

The UCN production rate from single phonon excitations in He-II at 0.5 K and SVP is:

$$P_\mathrm{I}(V_\mathrm{c}) = 4.97(38) \cdot 10^{-8} \frac{\text{Å}}{\mathrm{cm}} \frac{\mathrm{d}\Phi(E_\mathrm{i})}{\mathrm{d}\lambda}\Big|_{\lambda^*}. \tag{3.2}$$

In Tab. 3.1 all relevant factors and the UCN production rates for different

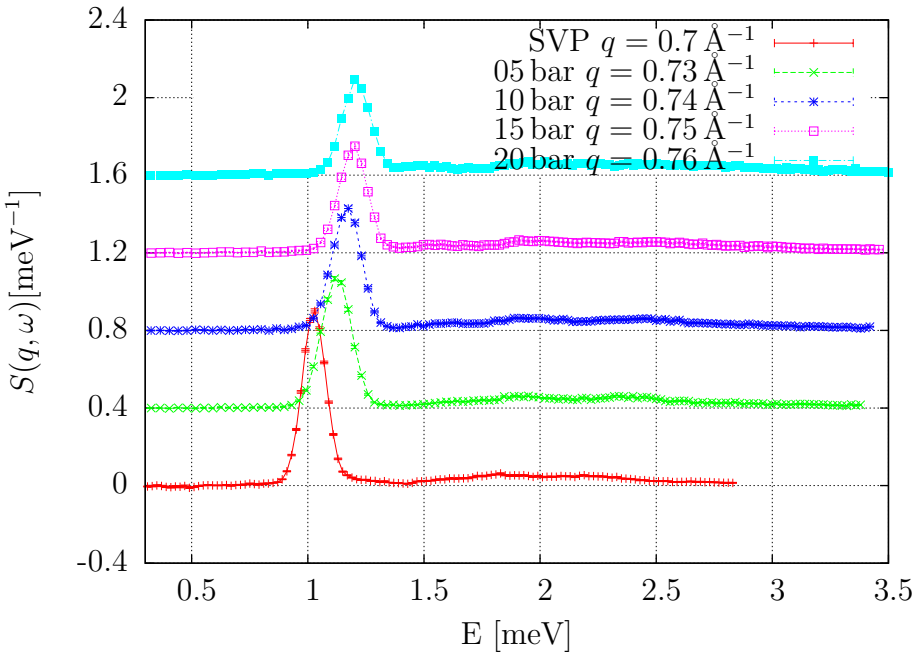

Figure 3.6: $S(q,\omega)$-slices for $q = \sqrt{2m_\mathrm{n} \cdot \omega/\hbar}$, at 0.5 K where $\hbar\omega$ is closest to the energy at the intersection of the dispersion relations of helium and of a free neutron. The intense peak is the single phonon excitation. Its surface is the scattering intensity S^* which decreases with pressure. The adjacent multiphonon region is much weaker in intensity and can be separated by simple substraction. The curves are shifted vertically by 0.4 meV^{-1} each. The lines serve to guide the eye.

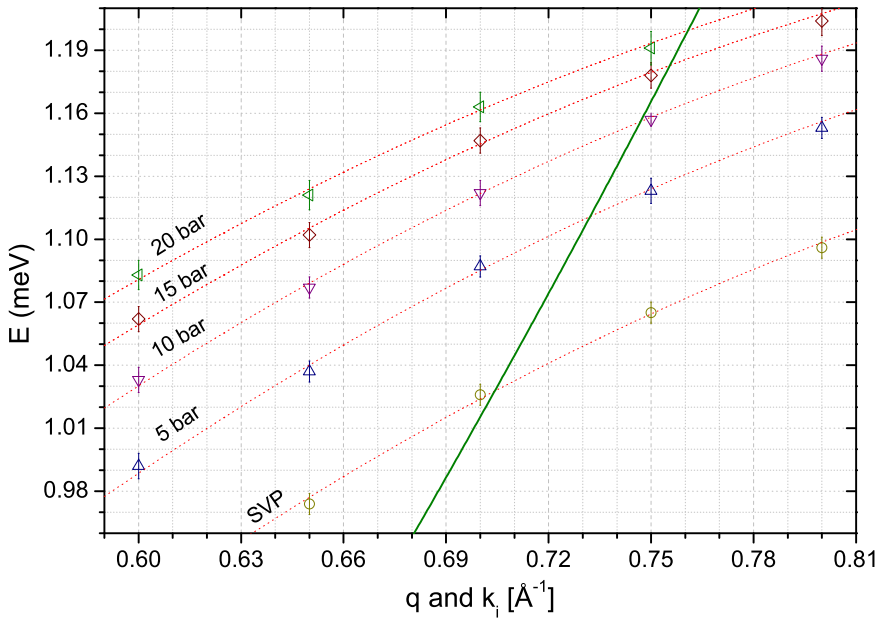

Figure 3.7: Intersection of the free neutron dipsersion relation $E_{\mathrm{n}}(k_{\mathrm{i}})$ with dispersion curves of superfluid helium $E_{\mathrm{He}}(q)$ at 0.5 K and p = SVP, 5, 10, 15 bar and 20 bar [Gib96]. The (- - -) indicates least-χ^2 fits with parabolas to the data ranges shown. β and $\lambda^*(p)$ are deduced from the shown intersections.

pressures are shown. They are calculated using Eq.(2.22) with parameters from Ref. [Gib96], corrected for the change in number density, or are deduced from data within this reference (see Fig. 3.7). The optical potential of helium was taken into account. The wall potential used was 252(2) neV (beryllium). For a CN spectrum like the one of PF1b (see Fig. 5.3b) the UCN production rate from one-phonon processes will decrease with pressure.

The value in Eq.(3.2) is higher as values previously published in Ref. [Bak03, Kor02]. Baker and coworkers [Bak03] refer to two other publications [Gol77, Yos03]. Golub and Pendlebury [Gol77] use $\sigma = 1$ barn, $\beta = 2$, and $S^* = 0.1$ in their article. Yoshiki [Yos03] is calculating numerical the total cross section $\sigma_{1-\mathrm{ph}} = 22$ μbarn for UCN production, for $\sigma = 1.34(2)$ barn, and $S^* = 0.117(7)$. From this one can derive an UCN production rate from single phonon excitations with:

$$\begin{aligned} P_{\mathrm{I}} &= N \cdot \sigma \cdot \mathrm{d}\lambda \frac{\mathrm{d}\Phi}{\mathrm{d}\lambda}|_{\lambda^*} \\ &= 5.06(21) \cdot 10^{-8} \frac{\text{Å}}{\mathrm{cm}} \frac{\mathrm{d}\Phi}{\mathrm{d}\lambda}|_{\lambda^*}. \end{aligned} \tag{3.3}$$

	SVP	5 bar	10 bar	15 bar	20 bar
λ^* [Å]	8.92(2)	8.58(2)	8.41(1)	8.32(2)	8.26(2)
N [10^{22}cm^{-3}]	2.1835	2.2992	2.3879	2.4674	2.5317
β	1.42	1.32	1.28	1.23	1.21
S^* [meV^{-1}]	0.118(8)	0.105(8)	0.091(9)	0.076(9)	0.066(7)
$P_{1-\mathrm{ph}}/\left(\frac{\mathrm{d}\Phi}{\mathrm{d}\lambda\|_{\lambda^*}}\right)$ [10^{-8}Å/cm]	4.97(38)	3.73(28)	2.99(23)	2.39(18)	1.96(16)
relative factor	1	0.75(11)	0.60(10)	0.48(9)	0.41(8)

Table 3.1: Factors relevant for single phonon production rate deduced from inelastic neutron scattering data of Gibbs [Gib96] (S^* is identical to $Z(Q)$ at the intersection multiplied with the correction proposed by Ref. [Cau08]). The absolute value is given for beryllium with a wall potential $V_{\mathrm{F}} = 252(2)$ neV. The number densities were calculated from the mass density (see Tab. 2.2).

for a $\mathrm{d}\lambda = 0.1053$ Å, which describes the range of wavelength of incident neutrons that contribute to the production rate in a beryllium vessel. The optical potential of helium is not yet taken into account. It changes the range of integration ($\mathrm{d}\lambda$) and the value of $\sigma_{1-\mathrm{ph}}$, as the integration limits for k_{f} and $\mathrm{d}\Theta\mathrm{d}\Phi$ change. This can be approximated by a multiplicative factor

$$[(252 - 18.5)/252]^{3/2} \approx 0.89.$$

The paper from Korobkina and coworkers [Kor02] gives a production rate of:

$$\begin{aligned} P_{\mathrm{I}} &= 9.44 \cdot 10^{-9} \frac{\mathrm{d}\Phi}{\mathrm{d}E}|_{E^*} \\ &= 4.38 \cdot 10^{-8} \frac{\text{Å}}{\mathrm{cm}} \frac{\mathrm{d}\Phi}{\mathrm{d}\lambda}|_{\lambda^*}, \end{aligned}$$

where they have used $S^* = 0.1$ and $\beta = 1.45$.

The value calculated is in agreement within the errorbars with the value given by Yoshiki. The deviation from the value published by Korobkina and coworkers can be explained by the new value used for $S^* = 0.118(8)$. Which is confirmed in the recent comparative analysis of the static structure factor and the static response function of superfluid helium-4 [Cau08]. There the authors state that the Gibbs data at SVP agrees well to other measurements and recommend their use.

UCN production from multiphonon processes

The situation looks slightly differently for the UCN production rate from multiphonon scattering processes. With increasing pressure the broad peak of the multiphonon excitations move to shorter neutron incident wavelengths (see Fig 3.8). Intensities of the excitations do not change within the statistical errors of the measurement.

The pressure dependent UCN production rate from multiphonon excitation processes can be calculated by integration over Eq.(2.23) with a given incident neutron spectrum $\mathrm{d}\Phi/\mathrm{d}\lambda$. The results for a numerical integration of the interpolated real data with the spectrum of PF1b [Abe06] for wavelengths between 4.2 Å and λ^* are listed in Tab. 3.2. The increase in production rate is mostly due to the increase in ^{4}He number density N with pressure. For $\lambda > 4.2$ Å no experimental data is available (see also Fig. 3.3).

An accepted model for the extrapolation to short wavelengths is given by Family [Fam75]. It was developed from low-order diagrams of the interparticle interactions in the high frequency limit and predicts $S(q, \hbar\omega) \propto q^4\omega^{-7/2}$. It is valid for any liquid and an interaction potential which can be approximated by a hard shell potential. In general this is the case for helium. In an analysis along the dispersion curve of the neutron this leads to $s_{\mathrm{II}}(\lambda) \propto \lambda^3$.

For a global characterisation of the multiphonon scattering function, I have found the following analytical expression useful,

$$s_{\mathrm{II}}(\lambda) = \sum_i \frac{f_i \lambda^3}{\exp\left(p_i \cdot \frac{E_i - h^2/2m_{\mathrm{n}}\lambda^2}{E_{\mathrm{R}}}\right) + 1}, \tag{3.4}$$

where E_i is the energy sum of a maxon and a roton, two rotons, and two maxons, respectively. $E_{\mathrm{R}} = \hbar^2 k_{\mathrm{i}}^2 / 2m_{\mathrm{He}}$ is the recoil energy and f_i, p_i are fitting parameters (see Tab. 3.3). It allows a global analytical description of the multiphonon scattering function. For $\lambda \ll 6$ Å it converges to the model of Family. In Fig. 3.8 the correspondence to the measured data is shown. Results from calculations for the entire cold neutron spectrum of PF1b using this model, excluding the single phonon part are also presented in Tab. 3.2. Earlier calculations done for SVP by Schott and coworkers [Sch03] predict a huge increase in the scattering function for short wavelengths. This appears to contradict the first moment sum rule [Rah62]

$$\int \mathrm{d}\omega \omega S(q, \hbar\omega) = \frac{\hbar q^2}{2m^{\mathrm{He}}}. \tag{3.5}$$

The linear extrapolation in q used in Ref. [Kor02](SVP only) overestimates the multiphonon contribution with respect to the Family model. On the long

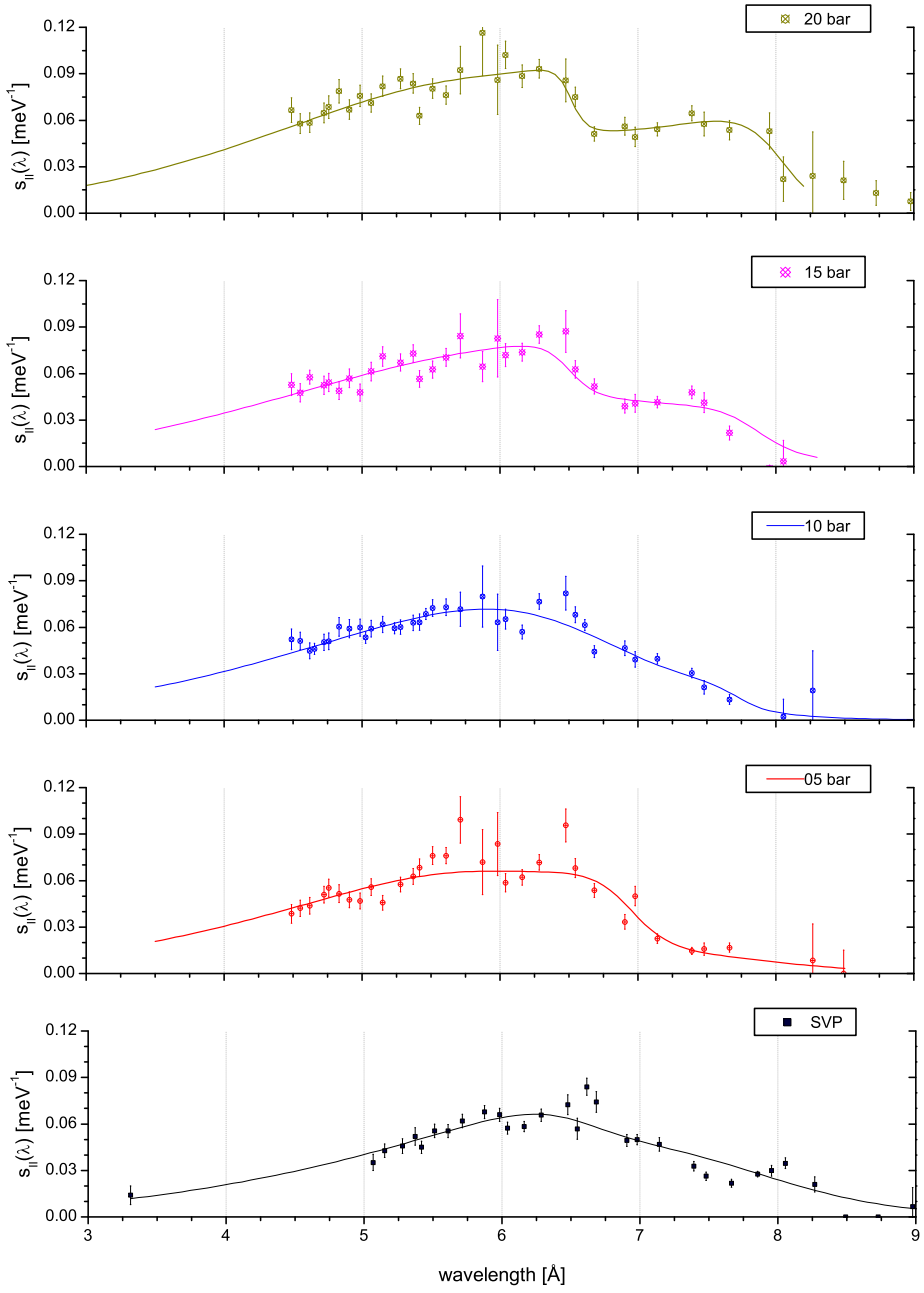

Figure 3.8: Multiphonon scattering functions $s_{\mathrm{II}}(\lambda)$ for $p = 5, 10, 15, 20$ bar at 0.5 K and SVP at 1.24 K. The broad region is fitted with the phenomenological model of Eq.(3.4).

pressure [bar]	P_{II}[cm^{-3}s^{-1}] interpolated	P_{II}[cm^{-3}s^{-1}] model
SVP	3.2(2)	2.7(6)
5	3.4(2)	3.3(6)
10	3.7(3)	3.8(6)
15	4.4(3)	4.6(8)
20	6.7(3)	6.6(8)

Table 3.2: Calculated UCN production rates from multiphonon processes for the cold neutron spectrum from PF1b [Abe06] shown in Fig. 5.3. For the interpolation of the data a linear interpolation was used with a step size of 0.1 Å. The right column presents the values obtained with Eq.(3.4) and the parameters in Tab. 3.3

	SVP	05 bar	10 bar	15 bar	20 bar
f_1 [$\cdot 10^{-3}$]	0.19	0.05	0.03	0.07	0.14
f_2 [$\cdot 10^{-3}$]	0.14	0.15	0.34	0.13	0.16
f_3 [$\cdot 10^{-3}$]	—	0.28	0.14	0.40	0.37
p_1	1.73	1.98	9.70	6.64	6.87
p_2	3.55	6.14	1.80	8.67	14.86
p_3	—	1.56	1.14	0.85	1.30
E_1 [meV]	1.49	1.43	1.38	1.34	1.28
E_2 [meV]	1.93	1.96	1.96	1.96	1.94
E_3 [meV]	2.38	2.49	2.54	2.58	2.60

Table 3.3: Fitting parameters of Eq.(3.4) for SVP at 1.24 K, and 5, 10, 15, and 20 bar at 0.5 K. Determined with least–χ^2 fits to the inelastic scattering data. $E_{1,2,3}$ is the sum of the energy of two rotons, a roton and a maxon, and two maxons, respectively. These energies are calculated from values in Appendix A of Ref. [Gib96]. The uncertainty of the shown parameters is of the order of the last digit.

wavelength end ($\lambda > \lambda^*$) there is no contribution to the UCN production rate, as there are no more elementary excitations in superfluid helium and the cold beam differential flux drops.

3.4 Temperature Dependence of Multiphonon Scattering

The multiphonon scattering function $s(\lambda)$ has also been extracted for $T = 1.00, 1.60, 1.85$ K at 20 bar. The curves are shown together with the one for 0.5 K at 20 bar in Fig. 3.9. Although the single phonon excitation nearly disappears the multiphonon part does not change within the accuracy of the

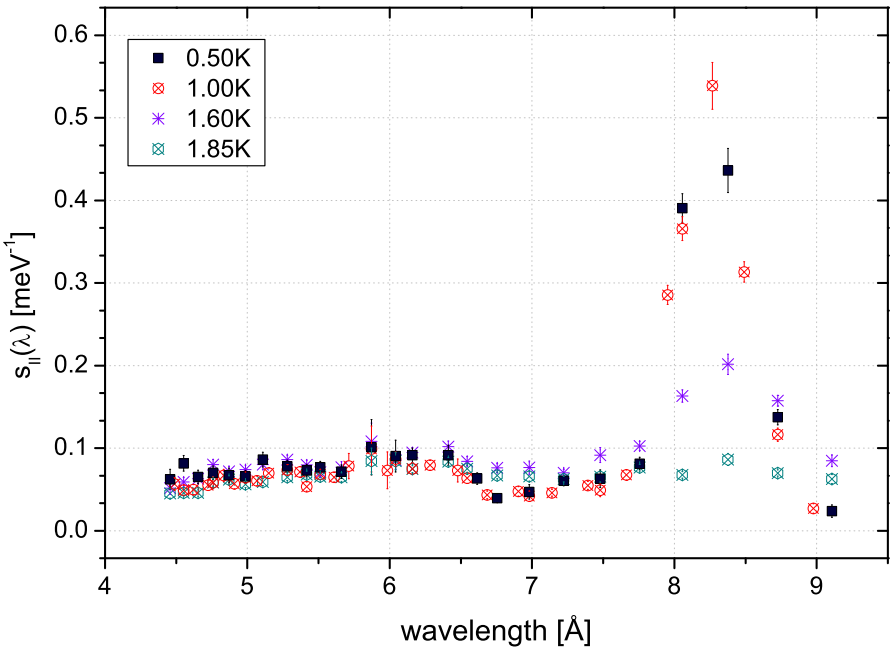

Figure 3.9: Scattering functions $s(\lambda)$ for $p = 20$ bar at $0.5, 1.0, 1.6$ and 1.85 K. Only the single phonon part decreases in intensity — the multiphonon part can be taken as independent of temperature. Width of single-phonon peak is dominated by experimental resolution of the scattering experiment.

measurement. This corresponds very well to the assumption made for the simple subtraction decomposition proposed by Miller and coworkers [Mil62]. They assume the multiphonon component to be independent of temperature.

3.5 Up-scattering

The change in the first velocity of sound, the density, and the Landau parameters imply also a change in up-scattering with pressure. The data from Tab. 3.4 and Eqs.(2.25, 2.27, 2.30) allow to calculate the change. The dimensionless integral I in Eq.(2.28) varies with pressure. There is an overall factor $\alpha(p)^9$ and the last term which depends on $u(p)$. Limits of this term can be obtained by:

$$(2u-2)^2 \leq \left[\sum_{i\neq k} \cos\Theta_{ik} + 2u - 1\right]^2 \leq (2u+2)^2\,,$$

where the neutron is taken to be at rest, and $\sum_{i\neq k}\cos\Theta_{ik}$ is a sum over the angle between all three remaining momenta. Assuming that $\sum_{i\neq k}\cos\Theta_{ik}$ is constant with pressure, an upper (lower) limit for the last term can thus be obtained:

$$\frac{(2u_{\mathrm{p}}\pm 2)^2}{(2u_{\mathrm{SVP}}\pm 2)^2}.$$

For $T = 1.0$ K and 20 bar the up-scattering rates are calculated as in Sec. 2.3.3 using the values from Tab. 3.4:

$$\begin{aligned}\frac{1}{\tau_{\mathrm{up}}}(\mathrm{SVP}) &= \frac{1}{\tau_{1-\mathrm{ph}}}+\frac{1}{\tau_{\mathrm{pp}}}+\frac{1}{\tau_{\mathrm{rp}}} &(3.6)\\ &= \frac{1}{246}+\frac{1}{101}+\frac{1}{369}=\frac{1}{58}\ \mathrm{s}^{-1}\\ \frac{1}{\tau_{\mathrm{up}}}(20\mathrm{bar}) &= \frac{1}{2820}+\frac{1}{26(6)}+\frac{1}{335}=\frac{1}{24(5)}\ \mathrm{s}^{-1}, &(3.7)\end{aligned}$$

with a mean value for the two-phonon processes where the value in brackets is the error derived from the upper (lower) limit.

With increasing pressure the contribution from one-phonon processes decrease and two phonon scattering dominates strongly the up-scattering. The roton-phonon processes change only slightly with pressure. This is due to two counteracting evolutions of the phonon-roton dispersion under pressure.

1. The slope of the phonon part increases and with it the first velocity of sound α. The intersection with the neutron dispersion relation moves to higher energies for the same temperature. Therefor one-phonon processes get negligible whereas the α^5-dependency increases the contribution from two phonon processes at the same temperature.

2. The energy gap Δ of the roton minimum decreases with pressure. The occupation probability of a roton state increases for the same temperature.

The increase in first velocity sound with pressure leads therefore to a non-negligible up-scattering at 20 bar from two phonon processes even at temperatures $T \leq 0.6K$. This requires lower operation temperatures of an UCN source with superfluid helium under pressure to attain same UCN densities as in helium based sources at SVP

pressure [bar]	α [m/s]	u	μ [m_{He}]	Q_{r} [Å^{-1}]	Δ [meV]
SVP[1]	238	2.86	0.1500	1.924	0.7415
5	272	2.61	0.1534	1.969	0.7142
10	301	2.46	0.1334	2.003	0.6872
15[2]	324	2.35	0.14	1.998	0.6600
20	344	2.27	0.1175	2.055	0.6342

Table 3.4: Pressure dependence of first velocity of sound [Vig66] and Landau parameters [Gib96] which are linearly interpolated for $T = 1.0$ K (1 Ref. [Gly95] at 0.9 K, 2 Ref. [Die72] at 1.28 K). The change of the Grüneisen constant u with T is negligible for 0.5 K $\rightarrow$ 1.0 K) (Ref. [Abr70]).

Chapter 4

A versatile cryostat to investigate UCN production

All experiments concerning conversion of CN to UCN in superfluid helium require a cryostat. Its main task is to provide a large volume of ^{4}He at temperatures below 0.7 K, to reduce losses through up-scattering (see Sec. 2.3.3). This volume has to be mounted in a way that it can be exposed to an incident beam of cold neutrons, without activating the whole apparatus. If experiments with UCN are not performed inside the helium, installations have to be foreseen to guide the produced UCN from the filled helium volume to the experimental setup at room temperature outside of the cryostat. In this chapter I describe the cryostat which has been developed to produce UCN and then extract them to a vacuum at room temperature. In Chapter 5 measurements are describe using this apparatus investigating the extraction of UCN to vacuum. For measurements of the UCN production rate in superfluid helium under pressure, described in Chapter 6, only the UCN production volume was changed to withstand pressures of up to 50 bars.

4.1 Cooling a large volume of He-II

Cooling a large volume of He-II to temperatures of 0.5 K–1.0 K requires either a dilution refrigerator, or a ^{3}He evaporation stage (0.5 K stage). Dilution refrigerator are well adapted for small samples to reach very low temperatures ($T < 0.3$ K) but have limited cooling power, and are more complicated in design. With a sole ^{4}He evaporation stage (1.0 K stage) it is difficult to reach temperature below 1.0 K as the latent heat of evaporation is too small. For our purpose the best-adapted technique is the use of ^{3}He in an evaporation stage. The cooling power can thus be easily increased with pumping speed.

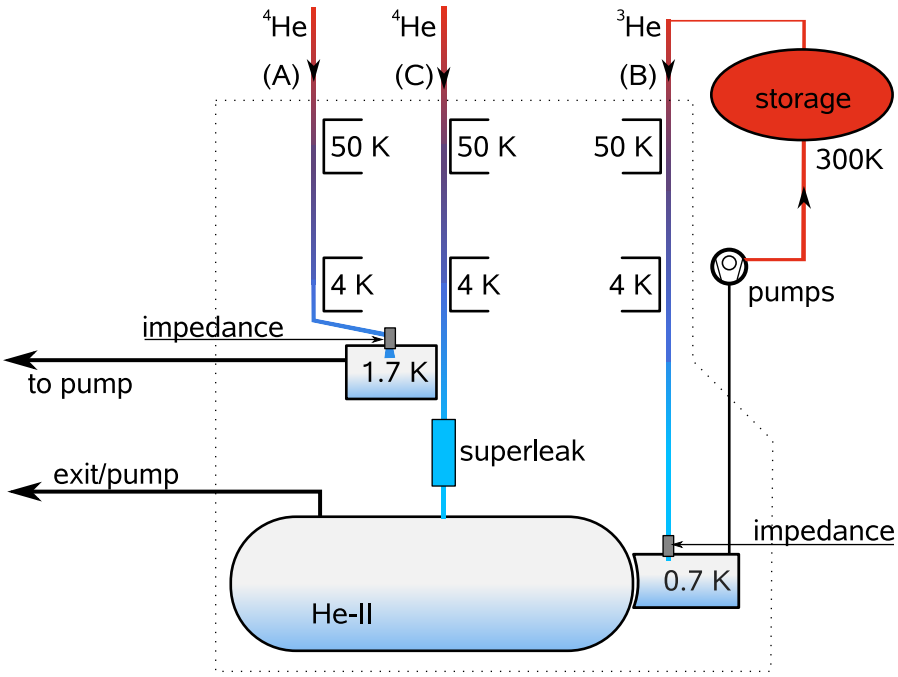

Figure 4.1: Sketch of the cryogenic system of the prototype cryostat. Only the thermal coupling to the cryo cooler is shown (50 K and 4 K) for the two refrigeration cycles and the converter helium cycle. (A) ^{4}He cooling line: the gaseous helium is precooled (50 K), liquefied (4 K), and then pumped on to provide $T_{\mathrm{He-4}} \approx 1.7$ K. (B) ^{3}He cooling cycle: the gaseous helium from a storage balloon is precooled (50 K), liquefied at the 4 K stage which reaches $T \leq 3.3$ K if only operated with ^{3}He, and then pumped on to provide $T_{\mathrm{He-3}} \approx 0.7$ K before it returns to the storage balloon. (C) Converter filling line: Gaseous ^{4}He is precooled (50 K), liquefied (4 K), and then further cooled to $T \approx 1.7$ K by the first cooling line (A). Then it passes through the superleak before it is cooled by the ^{3}He evaporation stage (cycle B) to $T \approx 0.7$ K.

A cooling scheme of the prototype cryostat is shown in Fig. 4.1. As final refrigerator for the converter we use a ^{3}He evaporation stage. Prior to this a commercial cryo cooler is used to liquefy helium and then a ^{4}He evaporation provides temperatures below the λ-point ($T_\lambda = 2.17$ K). Typically a temperature of $\lesssim 2$K is needed to pass helium through a superleak for purification.

4.2 The cryogenic apparatus

The assembled cryostat during experiment is shown in Fig. 4.2 and its simplified schematic cross section in Fig. 4.3. It consists of the main cooling tower

and in this specific case of the prototype production volume with ultracold neutron extraction guides. Cold neutrons enter through a series of windows and pass through the entire production volume before they exit on the far end. Their are two remarkable innovations: first, the sole use of gaseous helium, which is liquefied inside the cryostat [Sch06]; second a cold UCN valve for the storage of UCN prior to their windowless extraction. Furthermore, a variety of external infrastructure is needed to operate the cryostat. In this section details of these parts are presented.

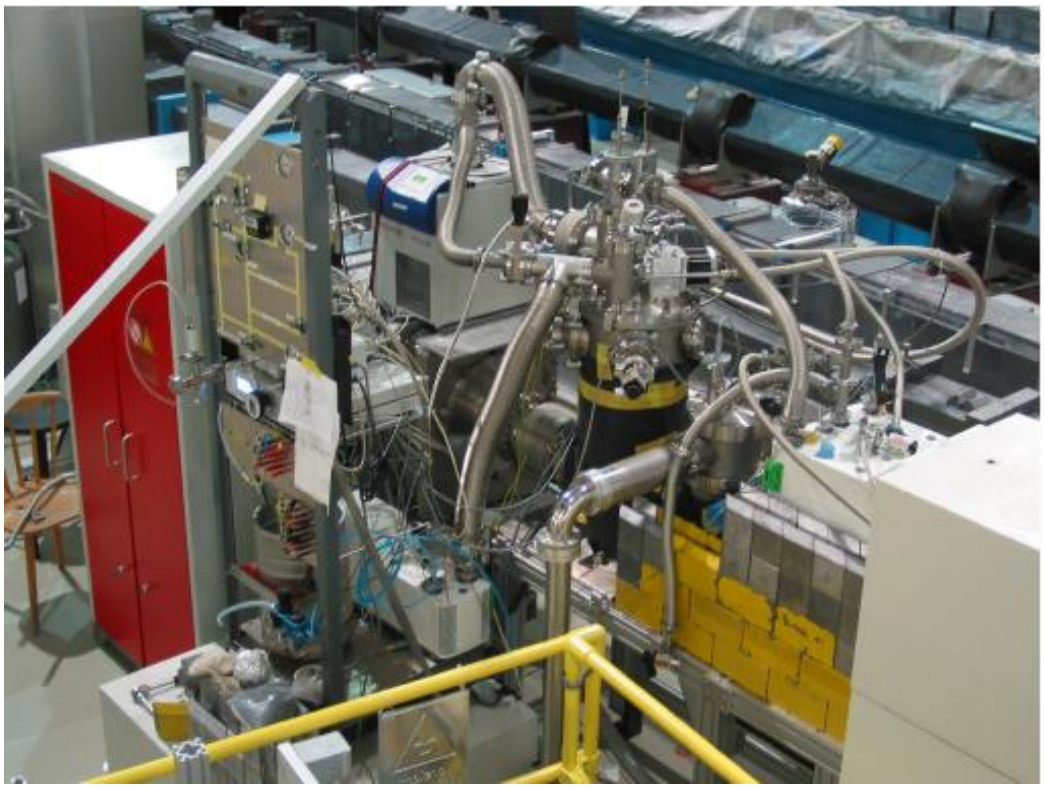

Figure 4.2: Overall view of the prototype cryostat at the LN1 beam line of the "Neutronenquelle Heinz Maier-Leibnitz".

Gifford McMahon cryo cooler

A dry, compact cryostat design was made possible thanks to the cooling power 1.5 W at 4.3 K of a commercially available Gifford McMahon cryo cooler (Sumitomo model SRDK415D with compressor CSW-71D), which is fixed to the top flange. Thus helium is liquefied inside the cryostat and an external liquid helium supply from a storage dewer becomes dispensable. Additionally it provides the cooling power to cool the main radiation shielding of the cryostat. The primary heat screen is connected to the 1st stage of the cold head with a nominal power of 40 W at 50 K. All connections to parts at

lower temperatures inside the screen are heat anchored here to reduce heat conduction. The cardinal task of the 2nd stage is the liquefaction of ^{3}He and ^{4}He. Apart from that it also serves for cooling two heat switches and the inner heat screen to ~ 4 K.

^{4}He cooling cycle

The ^{4}He cooling cycle serves to cool the incoming helium for the converter volume below the λ-transition temperature. It can also be used with a separate capillary to further precool ^{3}He.

Helium is supplied by a standard 50 litre 200 bar gas cylinder. With a needle valve, a lock-off valve and a gas flow monitor at room temperature the input gas flow is controlled. It passes an external cryo trap at liquid nitrogen temperature before it enters the cryostat via the top flange. For liquefaction of gaseous helium, efficient precooling is required because the specific enthalpy of ^{4}He between 295 K and 4.2 K sums up to 1540 J/g (for detailed description of liquefaction with this apparatus see [Sch06]). After it passes a second, internal cryo trap at 50 K it enters the spiral heat exchanger connected to the first stage regenerator of the Gifford McMahon cryo cooler. In a spiral attached to the second stage of the cryo cooler the helium is finally liquefied at temperatures $T \leq 4.2$ K. From there it is guided through a thin capillary to the volume of the evaporation stage. Two spirals from thin capillaries in the liquid are used to cool the helium of the converter supply line and the ^{3}He of the ^{3}He cooling cycle, respectively. A temperature below 2 K is required to operate the superleak reliably. A needle valve soldered to the end of the capillary just above the liquid is used to control the impedance. A pump with a nominal pumping speed of 40 m^3/h sucks on the surface of the liquid and thus reduces the temperature to ~ 1.7 K. Eight copper buffles, with increasing reflection area towards the liquid helium surface are used, to minimise the radiation input via the pumping tubes. For a faster cool down the evaporation stage is coupled with an active coldswitch, similar in design as described in Ref. [Tor84] but for gaseous helium, to the 2nd stage of the cold head.

^{3}He cooling cycle

The ^{3}He evaporation stage is designed to cool the superfluid ^{4}He inside the converter volume to its final temperature of $T_{\mathrm{UCN}} \leq 0.7$ K. As ^{3}He is a rather expensive isotope (200 Euro/litre at standard conditions) it is circulated in a closed cycle. A gas handling system, described and sketched in Fig. 4.4, is used to control the gas flow in the system. A cascade of 2 dry roots blower pumps backed with a dry roughing pump (nominal pumping speed: 2000 m^3/h, 500 m^3/h, 40 m^3/h) sucks on the ^{3}He bath. Before the gas enters

the cooling tower it is cleaned with an external liquid nitrogen trap. Inside the cooling tower it passes another cryo trap at the temperature of the outer heat screen, before it is liquefied inside the condenser attached to the cryo cooler. Thereafter it passes through the ^{4}He evaporation stage where it is cooled further. An adjustable impedance allows to use a high cold gas flow to reduce cooling time. Once the liquefaction temperature ($T_{\mathrm{He3}} = 3.19$ K) is reached on can fine tune the impedance for continuous operation. A heat exchanger made of a copper plate with a hole array on each side (see Fig. 4.5) providing an effective contact area of 200 cm^2 transfers the cooling power from liquid ^{3}He to ^{4}He. Again, for a faster cool down the evaporation stage is coupled with an active cold switch to the 2$^{\mathrm{nd}}$ stage of the cold head.

^{4}He UCN converter supply

This cooling line serves to provide isotropically pure He-II for the UCN converter volume. The gaseous helium is supplied from a standard 50 litre 200 bar gas cylinder and passes a liquid nitrogen cold trap before it enters the cryostat via the top flange. The liquefied ^{4}He is cooled to a temperature below the λ-transition point with the ^{4}He evaporation stage. Thus the superfluid helium can pass through the superleak, where all impurities including ^{3}He stay back, into the converter volume. The converter volume is connected to the ^{3}He evaporation stage with a "U"-shaped copper tube with inner diameter 10 mm. The copper allows to cool down the converter volume even before it is filled with liquid. Once it is filled the high heat conductivity of superfluid helium guarantees efficient cooling of the entire volume.

Superleak

Natural Helium contains a fraction of $\sim 10^{-6}$ of ^{3}He. As ^{3}He has a very high thermal neutron absorption cross section (5333 barn) the storage time of the conversion volume filled with non-purified helium would be below 1 s. To reduce the ^{3}He level to $\leq 10^{-11}$ a superleak is used. It is made of a porous material which is tight for any gas or liquid, but "leaks" for superfluids. In the described cryostat we employ a superleak made from a stainless steel tube with inner diameter 7 mm filled with hammered Al_2O_3 powder with grain size 50 nm on a length of 150 mm (see Fig 4.6a). A second outer shell filled with superfluid helium cools the powder evenly. As ^{3}He becomes superliquid only at 2.5 mK it cannot pass through.

Cold switches

Both evaporation stages require to be completely decoupled during operation at final temperatures to reduce heat input from warmer places (4 K at 2$^{\mathrm{nd}}$

stage of cold head). A permanent isolation would inescapably increase cool down times for the whole cryostat, as these stages are then only cooled by radiation or with cold helium flowing through the adjustable impedance. To decrease cool down times by a factor two we employ two cold switches (see Fig. 4.6b) between the 2^{nd}-stage of the cryo cooler and both evaporation stages. The additional ineluctable heat load to the 2^{nd} stage from the necessary heaters is controlled by adjustable heating currents.

4.3 Operation

This section is addressed to users of the cryostat.

Prior to operation each part of the apparatus has to be leak tested at least once. It is also advisable to check tightness each time a capillary system is closed. This is most conveniently done by a sniffer test with the capillary under pressure. The starting point of this description is the connection of the UCN converter volume with the cryostat unit. The UCN extraction part is not described here as it depends strongly on the performed experiment and the setup used. I discuss here a typical cool down curve as it was registered during measurements described in Chapter 5, published in [Zim07] using a UCN volume of ~ 2000 cm^3 (see Fig. 4.7).

Assembly of cryostat and production volume

1. The UCN vessel is mounted inside the 2^{nd} heat screen. Small legs made from Teflon can be used as support. For a minimum heat conduction it is important to keep the contact area between the screen and the legs very small. A connection tube, shaped like an "U", connects the bottom part of the ^{3}He evaporation stage with the vessel (indium seal). This part is due to changes as the vessel itself changes, only the side connected to the cryostat is predefined. For a better cooling the "U"-piece is thermally anchored to the ^{3}He stage.

2. Close all heat screens. The 4 K heat screen is closed on the cold neutron entrance and exit side. Thereafter the outer screen is closed including the bottom plate.

3. Seal all accesses to the cryostat and connect the main vacuum pump. Open the valve to the main isolation vacuum and pump with the main vacuum pump until an isolation vacuum of 10^{-5} mbar is reached ($\sim$ 4 hours). Leave the valve to the ^{3}He cycle open to evacuate it. In addition the ^{4}He pump has to be turned on. Otherwise gas remnants will freeze out inside the Joule-Thomson stage. The valve connecting ingoing and outgoing side of the ^{4}He cycle needs to be open.

Cooldown and steady operation

1. Connect the cold head to the compressor according to the manual (this can also be done in advance). Turn on the water supply for the compressor and switch on the compressor. If there is a grinding noise turn off the compressor immediately (typically at room temperatures above 302 K). Try to cool the 2^{nd}-stage of the cryo cooler below 300 K.

2. Turn on all heat switches to guarantee the cooling of thermally separated parts. A heating current of 1 mA is sufficient to maintain the helium inside the switches. Turning off the current at $T_{2\text{nd}} \leq 10$ K will result in cooling the adsorption reservoir (see Fig. 4.6b) to the temperature of the 2^{nd} stage. This acts like a cryo-pump and will result in a thermal lockoff. Be sure not to turn off the currents before the desired temperature are reached.

3. After $\sim$ 24 hours the outer heat screen will have reached a stable temperature of $\sim$ 50 K. The temperature of the 2^{nd} stage is 6.5 K. After $\sim$ 70 hours the temperarues of the UCN-Volume and the 1K-Pot are stable at $\sim$ 9.5 K. The temperature of the 2^{nd} stage has dropped to 4 K.

4. From now on the ^{4}He Joule-Thomson stage can be used for further cooling. In Fig. 4.7 further cooling down was started 44 hours later only for experimental reasons. First the helium gas cylinder is opened, the pressure reduction valve is adjusted to approximately 2 bar and the main lock-off valve is opened. With the needle valve one adjusts the flow shown on the flowmeter to $\sim$ 25 g/h. The temperature of the ^{4}He stage falls rapidly below the temperature of the 2^{nd} stage.

5. Now one can also open the helium supply to the UCN converter volume. First the helium gas cylinder is opened. Then the pressure reduction valve is adjusted to approximately 1 bar and the main lock-off valve is opened. This will probably lead to an abrupt rise in temperature of the ^{4}He stage. This is the remaining heat of the superleak.

6. To open the superleak a steady temperature below 2.17 K is necessary. Slightly open the needle valve to regulate the ingoing ^{4}He. A temperature of 1.6 K can be reached by optimising the needle valve position and the ingoing pressure. Here it is important to be patient until the superleak opens, which is obviously the case when the temperature of the ^{3}He stage drops to $\leq$ 2.17 K as the superfluid helium passes the heat exchanger.

7. Over a period of $\sim$ 28 hours the UCN volume is filled with purified ^{4}He while its temperature is hold at $\sim$ 1.4 K. The temperature of the outer heat screen rises slightly due to the additional thermal load caused by

the helium used for cooling and filling the volume. After the volume is filled completely the helium supply to the ^{4}He evaporation stage is cut. Its temperature rises to the same level as the outer heat screen thus blocking helium transfer through the superleak.

8. After $\sim$ 139 hours we start to circulate ^{3}He in the closed cycle, pumping on the ^{3}He Joule-Thomson stage only with the roughing pump (40 m^3/h) and the small roots blower pump (500 m^3/h). During the following 74 hours we performed measurements at constant temperature without further cooling down the helium converter.

9. At temperatures around $\sim$ 1.4 K the helium loss rate out of the volume is still in the order of 5 g/h. It decreases steeply, when the Helium is cooled below 1 K.

10. To cool the converter volume down to $\sim$ 0.7 K, we start after $\sim$ 149 hours the big roots blower pump (2000 m^3/h). A steady state flowrate for ^{3}He of $\sim$ 75 g/h is achieved.

11. To achieve lowest temperatures, it is necessary to turn on the heating of the superleak, thus blocking it and to evacuate the ^{4}He cycle. Otherwise the superliquid helium inside the superleak will act as thermal short cut between both Joule-Thomson stages.

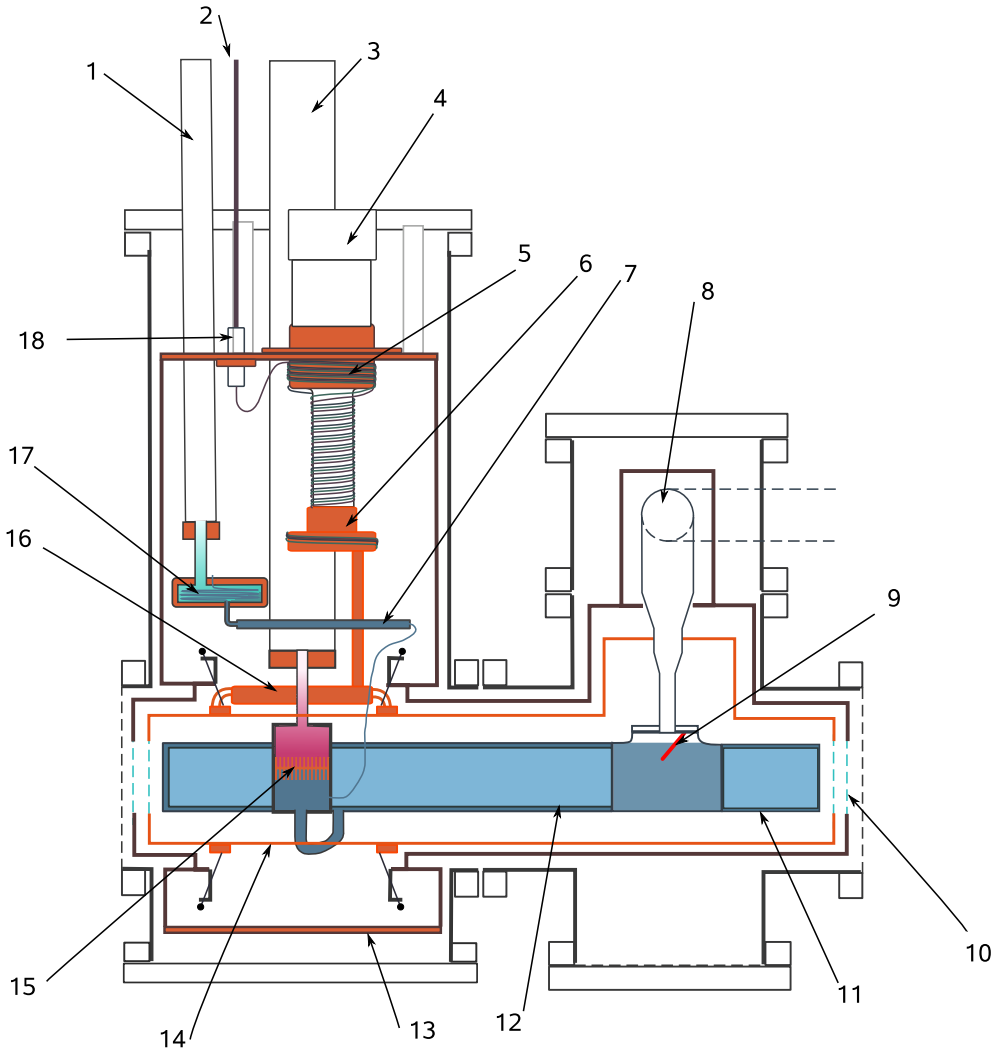

Figure 4.3: Simplified sketch of the cryostat with converter volume and extraction chimney. Pump line (1) to ^{4}He pump, (2) gas inlets (two ^{4}He feeds and one ^{3}He), (3) to ^{3}He circuit pumps, (4) cryo cooler, (5) 1$^{\text{st}}$ stage of cold head ($\sim$ 50 K), (6) 2$^{\text{nd}}$ stage of cold head ($\sim$ 4 K), (7) horizontal superleak, (8) extraction chimney, (9) UCN cold valve, (10) aluminium windows (both sides of the converter volume), (11) ^{4}He vessel made of aluminium, (12) converter volume made of polished stainless steel, (13) outer heat screen ($\sim$ 50 K), (14) inner heatscreen ($\sim$ 4 K), (15) ^{3}He evaporation stage with copper heat exchanger to ^{4}He ($\sim$ 0.7 K), (16) cooling connection from 2$^{\text{nd}}$ stage of cold head to inner heat screen, (17) ^{4}He evaporation stage with spiral capillary heat exchanger, (18) cryo trap for all three gas feeds (only one is drawn).

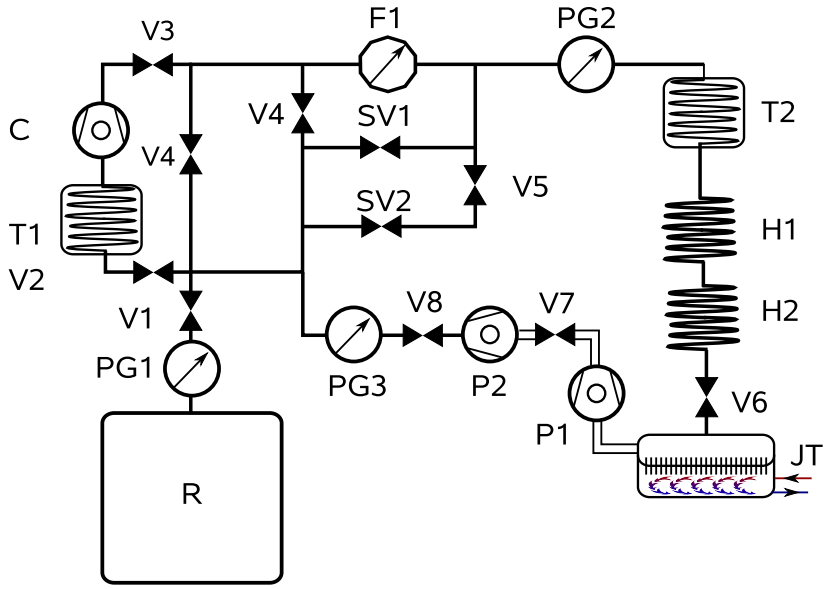

Figure 4.4: Flowchart of ^{3}He cycle: In operation the lock-off valve V1 of the reservoir R is open, its pressure is monitores with gauge PG1. Valve V4 is closed whereas valves V2 and V3 are open. Thus the gas is purified inside the liquid nitrogen cryo trap T1 before it is compressed with the compressor C to $\sim$ 2 bar. The bypass valve V4 is closed as well as valve V5 which enables a lower maximal pressure. The both security valves SV1 and SV2 are adjusted to open at 3 bar, 1 bar respectively. The flow meter F1 and the pressure gauge PG2 allow to control the ingoinggas flow. Inside the cryostat the gas passes another cryo trap T2 before it is cooled and subsequently liquefied in the heat exchangers H1 and H2 attached to the cryo cooler. Inside the ^{3}He evaporation pot the needle valve V6 allows the adjustment of the flow impedance into the helium bath. A cascade of 2 dry roots blower pumps (P1, P2) backed with a dry roughing pump (P3) sucks on the surface of the ^{3}He-bath and thus lowers its temperature. Pressure gauge PG3 monitors the pressure after the pumps. With the valves V7 and V8 the cycle can be shut off on the back side of the evaporation stage.

Figure 4.5: Heat exchanger inside the ^{3}He evaporation stage. Right: copper plate with hole array inside the stainless steel housing of the evaporation stage. Left: bottom flange of the exchange volume, which will be connected to the converter volume via a copper tube in "U"-shape.

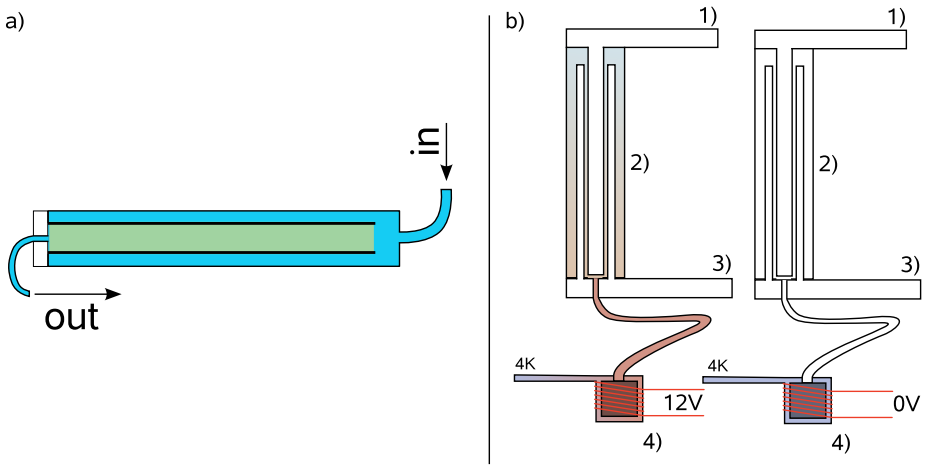

Figure 4.6: (a)Sketch of superleak: The superfluid can pass through the superleak, whereas non-superfluids and impurities stay behind. The inner part, made from hammered Al_2O_3 powder, is surrounded by He-II for better cooling. (b) Sketch of a cold switch: During operation the heater of the adsorption volume (4) is on, so that the gas fills the switching volume (2) made from a copper finger inside a copper cylinder surrounded by athin stainless steel tube. The gas serves as heat conductor between the warm part connected to (3) and the cooled part (2^{nd} stage of cold head) connected to (1). If the heater is turned off, the cold head cools the adsorption volume (4) which adsorbs all gas in the switch. There is no more helium left inside the switching volume, thus the heat connection is cut and the part connected to (1) can be cooled below the temperature of the part connected to (3).

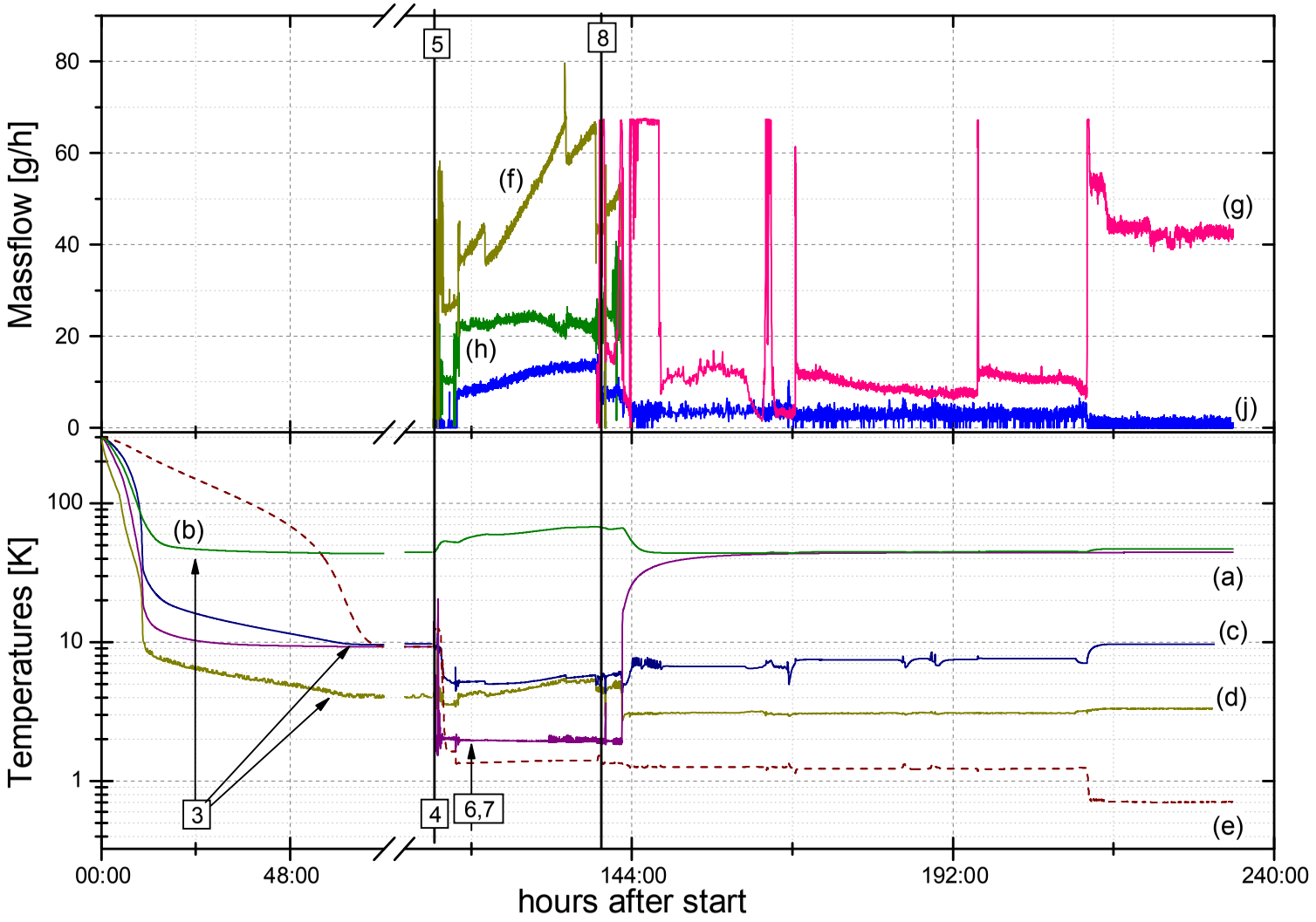

Figure 4.7: Typical cooldown and continuous operation of the prototype cryostat. Narrow peaks result from abrupt pressure changes and the flow meters getting out of range. All numbers refer to the enumeration in "Cooldown and Operation". The temperatures are given for: (a) ^{4}He evaporation stage, (b) 50 K heat screen, (c) UCN extraction tubing, (d) 2nd stage of the cryo cooler, (e) UCN volume. The flow is given for: (f) "in" converter volume, (g) ^{3}He circulation, (h) ^{4}He evaporation stage, (j) "out" converter volume.

Chapter 5

Experiments on the extraction of UCN from superfluid helium

The aim of the two experiments at the "Neutronenquelle Heinz Maier-Leibnitz", Garching was to show that the designed prototype cryostat works, that it is possible to extract UCN from superfluid helium without significant losses, and to investigate and compare two different type of converter vessel coatings. These experiments [Zim07, Zim08] have been performed in 2006/2007. The converter vessel was made of polished stainless steel. In this chapter I will describe the second experiment from spring 2007 where the conversion volume was coated with Fomblin grease.

5.1 Experimental setup

The cryostat described in Chapter 4 was used for all measurements. The specific equipment of the experiments (see Fig. 5.1 and Fig. 5.2) are the UCN converter vessel, a cold valve, and tubing for UCN extraction. The vessel has a volume of about 2.4 litres. It is made from electropolished stainless steel tubes with total length 696 mm and inner diameter 66 mm. The calculated neutron optical potential is $V_c = 184(4)$ neV. It is connected via a copper tube, in the shape of a "U", to the coldest stage of the cryostat. During experiment this tube is filled, like the entire conversion volume, with purified superfluid helium (He-II). This guarantees an optimal thermal coupling of the converter to the refrigerator.

For the second experimental run the volume was coated with Fomblin grease (Solvay Solexis RT15) ($V_c \approx 115(10)$ neV)[1] evenly spread on the walls with latex gloves. This defines, after subtraction of the Fermi potential of the

[1] As the mixing ratio of Fomblin oil and Teflon is unknown I take their mean value $V_c = 106.5$ [Pok03] and $V_c = 123$ [Bod08], respectively.

superfluid helium ($V_F \approx 18.5$ neV), the maximum kinetic energy of storable neutrons. Fomblin is a hydrogen-free perfluoropolyether (PFPE) oil normally used as lubricant in high vacuum applications. It became very popular as wall coating in neutron lifetime measurements [Mam89, Arz00, Ser05] due to its extremely small UCN loss rate per wall collision ($\eta \approx 2.35 \cdot 10^{-5}$ at 21° [Pok03]). Fomblin grease ($\eta \approx 1.85 \cdot 10^{-5}$ [Pok03]) is made by adding polytetrafluoroethylene (PTFE) to the liquid oil. At low temperature it becomes brittle and the smooth surface cracks into many small flakes.

The incident cold neutron beam passes through two 0.125 mm thick Ni foils ($V_c \approx 252$ neV) which close off the vessel on both sides. The valve for UCN extraction is situated above the superfluid helium in a "T"-section of the vessel. It can be manipulated from outside via a bellows-sealed capillary. With the valve open, UCN may exit through a 70 mm long vertical pipe with inner diameter 16 mm. The subsequent extraction line (5 in Fig. 5.1) consists of tapered transitions to diameter 50 mm, followed by a 90° bend, then a horizontal 300 mm long straight guide, a conical section expanding to diameter 66 mm, then another 90° bend, and finally a vertical 1 m long straight section down to a ^{3}He gas UCN detector. All UCN guides are made from electropolished stainless steel tubes manufactured by NOCADO[2].

The apparatus was installed 1.7 m behind the exit of the cold neutron guide "NL1". The beam was collimated from diameter 60 mm down to diameter 33 mm at the entrance of the apparatus, thus defining an UCN production volume of $V_p = 595$ cm^3. The neutron particle flux density determined at this point by gold foil activation was $1.5 \cdot 10^9$ cm^{-2}s^{-1} for a mean neutron wavelength of 5.3 Å. At the end of the measurements the cold neutron spectrum was measured at the position of the entrance window of the converter vessel. A time-of-flight analysing device described in Ref. [Zei06] was used for this purpose. It consists of a mechanical chopper and a ^{3}He detector with a vertical slit. During a measurement the detector is moved horizontally to integrate over the whole divergence of the beam. In this way the wavelength spectrum was determined up to 20 Å. In Fig. 5.3a the spectrum, calibrated with the gold foil measurement, is shown for $\lambda \leq 10$ Å.

5.2 Measurements

Fort the investigation of UCN production and extraction three different kinds of measurements have been carried out:

- **Build-up mode (Fig. 5.4)**
  Cold neutrons irradiate the converter while the UCN valve is closed for

[2]For more information on NOCADO stainless steel tubes see: http://www.nocado.com/.

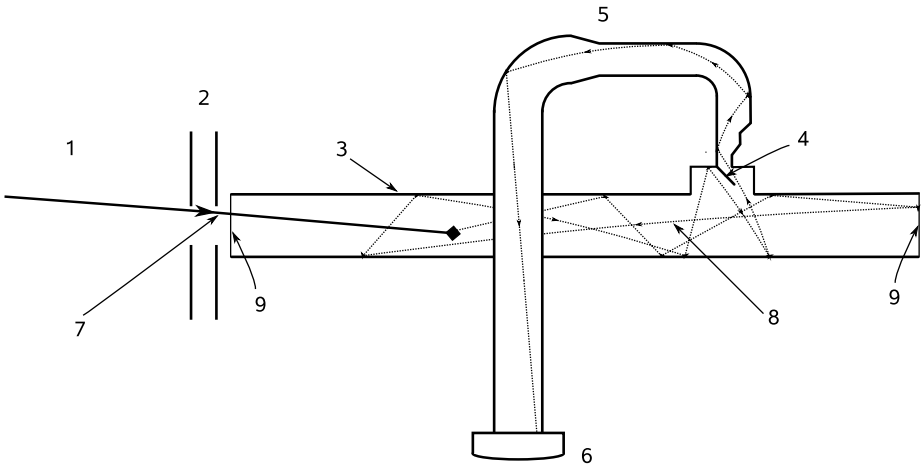

Figure 5.1: Schematic view of the setup for experiments on UCN extraction. Cold neutrons (7) from the guide (1) enter the conversion vessel (3) through aperture (2) to define a beam diameter of 33 mm. They pass through a nickel foil (9) before they may interact with the liquid and became ultracold neutrons (8). After a time of storage the cold valve (4) is opened, the UCN pass through the extraction tubing (5) and are detected in a ^{3}He detector (6).

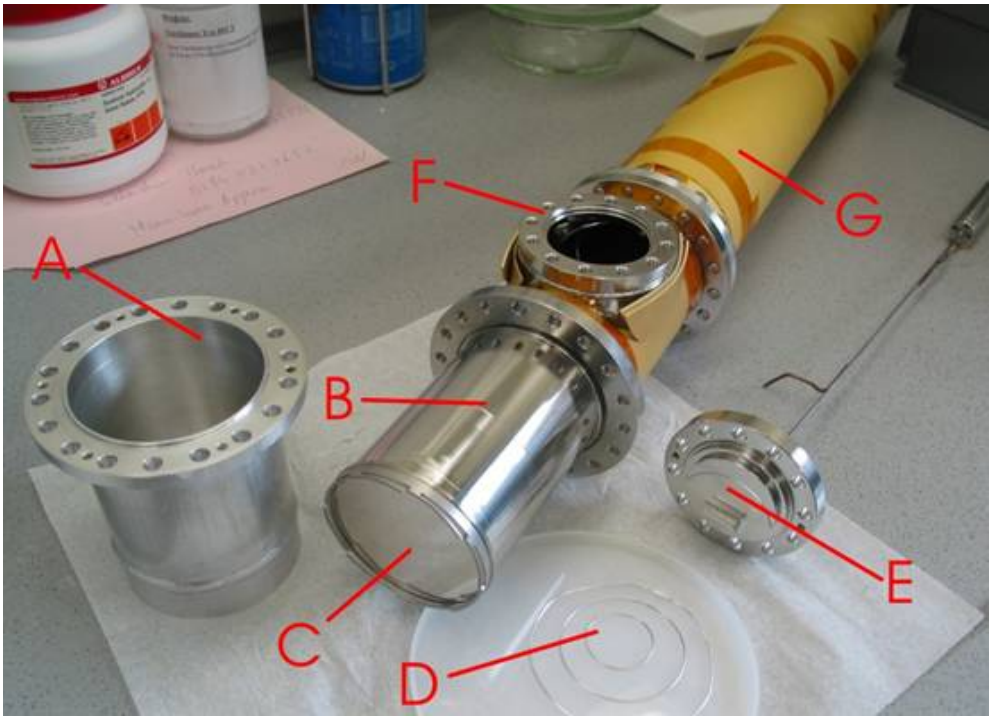

Figure 5.2: Photograph of converter vessel parts. The outer shell is made from aluminium (A), whereas the converter inner volume (B) is made from stainless steel and is closed off on both ends with nickel foils (C). The "T"-piece (F), where the extraction tubing and the UCN valve (E) are connected is also made from stainless steel. The whole vessel is wrapped in ^{6}Li-rubber to capture scattered cold neutrons.

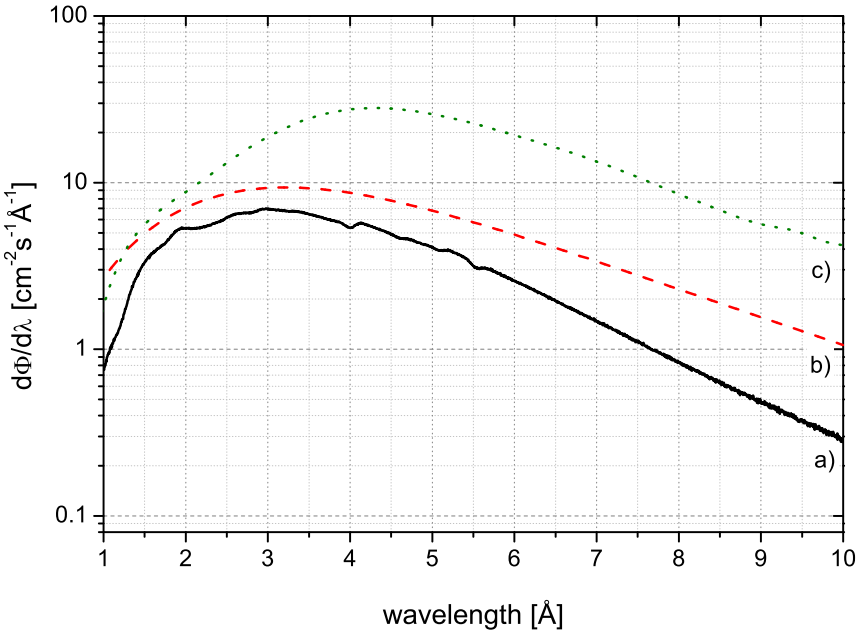

Figure 5.3: Differential cold neutron fluxes. (a) Measured cold neutron differential flux of LN1 at the "Neutronenquelle Heinz Maier-Leibnitz", Garching. (b) Spectrum of PF1b at the Institut Laue Langevin (ILL), Grenoble, calculated with Eq.(11) of Ref. [Abe06]. (c) Simulated spectrum of H172 of the ILL, at the position of the long-wavelength monochromator for UCN production.

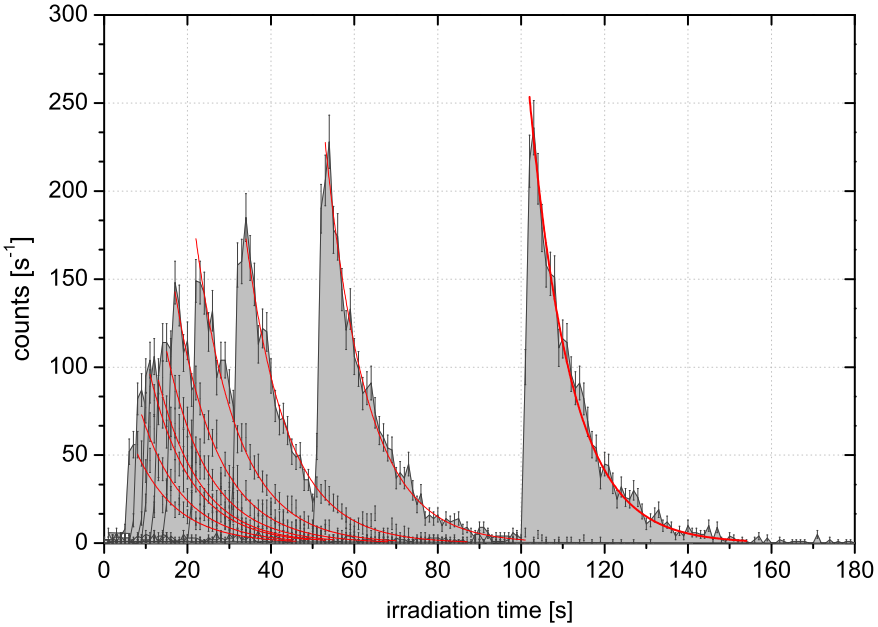

Figure 5.4: Typical "build-up" measurement here at 1.26 K. The red lines are fits of exponential decays to the emptying curves.

a time t_0. After this time the beam is shut off and the valve is opened simultaneously. UCN are counted as a function of time with the ^{3}He detector. This type of measurement is performed for 4 s $\leq t_0 \leq$ 500 s.

- **Continuous mode (Fig. 5.5)**
  The UCN valve is continuously open. At $t = 0$ s the irradiation of the converter with cold neutrons starts. At $t = t_\mathrm{i}$ the cold beam is shut off. UCN are counted as a function of time.

For UCN produced at 0.82 K inside the Fomblin-coated vessel a storage experiment was additionally performed:

- **Storage mode (Fig. 5.6)**
  Cold neutrons irradiate the converter while the UCN valve is closed for a constant time t_i. Then the beam is shut off and the UCN are kept inside the closed vessel. After a holding time t_h the cold valve is opened, and the remaining UCN are counted as a function of time.

Although the opening and closing of the cold neutron shutter and the UCN shutter were automatise and reproducible an ambiguity in the absolute definition of time of < 0.8 s remained.

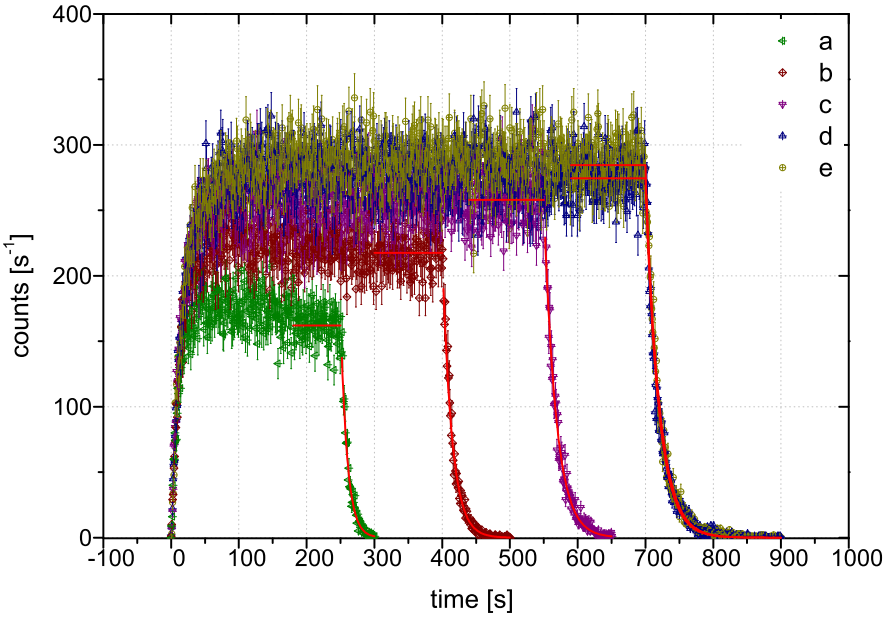

Figure 5.5: Continuous extraction of UCN for five different temperatures (a) $T = 1.26\ K$, (b) $T = 1.15\ K$, (c) $T = 1.04\ K$, (d) $T = 0.93\ K$, and (e) $T = 0.80\ K$. Irradiation was started at $t = 0$ and stopped at different times, but always when the count rate was in saturation.

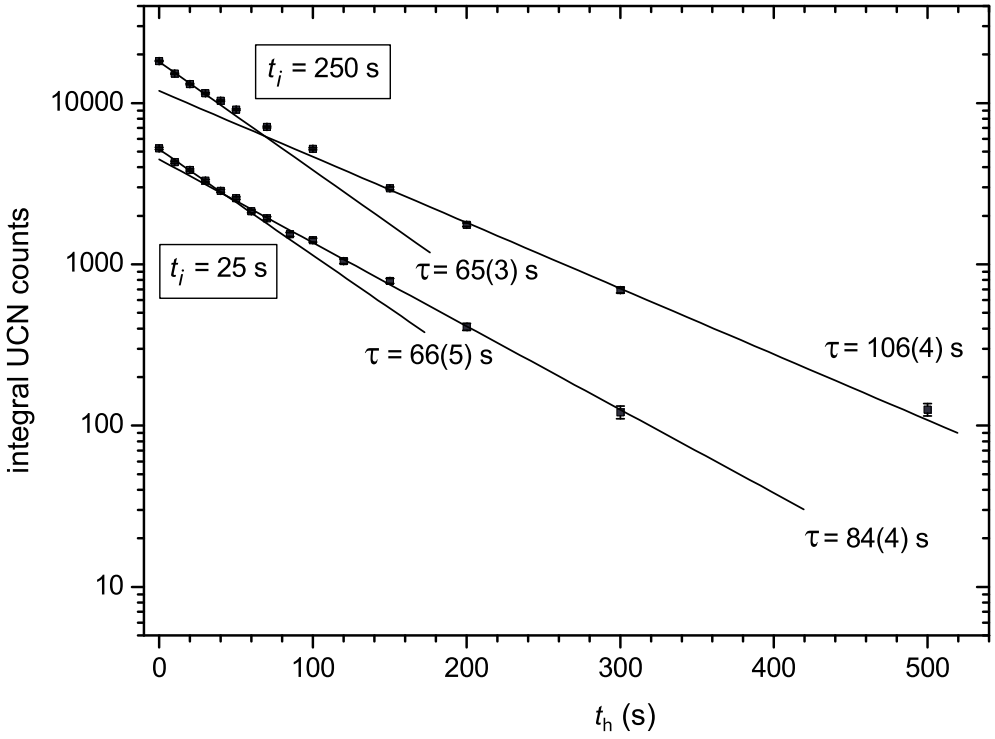

Figure 5.6: Integral UCN counts as a function of holding time t_{h} at 0.82 K. The converter was irradiated for 25 s (lower curve), 250 s (upper curve) with cold neutrons. The exponential fits to subsets of data demonstrates the change in loss rate $1/\tau$ with holding time t_{h}.

The background in the UCN detector with closed cold neutron shutter was measured several times during the experiment. It was below 0.001 s^{-1}, and is therefore neglected in the following analysis.

5.3 Data analysis

The converter produces low energy neutrons with a broad spectrum of energies. Only those with energies below $V_c(\text{wall}) - V_F(^4\text{He})$ can be stored inside the conversion volume. Neutrons with larger energy will in most cases escape the vessel after a time much shorter than the typical operation times of shutters in the experiments. However, a small fraction of so-called overcritical UCN will contribute to the countrate $\dot{N}$ with open UCN shutter in the continuous measurements. During storage the spectrum of the UCN is changing continuously with time due to energy dependent loss processes. The average loss probability per wall collision is largest for neutron energies close to the wall potential. Furthermore, the wall collision frequency increases with neutron velocity. Only in cases where energy dependent losses are small compared to other loss mechanisms the storage of UCN can be described with an exponential decay with one single time constant τ. This is only the case at sufficiently larger temperatures where the energy independent up-scattering loss rate dominates the total loss rate.

The extraction efficiency can be estimated from the fraction of UCN counted and the number of UCN expected from theoretical calculations described in Sec. 3.3. In addition Monte Carlo simulations with Geant4UCN [Atc05b] have been performed to better understand the statistical processes in the converter and during extraction. However, they are not used within the analysis to deduce quantitative results.

5.3.1 Time constants

The storage and the extraction of UCN can be characterised by several parameters. The storage lifetime τ describes the temporal decrease of UCN density in the closed converter vessel. The decay rate

$$\tau^{-1}(E,T) = \tau_{\text{l}}^{-1}(E) + \tau_{\text{up}}^{-1}(T) + \tau_{\beta}^{-1}, \tag{5.1}$$

contains: energy dependent contributions $\tau_{\text{l}}^{-1}(E)$ from absorption by impurities inside the converter, on the wall surface, or from losses through holes; temperature dependent up-scattering (see Sec. 2.3.3), and the β–decay of the neutron. A second parameter is the emptying time τ_{e} describing the temporal decrease of UCN counted after opening the neutron valve. The emptying

rate is described by:

$$\tau_{\mathrm{e}}^{-1}(E,T) = \tau^{-1}(E,T) + \tau_{\mathrm{ext}}^{-1}(E), \tag{5.2}$$

where τ_{ext} is the time constant for an UCN passing through the exit hole and the extraction tubing. In an ideal system, where neutrons are not back-reflected into the storage volume or stored during extraction, and in the approximation that UCN behave as an ideal gas it is inverse proportional to the surface area of the exit hole.

From these time constants we may derive the probability W to detect an UCN produced in the converter volume. It can be calculated by:

$$W = \epsilon \frac{\tau_{\mathrm{e}}}{\tau_{\mathrm{ext}}} \tag{5.3}$$

where ϵ is a factor describing losses due to imperfections in extraction and detection.

5.3.2 Continuous and build-up measurements

Both time constants, τ and τ_{e} are measured in the "build-up mode". The storage lifetime is derived from the increase of UCN counts with irradiation time. In the case where the loss rate is dominated by energy-independent processes the data can be fitted to the function:

$$N(t_{\mathrm{i}}) = N_{\infty}\left(1 - e^{-\frac{t_{\mathrm{i}}}{\tau}}\right) + A \tag{5.4}$$

where N_{∞} is the UCN count rate for $t_{\mathrm{i}} \to \infty$ and A an irradiation-time independent fraction. This fraction is interpreted as overcritical marginally trapped neutrons produced just before opening the UCN shutter and closing the cold neutron shutter. It might also include directly scattered cold neutrons if there is an overlap in opening and closing of the two shutters. The increase of A with decreasing temperature should be negligible, as the losses of overcritical UCN from the volume are dominated by temperature independent wall processes. Simulations with Geant4UCN have been made to investigate the energy dependency of the extraction for neutrons with initial energies $E \leq 500$ neV. They indicate that a large fraction of the counted neutrons have energies above the optical potential of the converter vessel and below the optical potential of the material from which the extraction tubing is made.

The temperature dependence of UCN accumulation is shown in Fig. 5.7. Additionally to the pure statistical uncertainty, a systematic uncertainty of

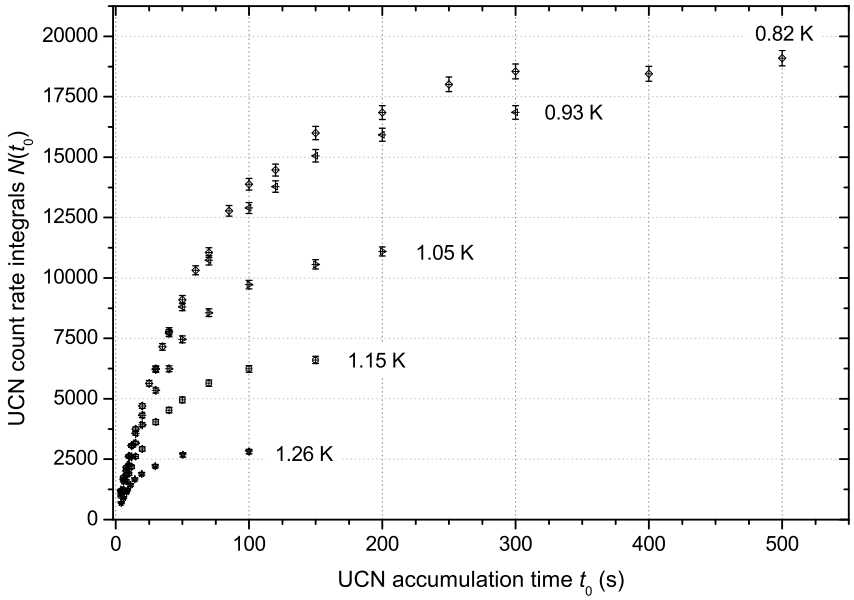

Figure 5.7: Total number of UCN after the accumulation for a time t_i, for different temperatures.

30 % of the counts in the first bin of each emptying histogram is included into the error bars of each data point. It takes into account the uncertainty in synchronisation of opening and closing the cold neutron and UCN shutter simultaneously. Assuming that the number of overcritical UCN count rate $\dot{A}$ is constant for all temperatures also

$$A = \dot{A}\tau_\mathrm{o},$$

is constant where τ_o is the storage lifetime of overcritical UCN. With $\dot{A}$, which is determined from the continuous measurements, it is possible to make a least–χ^2 fit of Eq.(5.4) to all five data sets. At $T = 1.26$ K it yields $N_\infty = 2714(54)$ and $\tau = 15.4(6)$ s for a reduced $\chi^2 = 1.24$. The values of N_∞, τ, and χ^2 for all temperatures are listed in Tab. 5.1. For lower temperatures the χ^2 gets increasingly worse. This indicates that the exponential of Eq.(5.4) has to be changed to include a term taking the transformation of the spectrum into account. Therefore the entire build-up can not be described any more by one sole time constant.

The emptying time constant τ_e is obtained with fits of $N_0 \exp(-t/\tau_\mathrm{e})$ to each emptying histogram of a build-up curve (Fig. 5.4). The reduced χ^2 is close to unity of each emptying curve. As in the case of τ, also τ_e is dependent on the irradiation time which becomes increasingly more pronounced for lower temperatures. This dependence is shown in Fig. 5.8 for all temperatures and

temperature [K]	τ [s]	N_∞	χ^2
0.82	68.6(9)	18143(135)	4.30
0.93	61.9(1.1)	16287(198)	3.15
1.05	43.7(8)	10826(124)	2.86
1.15	29.4(8)	4981(99)	2.34
1.26	15.4(6)	2714(54)	1.24

Table 5.1: Full data range: Results from least χ^2 fit of Eq.(5.4) to data shown in Fig. 5.7. The data point $N(4\text{s})$ is excluded from the fit as it was used to determine the offset A. This shared constant, $A = 13.4(19)$, describes overcritical UCN in the first moment after opening the UCN valve and is deduced from the continuous measurement.

temperature [K]	τ [s]	N_∞	χ^2
0.82	82.7(4.9)	18868(209)	0.98
0.93	70.8(2.9)	17008(252)	0.14
1.05	47.7(1.7)	11139(158)	0.89
1.15	33.6(1.7)	6552(121)	1.22
1.26	16.2(8)	2753(60)	1.67

Table 5.2: Reduced data range to demonstrate the change of time contants with time: Results from least χ^2 fit of Eq.(5.4) to the last six points of each data set shown in Fig. 5.7.

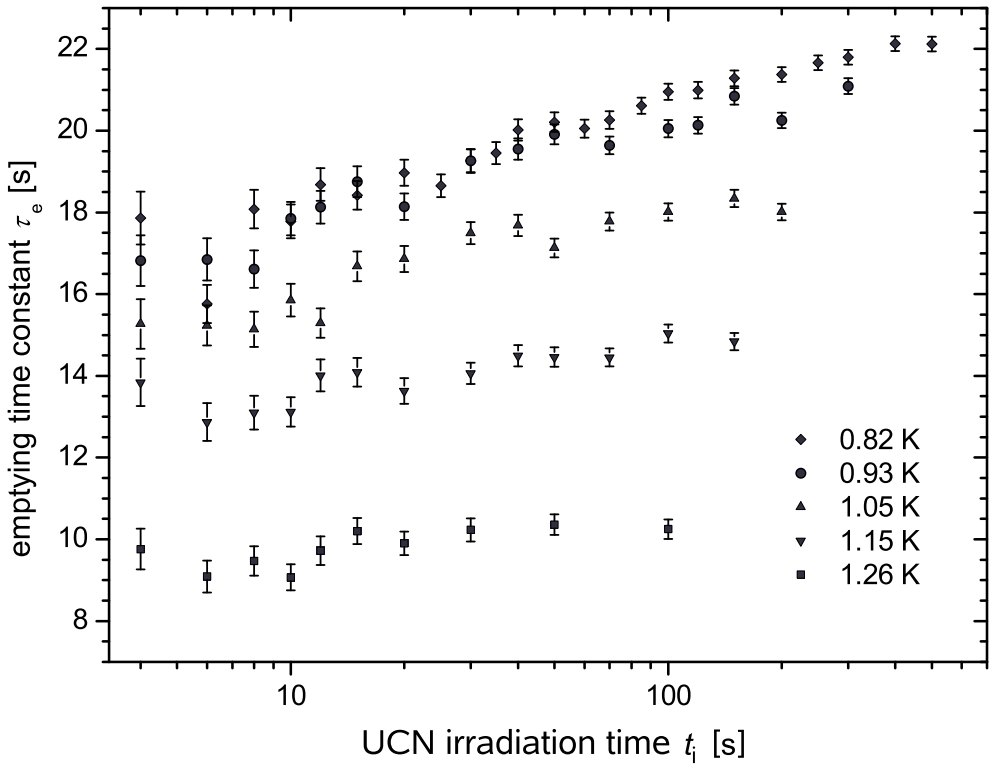

Figure 5.8: Emptying time parameter τ_e as a function of irradiation time t_i, determined from emptying histograms of all build-up mode measurements for various converter temperatures.

all t_i.

5.3.3 Change of lossrate with holding time

The dependence of the average UCN lossrate $(1/\tau)$ as a function of holding time t_h and irradiation time t_i can only be investigated in the storage mode. Although in general it is possible to fit a simple single-exponential decay to the data this gives a large reduced-χ^2. Moreover, just by looking at Fig. 5.6 it becomes evident that the loss rate decreases with storage time. This effect is expected, as neutrons with higher energy have a higher loss rate than those with small energies. This transforms the spectrum of stored neutrons with time, the mean energy and the average loss rate decrease.

5.3.4 Temperature dependence of the storage time

The storage time of UCN inside a superfluid helium is strongly dependent on the temperature. This effect was shown theoretical in Sec. 2.3.3. The temperature dependence can be written with Eqs(2.25,2.27,2.30) as:

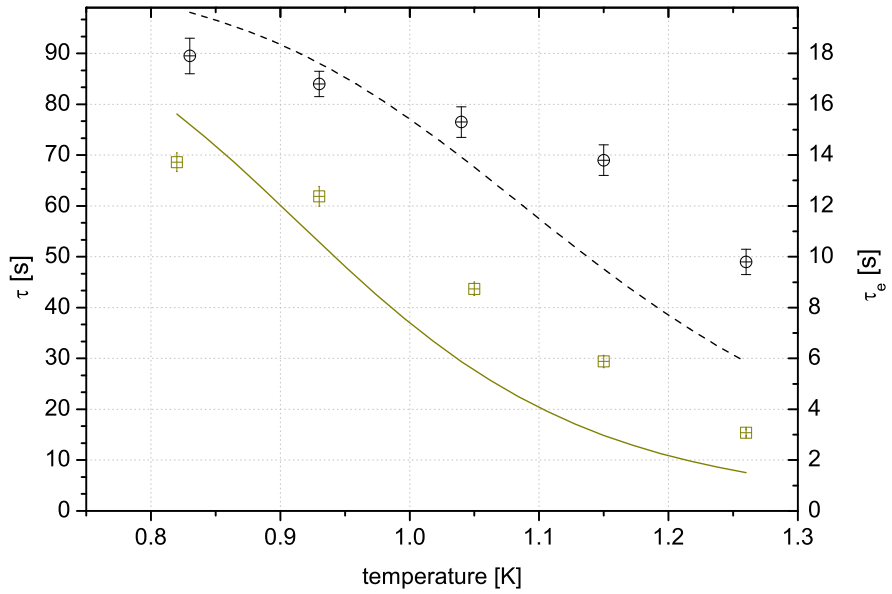

Figure 5.9: Dependence of storage time τ (⊞) and emptying time τ_e (⊕) on temperature T of the converter. Curve (—) and (- - -) are least-χ^2 fits of Eq.(5.5) to the data points.

$$\frac{1}{\tau(T,E)} = \frac{1}{\tau_\beta} + \frac{1}{\tau_l(E)} + \frac{1}{\tau_{1-\mathrm{ph}}(T)} + \frac{1}{\tau_{\mathrm{pp}}(T)} + \frac{1}{\tau_{\mathrm{rp}}(T)}. \tag{5.5}$$

In Fig. 5.9 comparisons with measured results are shown. A least-χ^2 fit of Eq.(5.5) to experimental data of $\tau(T,E)$ and $\tau_e(T,E)$, where $\tau_l(E)$ is the free parameter give extremely large reduced-χ^2s.

5.3.5 Production rate and extraction efficiency

The deduction of the production rate P from the continuous measurement count rate $\dot{N}_c = \dot{N} - \dot{A}$ (Fig. 5.5), where $\dot{N}$ is the measured value and $\dot{A}$ is a temperature-independent background, has to be done with caution. Although it is straightforward to give the formula for P:

$$P = \frac{\dot{N}_c}{VW}, \tag{5.6}$$

where V is the production volume and W the probability of an UCN to be detected; it is less evident how to correctly estimate $\dot{N}_c$ from $\dot{N}$ and W in

	$T = 1.26$ K	$T = 1.15$ K	$T = 1.04$ K	$T = 0.93$ K	$T = 0.82$ K
τ_e [s]	9.8(5)	13.8(6)	15.3(6)	16.8(5)	17.9(7)
τ_{ext} [s]	28.0(8)	26.0(10)	23.5(1.0)	23.1(1.2)	24.2(1.1)
$\dot{N}_c$	147(2)	202(2)	245(2)	263(2)	271(2)

Table 5.3: Time constants of the continuous measurement. The time constants τ_e were deduced from the $N(4\,s)$ - measurement in the build-up mode. $\dot{N}_c$ and the common parameter $\dot{A} = 13.4(1.9)$ s^{-1} are deduced from a least–χ^2 fit of Eq.(5.7) to data shown in Fig. 5.5, with fixed time constants τ_e and yiedling a reduced-$\chi^2 = 1.13$.

the continuous measurement. To determine $\dot{N}_c$ all five data sets are fitted simultaneously to the function (red curves in Fig. 5.5):

$$\dot{N}(t) = \begin{cases} \dot{N}_c + \dot{A} & : \quad t < t_i \\ \dot{N}_c \cdot e^{-\frac{t-(t_i+\Delta t_i)}{\tau_e}} & : \quad t \geq t_i \end{cases} \tag{5.7}$$

where t_i is the time after which the cold neutron shutter was closed by the program. The fit starts when the continuous count rate is in saturation. The delay time Δt_i is a common fit parameter for all five temperatures. This fit function defines overcritical neutrons as neutrons which have a rapid fall-off in count rate, with a time constant below the time resolution of the data acquisition. The decay can be described with a single parameter exponetial decay for all temperatures, as the neutrons are not stored and any spectral shaping should be negligible. For the fit τ_e is not a free parameter, but taken from the fits to the build-up emptying histograms at $t_i = 4$ s to minimise correlation with other fit parameters. It is assumed that the contribution from overcritical UCN, $\dot{A}$, to the equilibrium count rate is constant for all five data sets. It is therefore a shared parameter of all data sets in the least-χ^2 fits. In Tab. 5.3 the parameters are listed for the best fit with reduced-$\chi^2 = 1.13$.

The probability W can be given, as in Eq.(5.3) up to an unknown factor $0 < \epsilon \leq 1$ describing losses during extraction, by:

$$W = \epsilon \left(1 - \frac{\tau_e}{\tau}\right). \tag{5.8}$$

This equation is only vaild in the case where τ is time independent. This is only the case where up-scattering is the dominant loss factor. With $\dot{N}_c$ determined, and the time constants: $\tau = 15.4(6)$ s and $\tau_e = 9.8(5)$ s for fomblin at $T = 1.26$ K, we obtain:

$$\epsilon P_c = 0.68(8)\ \text{cm}^{-3}\text{s}^{-1}.$$

T [K]	ϵP_c [cm^{-3}s^{-1}] (continuous)	ϵP_b [cm^{-3}s^{-1}] (saturation)
0.82	0.62(1)	0.60(1)
0.93	0.61(1)	0.61(1)
1.05	0.63(2)	0.64(1)
1.15	0.64(3)	0.68(2)
1.26	0.68(8)	0.81(2)

Table 5.4: Production rates deduced with both methods. The noted error contains only statistical uncertainty. By far the largest uncertainty comes from neglecting the temporal evolution of the UCN spectrum.

Although this method has the advantage to be independent on the temporal evolution of the energy spectrum of the stored UCN it is very sensitive to a wrong estimation of the contribution from neutrons with $E > V_c$.

A second method to deduce the UCN production rate is based on the saturated integral UCN number N_∞ in the build-up mode. Here the fraction of overcritical UCN is smallest as overcritical UCN have much shorter time constants than stored UCN. When UCN are accumulated for $t_i \gg \tau$ the loss rate and production rate are in equilibrium. Denoting with N_0 the saturated number of UCN in the vessel (of which only a fraction $N_\infty = WN_0$ is detected) one can write:

$$P = \frac{N_\infty}{WV\tau} \tag{5.9}$$

The small fraction of overcritical UCN is estimated to be identical with $\dot{A}\tau_o = 13.4(19)$ from the shared least-χ^2 fit to the continuous measurement. Using the same values for the time constants at $T = 1.26$ K as in the former determination of P and $N_\infty = 2723(56)$, from Tab. 5.1, I obtain:

$$\epsilon P_B = 0.81(2) \text{ cm}^{-3}\text{s}^{-1}.$$

The values for the other temperatures are listed in Tab. 5.4. An average τ deduced from a fit to the entire range of the data sets will be smaller as in the equilibrium state for $t_i \to \infty$. This gives a too large loss rate for the actual equilibrium situation and therefore, combined with the saturated UCN number, values of the production rate which are too high. Without an exact understanding of the evolution of the spectrum with irradiation time it will be impossible to deduce an accurate number for the production rate.

5.3.6 Comparison with calculated UCN production rate

With the formula for UCN production in superfluid helium Sec. 2.3.2 and the measured cold neutron flux (see Fig. 5.3a) it is possible to calculate the expected production rate. The UCN production rate was calculated in Chapter 3.3 and is given by Eq.(3.2) (with values from Tab. 3.1):

$$P_{\mathrm{I}} = 4.97(38) \cdot 10^{-8} \ \frac{\text{Å}}{\mathrm{cm}} \mathrm{d}\Phi/\mathrm{d}\lambda|_{\lambda^*}. \tag{5.10}$$

For a fomblin coating, as in this experiment, the value of Eq.(5.10) has to be corrected for the wall potential of fomblin. The value has to be divided by the factor:

$$\left(\frac{V_{\mathrm{Be}} - V_{\mathrm{He}}}{V_{\mathrm{Fo}} - V_{\mathrm{He}}}\right)^{3/2} = \left(\frac{252 - 18.5}{115 - 18.5}\right)^{3/2} = 3.76(59),$$

with the uncertainty due to the poor knowledge of the wall potential of the used Fomblin grease. The differential flux was $\mathrm{d}\Phi/\mathrm{d}\lambda = 5 \cdot 10^7$ cm^{-2}s^{-1}Å^{-1} at $\lambda = 8.9$ Å. Together with the multiphonon contribution the expected value is:

$$P_{\mathrm{F}}^{\mathrm{theo}} = P_{\mathrm{I}}^{\mathrm{theo}} + P_{\mathrm{II}}^{\mathrm{theo}} = 0.66(11) + 0.62(9) = 1.28(14) \ \mathrm{cm}^{-3}\mathrm{s}^{-1}, \tag{5.11}$$

calculated with the measured incident spectrum (Fig. 5.3a) and the formula Eqs (2.23,3.4,3.2) for multiphonon and single-phonon production rate.

Both analyses of ϵP give only slightly different results (see Tab. 5.4). A τ, derived from the build-up measurement with the complete set of data, overestimates in general the production rate. The derivation from continuous measurements at low temperatures is difficult as the evolution of the spectrum during the extraction is unknown ($t_{\mathrm{ext}} \approx 23$ s). Therefore the most reliable estimation is at high temperature, for an utmost unchanged UCN spectrum. This assumption can only be made for the continuous measurement at $T = 1.26$ K:

$$\epsilon P = 0.68 \pm 0.08_{\mathrm{stat}} \pm 0.07_{\mathrm{sys}}. \tag{5.12}$$

where the systematic error is estimated by variing the data range for the determinatin of τ. Using only the first six data points of the build-up curve gives a τ which is 18% smaller than using the last six points.

This gives an $\epsilon = 0.53(12)$ which still has to be multiplied with $(\tau - \tau_e)/\tau \leq 0.784$, in the most optimistic estimation, to give the overall extraction efficiency $W \approx 41$ %.

5.4 Comparison with stainless steel converter vessel

The results from the above described measurements give interesting insights into the storage and the extraction of UCN especially when compared with the previous measurement where we have used an electropolished stainless steel converter volume [Zim07]. With the Fomblin grease coated volume the count rates of accumulated UCN observed immediately after opening the UCN valve and also the integral count rate were almost a factor three higher, despite a much lower critical wall potential. This absolute increase in UCN count rate can be explained by the considerably larger storage lifetimes τ, but also by the apparently shorter time constants for extraction τ_{ext}. Values for τ_{ext} from the measurements can be compared to the ideal situation of the gas-kinetic equation for a hole with surface area S:

$$\tau_{\text{ext}}^{\text{g}} = \frac{4V}{S\bar{v}},$$

where $V \approx 2.4$ litre is the volume of the used converter vessel and $\bar{v} = \frac{3}{4}v_c$ with v_c the critical velocity of the wall material. For the used converter volume with an extraction hole of $S = 200$ mm^2 we expect $\tau_{\text{ext}}^{\text{g}} = 14.8$ s, $\tau_{\text{ext}}^{\text{g}} = 11.3$ s for Fomblin, stainless steel respectively. The measured values are $\tau_{\text{ext}} = 25(2)$ s and $\tau_{\text{ext}} = 58(13)$ s. There are three possible explanations, which probably all contribute to the observed effect:

1. Polished surfaces increase the likelihood of closed trajectories of the UCN. The ensemble does not explore quickly enough the entire available phase space – one can not speak of an ideal gas. This hypothesis was already raised earlier by W. Mampe and colleagues for their liquid-wall bottle lifetime experiment [Mam89].

2. The flapper UCN valve hinders the direct transmission of UCN through the exit from a large part of the phase space. If the UCN ensemble is considered as an ideal gas this will not play a role. Otherwise the likelihood for an UCN to pass through the hole will decrease with the non-ideal gas character.

3. The high-energy part of the spectrum is rapidly lost from the storage volume. This leads to $\bar{v} < \frac{3}{4}v_c$ and the value for $\tau_{\text{ext}}^{\text{g}}$ increases accordingly.

For the design of a future UCN conversion vessel this should be take into account in form of a certain roughness to facilitate a rapid exploration of the entire phase space and a design of a flapper valve which facilitates the passage through the exit in open position.

5.5 Discussion

In two experiments, one of them discussed here, UCN have been produced and stored in He-II. It was shown that a large fraction, approximatively 40 % can be extracted to a vacuum at room temperature. Measurements at different temperatures allow to analyse the effect of up-scattering on the storage life time. The experimental results agree poorly with the in Sec. 2.3.3 discussed theoretical predictions. This can be explained with the neglect of temporal effects on the UCN spectrum while storage in the analysis. These effects also lead to a high degree of ambiguity in the determination of the production rate. Although the analysis is done for a temperature where the effects should be smallest, τ descriping the storage time changes by ~ 20 % during build up. For lower temperatures this change increases even further (~ 50 % at 0.83 K). The discrepancy of expected extraction time τ^g_{ext} and measured τ_{ext} indicate that the extraction can further be optimised. Using highly specular UCN guides together with rough surfaces inside the source will allow to approach the theoretical value.

These results show that a dedicated experiment for the determination of the UCN production rate in He-II at SVP with an accuracy of the calculated values should be envisaged. Such an experiment should probably abandon the idea of storage of UCN. Instead it should be based on the direct detection of UCN after production. This could be done with a pulsed beam to minimise beam dependent background and detectors submerged into the liquid to avoid extraction dependent effects. The superfluid helium vessel should be coated with a good neutron absorber thus that UCN that do not directly reach the detectors are not stored.

Chapter 6

UCN Production in Helium Under Pressure

The aim of the experiment is the direct verification of the pressure dependence of the UCN production rate in He-II, derived and calculated in Chapter 3. This is done by a wavelength-resolved measurement of the UCN production rate for different pressures. This experiment was performed at the neutron user facility for particle physics, PF1b [Abe06] of the Insitut Laue Langevin. In the first section of this chapter the setup and the measurements are described. In the last section the data is analysed and the results are discussed.

6.1 Experimental method and setup

The wavelength-resolved measurement of the conversion rate of cold neutrons to ultra cold neutrons in superfluid helium (He-II) under pressure requires from the neutronic point of view a beam with an intense flux in the entire region were single and multiphonon processes can occur ($\lambda = 3\,\text{Å} - 10\,\text{Å}$). A device to select specific wavelength is indispensable to see changes of the position of the single phonon peak, but also to characterise the wavelength dependency of UCN production with pressure. To control the selected wavelength some sort of cold neutron wavelength analysis has to be set up. To minimise wavelength dependent systematic effects, the beam which passes through the helium has to have a divergence small enough to exit the production volume without thouching the sidewalls at the far side of the volume for all selected wavelengths. The converter has to be kept at the lowest stable temperature, where the conversion process takes place and the losses due to up-scattering are small compared to temperature independent losses. It has to be maintained inside a vessel which can resist the high pressures applied. A high Fermi potential is favourable to increase statistics, whereas the loss

rate per wall collision η of the material can be of the order of $\sim 1 \cdot 10^{-4}$ as the storage time is limited by the permanent extraction. The use of an UCN valve, as in the experiment in Garching (see Chapter 5), is not necessary and would have complicated the setup. A thin material window, resisting up to 30 bar, is required to separate the extraction vacuum from the pressurised converter. Last but not least this requires a cryostat which is coupled to the converter providing cooling power as well as a method to apply pressure.

6.1.1 Overview of the setup

The cold to ultracold neutron conversion rate (short: UCN production rate) is measured in dependence of the incident cold neutron wavelength for 3.5 Å$\leq \lambda <$ 9.5 Å and pressures $p =$ SVP, 3, 6, 11, 16 bar, and 20 bar of the superfluid helium. A sketch of the experimental setup is shown in Fig. 6.1.

In a first reference measurement at SVP the differential UCN production rate $\mathrm{d}P/\mathrm{d}\lambda$ is measured. Then this is repeated for higher pressures. The observational parameter for each individual measurement is the detection rate of neutrons in the detector in dependence on pressure, temperature, incident wavelength, and incident flux which is a function of the selected wavelength.

To select a desired incident wavelength the cold neutrons pass through a turbine neutron velocity selector [Wag92] inside the casemate of PF1b. Thereafter they are guided to the entrance of the cryostat in a pure nickel guide with a rectangular cross section of 30×50 mm^2. An aperture of $\varnothing = 30$ mm from B_4C reduces the beam cross section. A monitor detector after the cold neutron shutter in front of the entrance window of the cryostat is recording the incident flux. Inside the conversion volume, filled with purified superfluid helium, a fraction of the cold neutrons will be downscattered to the ultracold neutron range. The UCN then have to pass through a thin aluminium window before they are guided to the detector in polished stainless steel tubes. A part of the cold neutrons traversing the helium will be scattered to energies above the wall potential of the conversion vessel. With a high propability they will be lost from the conversion volume and the UCN guides. The main part of the incident neutrons will pass the apparatus without any interaction. A chopper behind the exit window of the cryostat allows to measure the time-of-flight spectrum with a detector placed 2 m further downstream.

6.1.2 PF1b – an intense source of cold neutrons

The instrument PF1b has a capture flux of $\Phi_c \approx 2 \cdot 10^{10}$ cm^{-1}s^{-1} [Sol08], with a spectrum well suited for our measurement (see Fig. 5.3b).

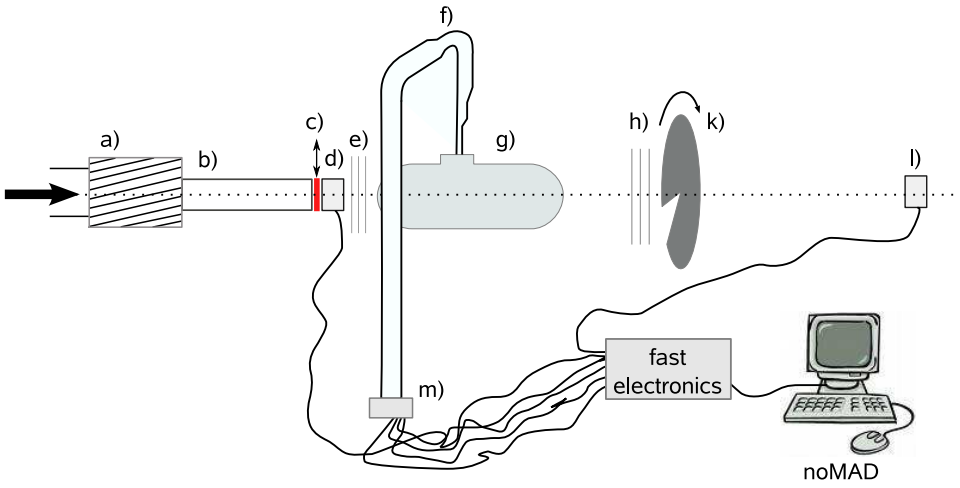

Figure 6.1: Sketch of the experimental setup. The polychromatic cold neutron beam is incident from the left on the velocity selector (a). A secondary natural nickel guide (b) transports the now nearly monochromatic neutrons to the apparatus. The neutrons pass a shutter of boron plastic (c), the flux monitor (d) with a circular aperture of $\varnothing = 30$ mm, and three aluminium foils before they enter the conversion volume made of nickel (g). UCN that are produced inside the volume can exit through the extraction system (f) and are counted by the UCN detector (m). The main fraction of cold neutrons pass the volume unhindered and exit the apparatus through three aluminium windows (h). After passing an exit aperture of $30 \times 50\text{mm}^2$ and a chopper (k) with slit width 3 mm the actual wavelength can be determined with the time-of-flight to the "TOF"-detector (l). The signals of all three detectors are preamplified and then registered with NoMAD, which also controls the shutter and the speed of the velocity selector.

The initial neutron source is the 58 MW research reactor of the Institut Laue Langevin with its vertical cold source [Age89], filled with 20 dm^2 liquid deuterium for thermalization of the neutrons to an almost Maxwellian spectrum at 25 K. A part of these cold neutrons is extracted horizontally into the ballistic supermirror guide H113 feeding our experiment. Further discussion of the properties of the guide and a detailed measurement of the wavelength spectrum is given in Ref. [Abe06]. The capture flux spectrum $d\Phi_c/d\lambda$ at the exit window of the guide can be parametrised by Eq.(11) in Ref. [Abe06]:

$$\Phi_c = \Phi_0 \frac{(\lambda/\lambda_2)^p}{1+(\lambda/\lambda_2)^p} e^{-\lambda/\lambda_1}, \tag{6.1}$$

which is shown in Fig. 5.3b for the values $\Phi_0 = 1.3 \cdot 10^{10} cm^{-2} s^{-1} Å^{-1}$, $\lambda_1 = 3.3$ Å, $\lambda_2 = 4.0$ Å, and $p = 3.0$. The flux has changed since, as some guide segments and the in-pile part of the guide were replaced. The divergence at the exit of the neutron guide is of importance for the transmission of the neutron velocity selector. In [Abe06] the angular distribution is discussed extensively and it is shown that the horizontal and vertical divergence can be approximated by a Gaussian function with a width of $\eta(\text{FWHM}) = 7$ mrad $= 0.4°$ for the polychromatic beam. The cut-off angle $\gamma = \kappa \cdot \lambda$ for a given wavelength, with the "mirror constant" $\kappa = 1.7$ mrad/Å, describes the wavelength-dependent divergence. These values might have changed slightly with the changes of the guide.

6.1.3 The neutron velocity selector

The measurement of the wavelength differential UCN production rate requires a selection of the incident wavelength. In general two different methods are used to select a monochromatic beam from a broad neutron energy spectrum. Either a crystal monochromator is reflecting neutrons under the Bragg condition off the beam axis, or in the case of a velocity selector a velocity condition is imposed on the entire beam. The use of a Bragg reflexion from a crystal can provide a very narrow incident energy spectrum. There are two types of crystals, MICA and graphite intercalated compounds, with a lattice spacing large enough to cover the wavelength range of interest. But, using a crystal as monochromator would have either meant to rotate the entire experimental setup around the axis of the crystal, or to use a device with two crystals in a "Z"–configuration. The first solution is impossible from the room available in the experimental zone of PF1b as well as the peculiarities of the experimental setup, the second from lack of such a device. Fortunately, our measurement requires only a moderate wavelength resolution, as the spectrum that is measured has only one significant peak. This allowed us to use a selector turbine for the measurements which covers, with

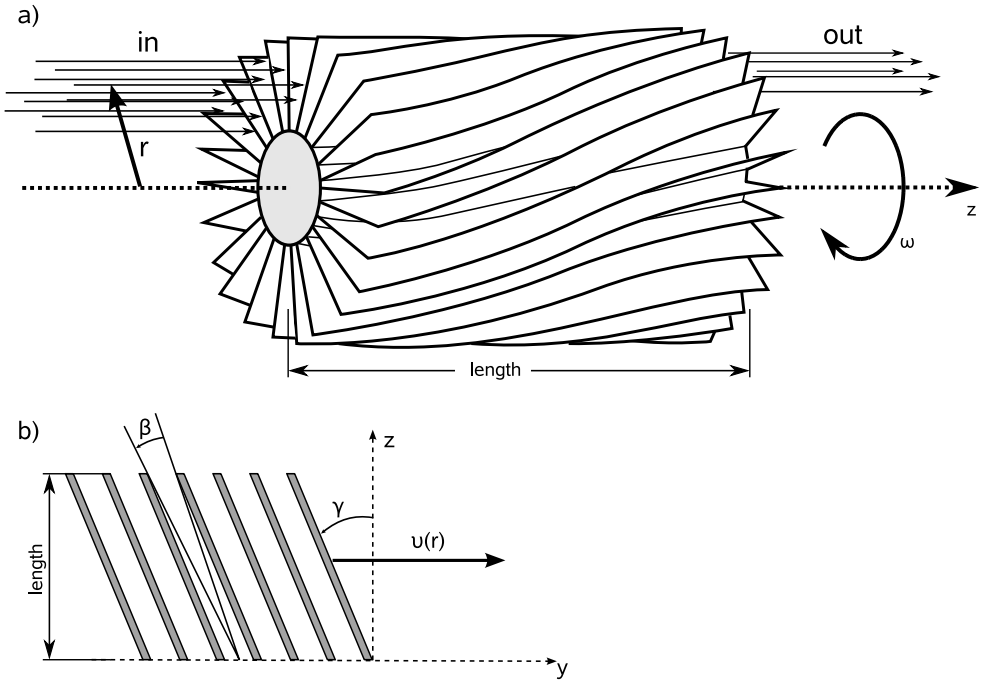

Figure 6.2: (a) Sketch of neutron velocity selector with helical lamellae. (b) At radius r the selector can be described by a Soller collimator inclined by the angle γ moving with the velocity $\nu(r)$ perpendicular to the flight axis-z, β indicates the geometrical acceptance of the collimator.

some changes, the entire wavelength range of interest. Furthemore it does not change the axis of the beam.

The selector used for the experiment is described in detail in Refs. [Fri89, Wag92]. It is made of helical lamellae coated with Gadolinium and spinning at a frequency $f \leq 28300$ rpm. These lamellae act as tilted Soller collimator which moves with a velocity $\nu(r) = \omega r$, where $\omega = 2\pi f$, perpendicular to the rotor axis.

The velocity distribution of the transmitted neutrons is:

$$\phi_{\mathrm{t}}(\boldsymbol{v}) = A(\boldsymbol{v})\phi(\boldsymbol{v}), \tag{6.2}$$

where $\phi(\boldsymbol{v})$ is the incident velocity-space density distribution and $A(\boldsymbol{v})$ is the opening function of the selector. Integrating over the perpendicular component gives the transmission for one neutron velocity $v_{\parallel}$:

$$T(v_{\parallel}) = \frac{\int A(\boldsymbol{v})\phi(\boldsymbol{v})\mathrm{d}v_{\perp}}{\int \phi(\boldsymbol{v})\mathrm{d}v_{\perp}}, \tag{6.3}$$

which explicitly depends on the form of $\phi(\boldsymbol{v})$. The transmitted mean velocity is given by:

γ' [°]	λ-range [Å]	calculated $\Delta\lambda$(FWHM)/λ [%]
+ 5	$5.5 - 10$	~ 8
0	$4.5 - 9$	~ 10
- 5	$3.5 - 8$	~ 14

Table 6.1: Calculated wavelength ranges and resolutions accessible with rotation speeds between 15600 rpm and 28300 rpm. The incident divergence is taken to be $\alpha = 0.4°$.

$$\bar{v_{\parallel}} = \omega \bar{r} \tan(\gamma), \tag{6.4}$$

where $\bar{r}$ is the mean distance of the passing neutron to the rotation axis and γ the inclination of the lamellae with respect to the flight axis (see Fig. 6.2). The velocity $\bar{v}$ for a given rotation frequency can be changed by tilting the selector axis by the angle γ' with respect to the beam axis, thus $\gamma = \gamma_0 + \gamma'$, with γ_0 the fixed angle between lamellae and selector axis. Thus the whole velocity range of the selector can be shifted. In this case the resolution $\Delta v/\bar{v}$, which can be approximated for a Gaussian-like divergence by:

$$\Delta v/\bar{v} = \frac{\tan\gamma}{\sqrt{\alpha^2 + \beta^2}}, \tag{6.5}$$

where α is the divergence of the incident neutron beam and β defined in the Fig. 6.2, will also change (see Tab. 6.1).

Characteristics of the selector

The rotation speed of the Dornier Neutron Velocity Selector can be varied between 3000 and 28300 rpm. It is mounted on a rotational table which allows to change the angle γ' between beam and rotation axis. The whole apparatus is mounted on a concrete block inside the casemate of H113 just in front of the experimental area of PF1b. Vibrations of the setup can occur depending on the rotation frequency. All vibrations greater than 0.4 mm/s^2 in radial directions can cause permanent damage to the selector and have to be avoided in measurements. In a test two critical ranges of speeds, between 5000 rpm and 10000 rpm and between 12800pm and 15600 rpm, have been identified. Speeds in this range were not accessible in the entire experiment. This forced us to measure with inclined rotation axis at $\gamma' = 5°, -5°$ to cover the interesting wavelength range of $\lambda = 3.5$ Å–10 Å. In Tab. 6.1 the corresponding wavelength ranges are listed, for both angular settings. The values for the resolution have been calculated for the ideal case of a perpendicularly moving Soller collimator inclined by $\gamma = 0.32$ rad, with $\beta = 33.5$ mrad [Fri89], and $\alpha = 7$ mrad [Abe06] using Eq.(6.5). It should be

noted that the scale of γ' could have an offset, i.e. the inclination between beam and selector at "$\gamma_0 = 0$" was not necessarily 0. Only differences to the position "$\gamma_0 = 0$" were measured.

6.1.4 Conversion volume

The volume filled with superfluid helium in which the conversion of cold neutrons to UCN takes part is made from 3 mm thick aluminium and 1 mm thick stainless steel. The sketch in Fig. 6.3 is also showing the inner wall made from nickel coated stainless steel and 0.2 mm thick nickel sheets. According to French security legislation for pressure recipients the vessel did not exceed a volume of 1 litre, making a certification by an independent body superfluous. It was tested with pressures up to 50 bar in several overnight experiments. The radial dilatation which was measured to be 50 μm for 50 bar was completely elastic for all test runs. This indicates that there will be no long-term fatigue of the material.

The design was made according to legislation and so that the entrance window for cold neutrons is as close a possible to the entrance flange of the cryostat. The UCN exit window, made from 100 μm aluminium, required a support structure (see Fig. 6.3) from stainless steel with an effective hole surface of 126.8 mm^2.

Superfluid helium was entering through the long horizontal aluminium tube which is connected via an "U"-shaped copper pipe to the ^{3}He evaporation stage of the cryostat described in Sec. 4. A calibrated Cernox[1] heat sensor, with a typical accuracy of $\pm$5 mK and a longterm stability of $\pm$25 mk at 1.4 K (tmperature range: 0.5 K – 325 K), is screwed to the outer wall of the conversion volume. A long vertical capillary, heat anchored to the 4 K and 70 K screen, is used to evacuate the volume prior to cooldown and to measure the pressure inside the converter volume during the experiment. The pressure is applied through the superleak from a commercial 50 litre, 200 bar gas cylinder.

6.1.5 UCN extraction line

The UCN extraction line is identical to the one described in Ref. [Zim07] and in Sec. 5. It is heat anchored to the 4 K screen after the initial 70 mm made from a tube with wall thickness 0.4 mm for reduced heat conductivity. A second heat anchor to the 70 K outer screen is fixed to the horizontal section after the first bend. In this setup the UCN have to go up $\sim$ 0.2 m before they fall down in an $\sim$ 1.5 m long vertical tube to the UCN detector,

[1]Model: CX-1030-CU, Lake Shore Cryogenic, Inc, www.lakeshore.com

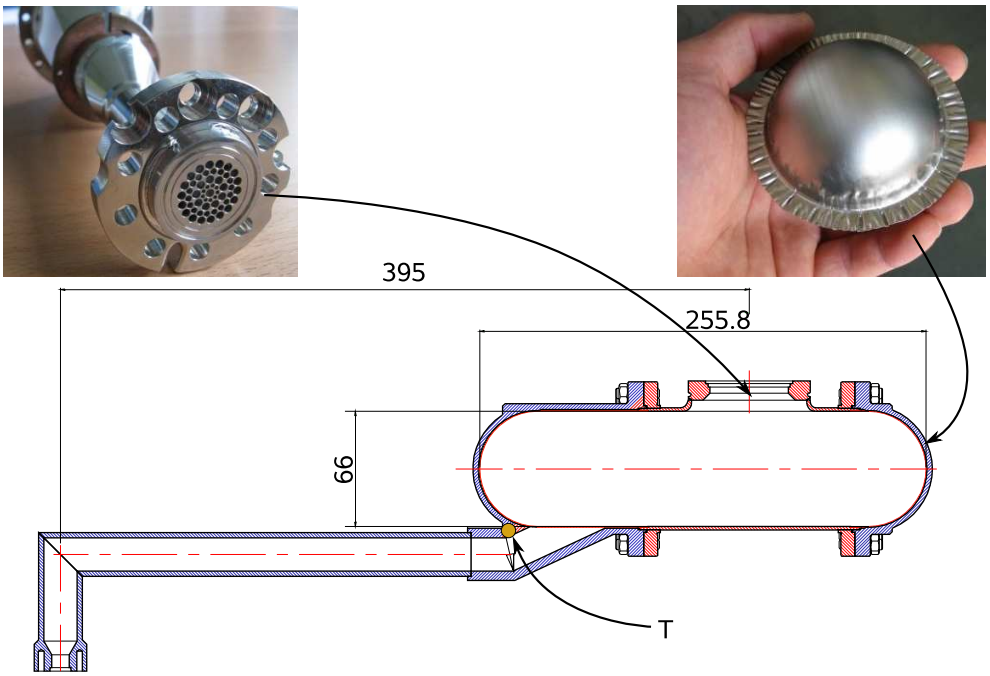

Figure 6.3: Sketch and photographs of the the conversion vessel. Aluminium was used for the outer vessel to withstand high pressure at low activation by the cold neutron beam. The conversion volume itself was defined by two end caps from 0.2 mm nickel sheet (photography top right) and the nickel coating of the central stainless steel piece (red in the drawing). The support structure (photography top left) for the UCN exit window is made of stainless steel. The calibrated heat sensor was screwed to the aluminium housing at (T).

which can be separated by a vacuum-tight UCN shutter from the rest of the extraction vacuum. The typical vacuum pressure inside the extraction line was $p_{\text{extr}} \approx 10^{-5}$ mbar and $p_{\text{extr}} \approx 10^{-6}$ mbar with the production volume at room temperature and cooled, respectively. This improvement with decreasing temperature indicates that gas is freezing out on the inside of the cold extraction tubes.

6.1.6 Time-of-Flight setup

Behind the exit window of the cryostat a time-of-flight measurement is set up to determine the exact wavelength spectrum of the cold neutrons which have passed the conversion volume for each velocity selector setting. The chopper (see Fig. 6.4) is a disc with $\varnothing = 25$ cm made from Li-rubber and Gd painted plastic/composite material. Four diametric rectangular slits of $w = 3$ mm pass behind a window of the same dimensions. The opening function can be approximated by a triangular in time, with the base width:

$$\Delta t = \frac{2w}{\Omega r}, \tag{6.6}$$

where Ω is the angular rotation frequency of the disc. The graph in Fig. 6.4 shows the deviation for rectangular slits. Each time a bunch of neutrons is passing, the chopper sends a start signal to the data acquisition. At a distance of 200(1) cm a neutron detector with a thickness of 44(1) mm is placed to register the time-of-flight. As the detector has a low efficiency ($\sim 5 \cdot 10^{-5}$), the detection efficiency is constant over the thickness of the detector.

6.1.7 Neutron detector and monitors

At three different points (see Fig. 6.1) neutron detectors are used to either monitor the cold neutron flux, count the number of UCN which have passed the extraction tubing, or detect the cold neutrons of the time-of-flight measurement. Monitors are detectors which only detect a small fraction of the neutrons passing and typically have a detection efficiency proportional to $1/v$ (v is the neutron velocity). These monitors are used in front of the entrance window of the cryostat and also as time-of-flight detector. The detector for UCN is placed at the end of the UCN extraction line, ~ 1.5 m below the horizontal section. This vertical acceleration section increases E_{kin} of the UCN by $\Delta E_{\text{kin}} \approx 150$ neV and increases the transmission through the aluminium entrance window of the detector.

Cold and ultracold neutrons can only be detected through nuclear reactions.

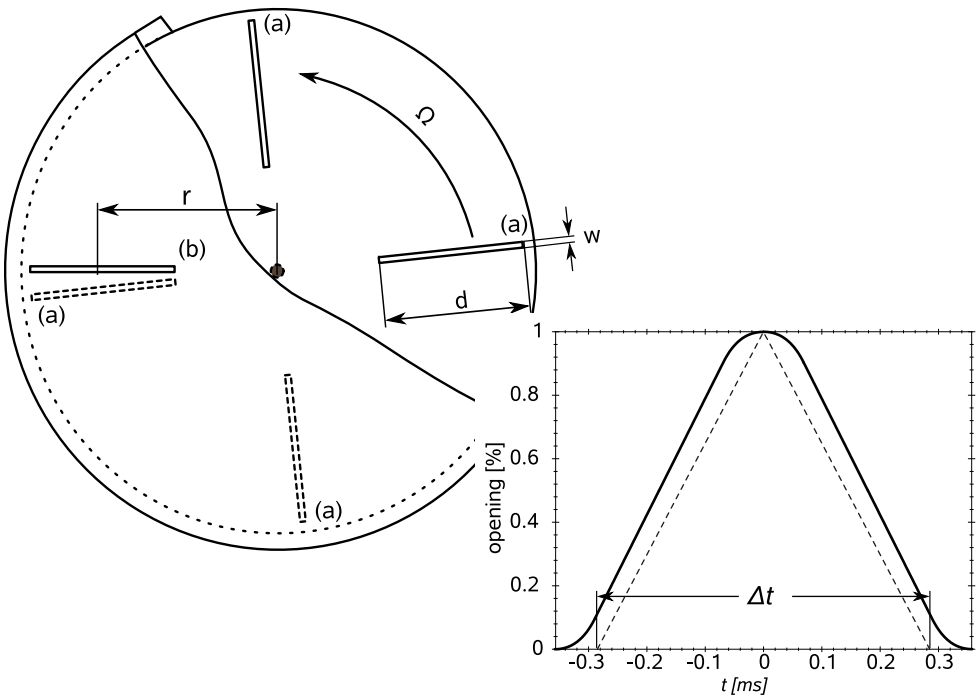

Figure 6.4: Sketch of time-of-flight chopper. The disc with four slits (a), rotates with a rotation frequency Ω inside a housing with a small window (b) of the same dimensions as the slits. The graph shows the opening function for the case of radial openings (- - -) and rectangular openings (—).

Charged particles or gammas from these reactions can then be detected by their electromagnetic interaction. Three typical reactions are used for neutron detectors:

$$^{3}\mathrm{He} + \mathrm{n} \longrightarrow \quad p + t + 780 \text{ keV} \qquad 5333(7)\text{barn} \qquad (6.7)$$

$$^{6}\mathrm{Li} + \mathrm{n} \longrightarrow \quad t + \alpha + 4.78 \text{ MeV} \qquad 940(4)\text{barn} \qquad (6.8)$$

$$^{10}\mathrm{B} + \mathrm{n} \longrightarrow \begin{array}{ll} ^{7}\mathrm{Li} + \alpha + 2.79 \text{ MeV} & 6.4\% \\ ^{7}\mathrm{Li}^{*} + \alpha + 2.31 \text{ MeV} & 93.6\% \end{array} \qquad 3835(9)\text{barn} \qquad (6.9)$$

The UCN and ToF detector use both ^{3}He as converter, only the beam monitor is a ^{6}Li–detector.

UCN detector

The UCN detector was designed and constructed by the Frank Laboratory of Neutron Physics in Dubna. It is a ^{3}He-counter with a 100 μm thick entrance window made of aluminium, which has a critical energy of 54 neV. The detection volume is filled with 18 mbar ^{3}He for neutron absorption, 12 mbar CO_2 and 1070 mbar Argon. The low helium pressure make it practically

insensitive to cold and thermal neutrons. For UCN the attenuation length is in the range of 10 mm. A wire electrode with +1000 V on the bottom of the cylindrical gas volume collects the charges. The signal is preamplified by an integrated preamplifier. Shielding is done using borated polyethylene bricks on the outside and borated rubber for the inner most layer. A typical pulse height spectrum is shown in Fig. 6.5 a.

Flux monitor and time-of-flight detector

The cylindrical flux monitor is coated on the inside with ^{6}LiF and has a detection efficiency of $\sim 2.6 \cdot 10^{-6}$. If a neutron is captured by ^{6}Li either the charged tritium or the alpha will ionise the counting gas. A wire electrode at 1100 V in the centre of the cylinder is collecting the charges. The preamplified signal was discriminated with a threshold of 0.75 V, the dead time is 2.2 μs. The pulse height spectrum is shown in Fig. 6.5 b.

The time-of-flight detector is a ^{3}He counter with a detection efficiency of $\sim 5 \cdot 10^{-5}$. An anode at 1500 V in the centre of an aluminium cuboid is collecting the charges. The threshold for discrimination is set to 0.997 V, shown on Fig. 6.5 c. The dead time of this detector is 4 μs.

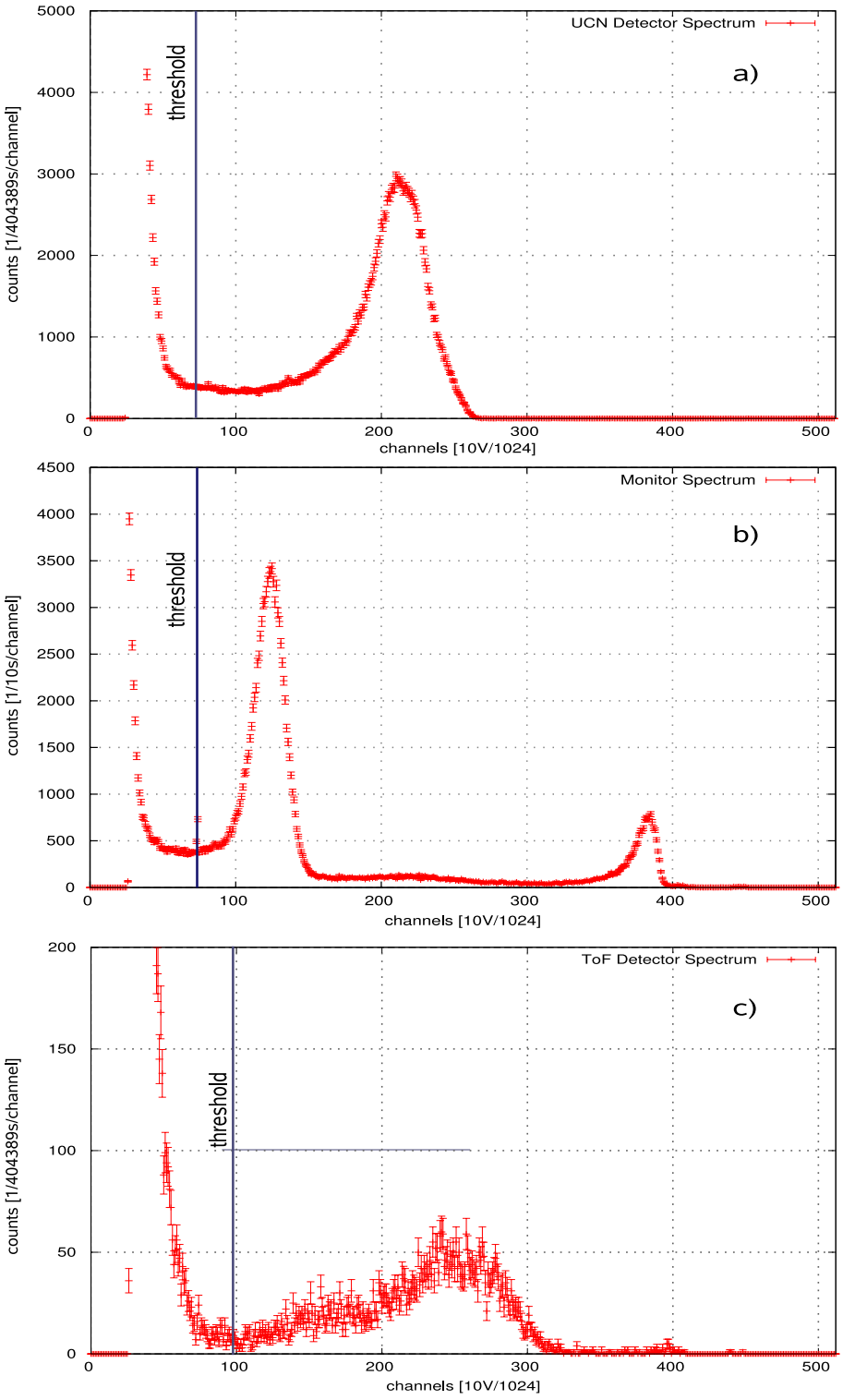

Figure 6.5: Pulse height spectra of a) UCN detector, b) flux monitor, and c) time-of-flight detector. The vertical lines indicate the threshold above which all events are counted.

6.2 Measurement

The cryostat was cooled down three days prior to the start of the third reactor cycle, which started 27$^{\text{th}}$ August 2008. At 2 pm, 26$^{\text{th}}$ August 2008 the superleak opens at a temperature of $T_{\text{He}-4} = 2.04$ K. The following 24 hours we fill the volume via the superleak with purified ^{4}He. After several unsuccessful tries to take the ^{3}He circuit with its 0.5 K evaporation stage into operation we decide to replace ^{3}He with ^{4}He from another gas cylinder. In the evening of the 28$^{\text{th}}$ we reach $T_{\text{vol}} = 1.15$ K (temperature of the converter vessel). For the following 12 days we have taken data at $p_{\text{vol}} = \text{SVP}, 3, 6, 11, 16, 20$ bar with this setup. Also trials with solid-He were made, which are not discussed within this thesis.

6.2.1 Beam profile measurements

After the neutrons have passed the velocity selector they are guided for 2 m inside a pure nickel guide to the experimental zone. Beam profile measurements with a CCD-beam camera have been made prior to the installation. The divergence itself has no influence on the UCN production rate. Nevertheless it is important to check, whether for all selected wavelengths the beam passes completely inside the conversion vessel. This was done for maximum (28300 rpm) and minimum (15600 rpm) selector velocity at an angular setting of $\gamma' = +5°$ and at three different positions indicated in Fig. 6.6. The divergence $\alpha(15600\,\text{rpm}) = 17$ mrad for the largest wavelength ($\sim$ 9.8 Å) used in experiment. Typically it decreases for shorter wavelength. For a selector speed of 28300 rpm with same angular settings we found $\alpha(28300\,\text{rpm}) = 13$ mrad. This gives a maximum beam width $\varnothing_{\text{w}} \leq 47$ mm at the exit of the converter vessel ($\varnothing = 66$ mm).

Furthermore, a beam profile measurement at the exit of the monitor (shown in Fig. 6.7) was made to see eventual inhomogeneities in the spatial neutron distribution. The beam profile of the longer wavelength shows that the region of highest intensity is non-centred, but instead shifted to the upper left corner of the image. The one for the short wavelengths (28300 rpm) has a lower degree of inhomogeneity although the region with highest intensity is also off-centre.

6.2.2 Gold foil activation

Two gold foil activation measurements directly at the exit of the cold neutron flux monitor have been performed for selector speeds of 15600 rpm and 28300 rpm at an angular setting of the velocity selector of $\gamma' = +5°$. These allow to calibrate the detection efficiency of the monitor detector. The results

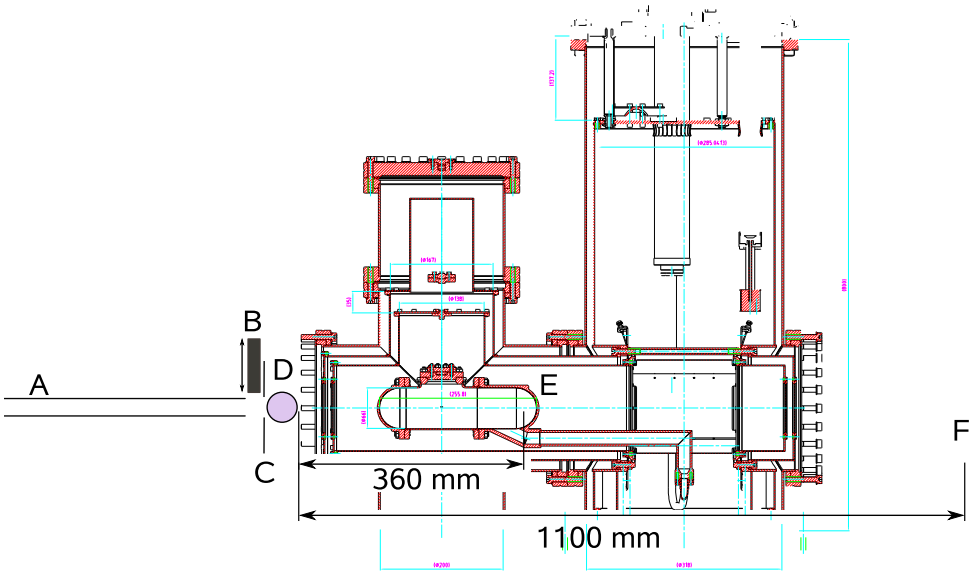

Figure 6.6: Sketch of beam profile measurement. The neutrons enter through the nickel guide (A), pass the open borated shutter (B),the beam is reduced by an aperture (C) to $\varnothing = 30$ mm. Right after the beam monitor (D) is the first position for a beam profile measurement, then there is one at (E) and (F) 360 mm, 1100 mm downstream from the monitor, respectively. The cryostat was not there at the time of measurement, it is only shown to visualise the three positions.

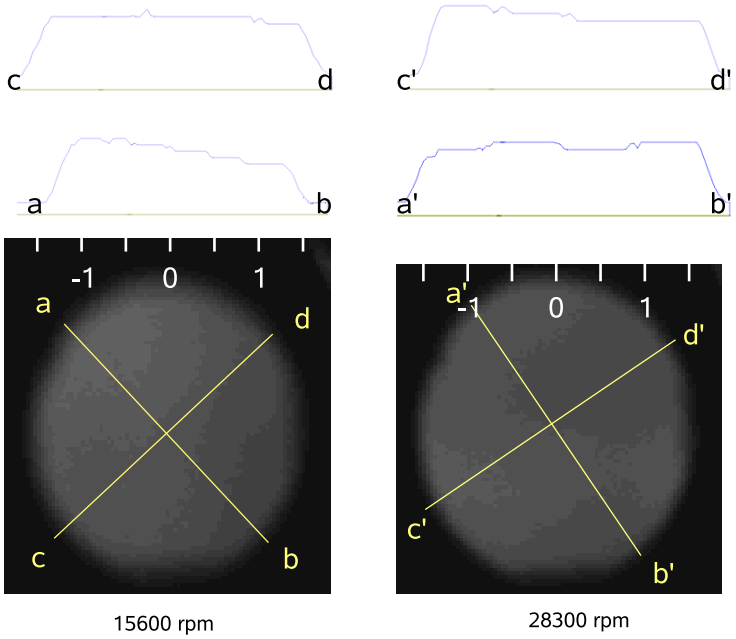

Figure 6.7: Beam profile measurements (Scale in cm) at the exit of the beam monitor for velocity selector speeds $f = 15600$ rpm and 28300 rpm. The brighter the shading the higher the neutron countrate.

rotation speed [rpm]	gold foil [$\mathrm{cm}^{-2}\mathrm{s}^{-1}$]	flux monitor [s^{-1}]	ratio
15600	$2.66 \cdot 10^8$	$10.586(17) \cdot 10^3$	$3.98 \cdot 10^{-5}$
28300	$4.91 \cdot 10^8$	$18.309(21) \cdot 10^3$	$3.72 \cdot 10^{-5}$

Table 6.2: Comparison of neutron fluxes from gold foil activation and the corresponding monitor values, corrected for a deadtime of 2.2 μs.

together with the monitor count rates are listed in Tab. 6.2.2.

The slight change in detection efficiency is probably due to wavelength-dependent, inhomogeneous distributions of neutrons across the monitor which has a circular opening of 30 mm diameter (discussed in the previous section). The gold foil, also circular has a diameter of 10 mm and covers therefore only $1/9^{\mathrm{th}}$ of the area in the centre. The monitor is to a good approximation an ideal $1/v$-detector. From the beam profile measurements it appears that the measurement at $f = 15600$ rpm overestimates, or the one at $f = 28300$ rpm underestimates, the efficiency of the detector. However, Fig 6.7 shows that the intensity distribution depends on the wavelength. As the monitor covers the entire area of the beam, we use the monitor data and not the gold foil results in the analysis.

6.2.3 Time-of-flight measurement

For each rotation speed of the velocity selector, and for both angles γ' $(-5°, 5°)$, a time-of-flight measurement was performed. The precise form of the time-of-flight spectrum at each individual rotation speed will be essential for the analysis of the wavelength-resolved conversion rates. In Fig. 6.8 a selection of typical spectra is displayed for both angles and for different rotation speeds of the velocity selector.

A time–of–flight measurement with chopper and detector separated by a flight path of $d = 2.00(1)$ m was set up at the exit of the cryostat. The rotation speed of the chopper was fixed at 1000 rpm. Every 15 ms a neutron pulse with an intrinsic width of $\Delta t(\text{FWHM}) \approx 360$ μs from the finite opening passed the chopper (see Fig. 6.4 for the expected shape). The time bin of the data acquisition was set to 20 μs with an offset of 0.1 μs. There is an unknown offset t_0 between the pickup defining the start signal and the real opening of the chopper slit. This offset was determined experimentally by changing the geometric flight path length (see Fig. 6.9).

6.2.4 Weather of the converter vessel

The temperature of the converter vessel was measured throughout the experiment with a calibrated Cernox sensor, which was screwed to the aluminium container. There were only minor fluctuation of temperature, in the range of $\Delta T < 0.002$ K, for each individual measurement (see as an example Fig. 6.10 and for explanation of measurement Sec. 6.2.5). During an entire wavelength scan for one pressure setting the temperature fluctuations were $\Delta T < 0.03$ K (see Fig. 6.11).

The pressure was measured with a calibrated gauge for $p < 100$ bar relative. It was situated outside the cryostat, connected to the converter volume by a long capillary which is heat anchored at both radiation screens and can also be used for pumping. At pressures below 1 bar atmosphere it shows negative values and is not correctly calibrated. During measurements at SVP, established by continuous pumping, the gauge showed -1.600 bar. The measurements at $6, 11$ bar, and 16 bar, instead of $5, 10, 15$ bar where scattering data are available for comparison, have their origin in the confusion of absolute and relative pressure.

6.2.5 UCN production rate measurements

The conversion rate is measured for wavelengths between 3.5 Å and 10 Å with a step width of $\Delta\lambda = 0.25$ Å. As the rotation speed-to-wavelength

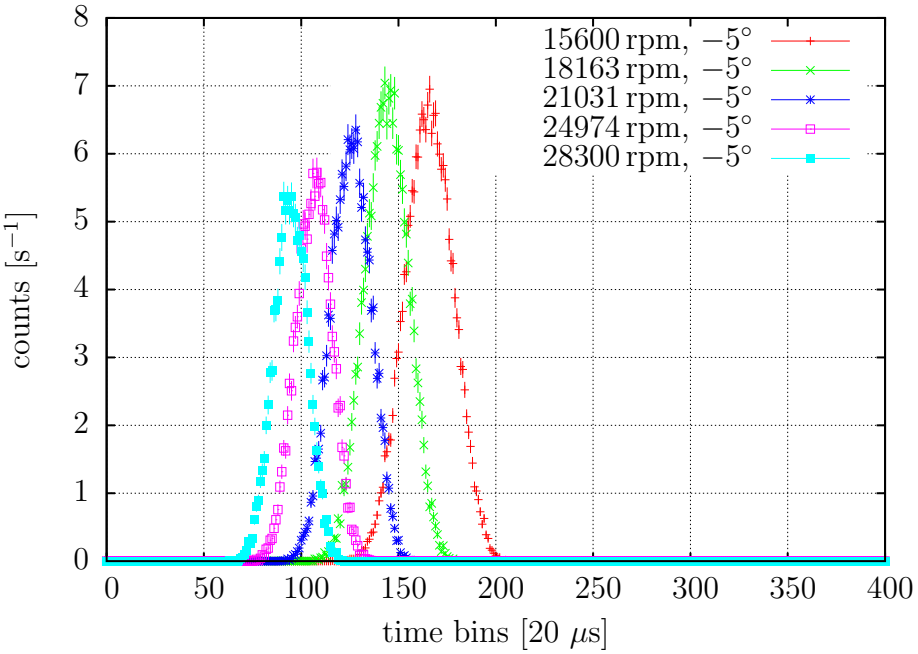

(a) Selector angle −5°

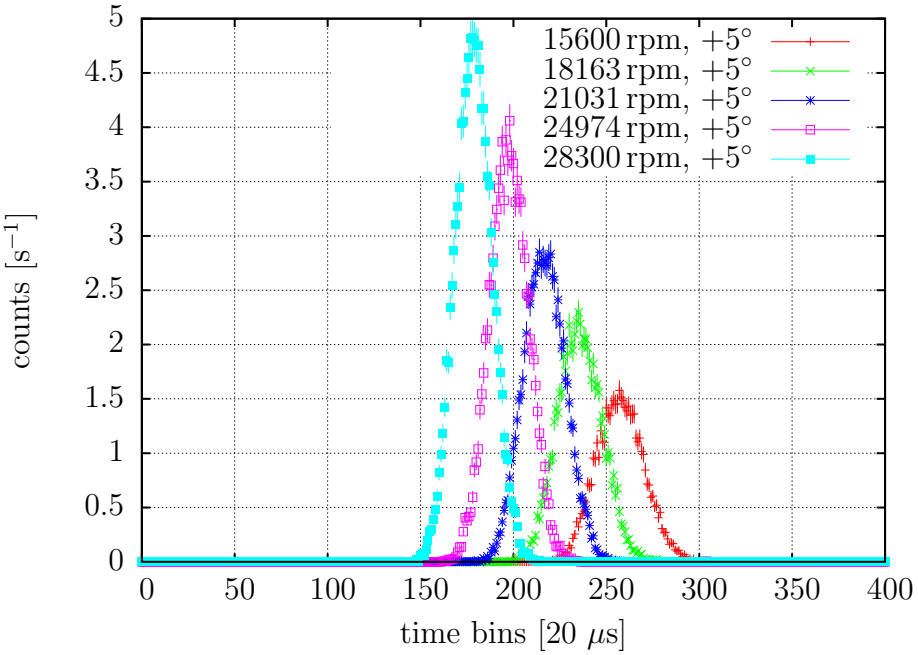

(b) Selector angle +5°

Figure 6.8: Raw data from time-of-flight measurements for the two angular settings used: (a) $\gamma' = -5°$ and (b) $\gamma' = +5°$.

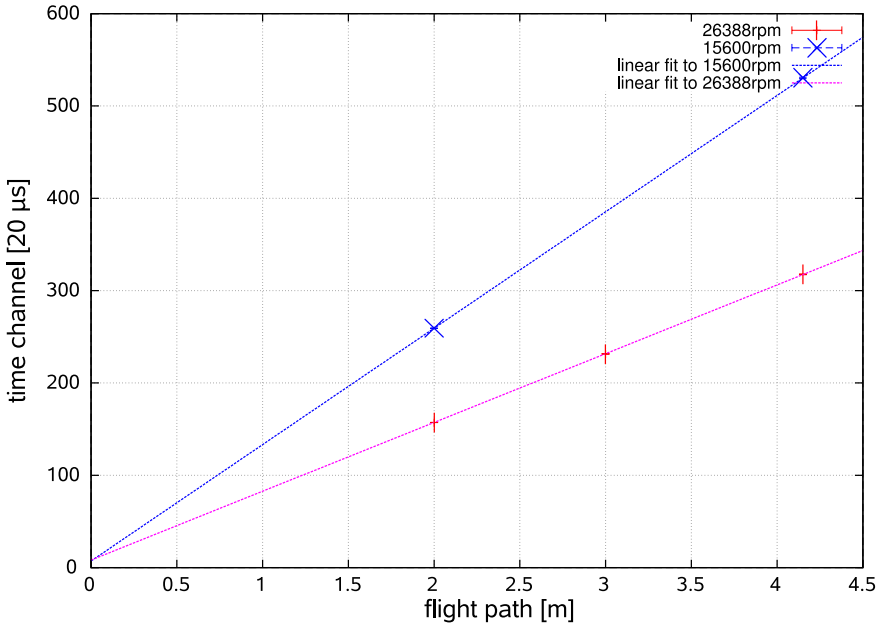

Figure 6.9: Determination of time offset t_0 from changing the length of the flight path. This is done for the selector speeds 26388 rpm and 15600 rpm.

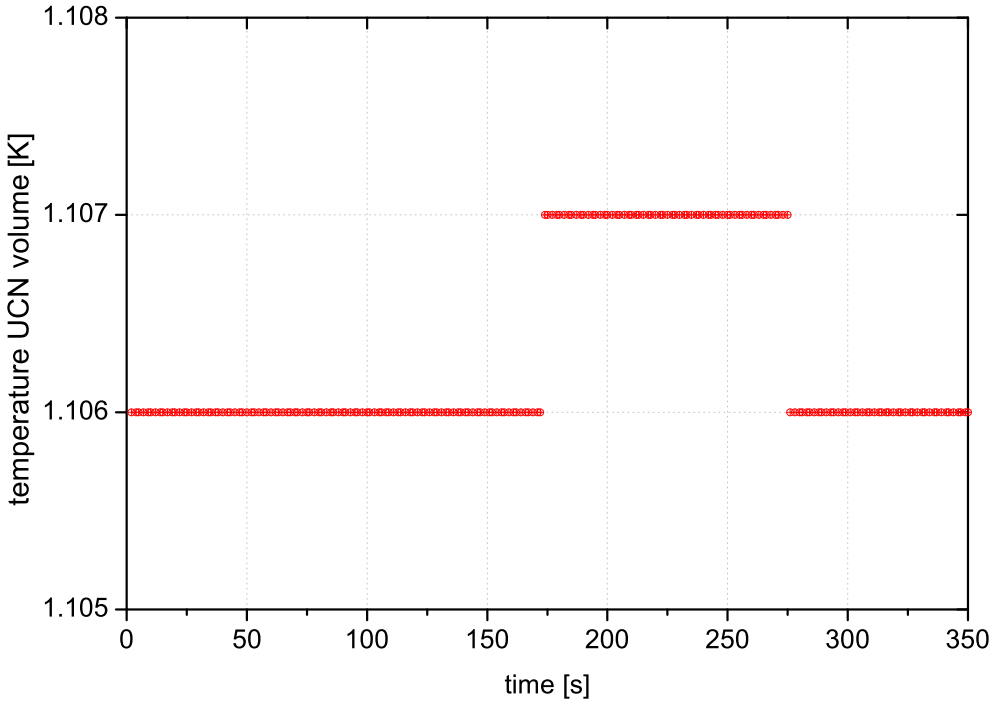

Figure 6.10: Typical change in temperature during one individual measurement (SVP 31-Sep-2008). The discrete step is caused by the resolution of the data acquisition. The typical accuracy at this temperature is 5 mK.

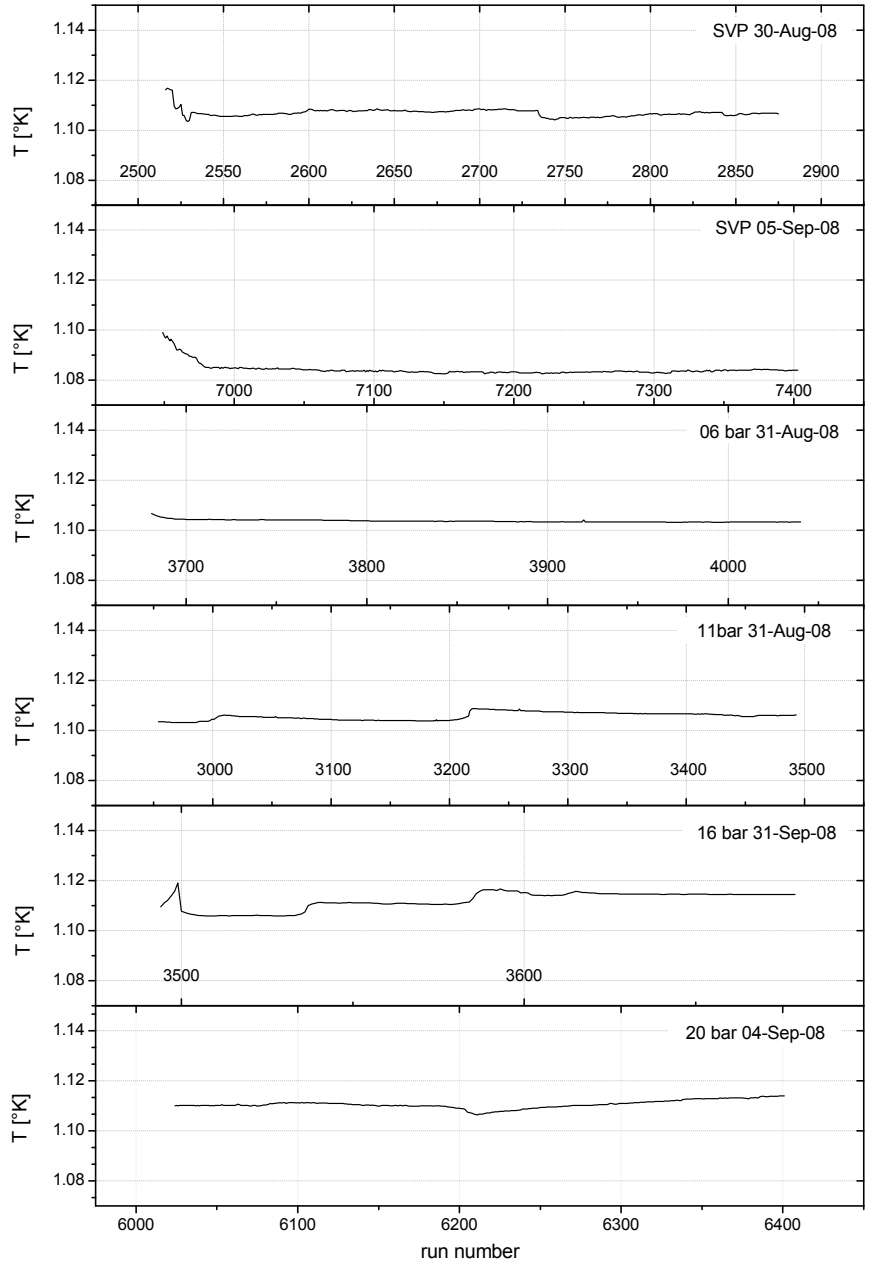

Figure 6.11: Typical change in temperature during an entire scan for some selected pressures and for examples from both wavelength ranges.

transformation was only approximate during data acquisition, I will in the following only refer to rotation speeds.

The pressure on the superfluid helium in the conversion volume has been applied through the superleak at temperatures just below the λ-point. Subsequently the whole volume was cooled down to the lowest accessible temperature of $T \approx 1$ K (see Tab. 6.3).

Apart from some control measurements at SVP the measurement proceedure is identically for both angular settings of the velocity selector and all pressures:

- For each pressure three up – down scans with fixed values for the rotation speed corresponding to $\Delta\lambda \approx 0.25$ Å are performed, starting with the slowest rotation speed within the allowed range of the selector. The up-down scans where performed in pairs to compensate for slow drifts.
- The production rate for a specific rotation speed in each scan is measured five times. In total there are 30 individual measurements for each selector speed.
- One individual measurement is divided into three phases (see Fig 6.12):
    1. The first 10 s are measured with closed cold neutron shutter, to determine the background.
    2. The following 40 s are measured with open shutter – cold neutrons pass through the apparatus. This allows to record the build-up and the saturation of UCN counts.
    3. The last 20 s the cold neutron shutter is closed. UCN are still counted to record the exponential decay which indicates the storage lifetime of the UCN in the system.

For technical and radio protection reasons it was not possible to measure consecutively the short and long wavelength range for each pressure. Therefore the angular setting was changed to $-5°$ after the conversion rates at long wavelength had been measured for all pressures. Then, starting with 20 bars the short wavelength rage was measured finishing with the multiphonon range at saturated vapour pressure. Thereafter some attempts have been made to measure the conversion rate for solid helium. These unfortunately fruitless endeavours are not described within this work. A complete summary of measurements at different converter pressures is given in Tab. 6.3

6.2.6 Control measurements at SVP

The experiment was continuously taking data for 12 days. For any data analysis it is crucial to know the stability of experimental conditions. This is

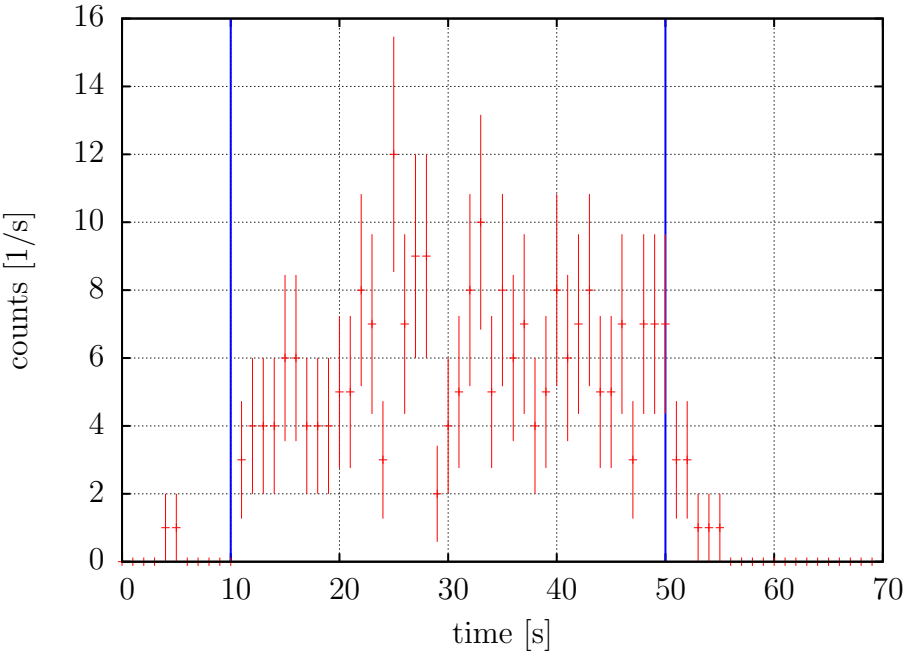

Figure 6.12: UCN detection vs. time for a typical individual measurement. The opening and closing of the cold neutron beam is indicated by vertical lines.

date	pressure [bar]	wavelength range [Å]	Temperature [K]
30 August 2008	SVP	$5.5-9.75$	1.111(5)
31 August 2008	11	$5.5-9.75$	1.105(2)
31 August 2008	16	$5.5-9.75$	1.115(5)
01 September 2008	6	$5.5-9.75$	1.105(2)
01 September 2008	SVP	$5.5-9.75$	1.080(1)
01 September 2008	11	$5.5-9.75$	1.105(2)
02 September 2008	3	$5.5-9.75$	1.108(3)
03 September 2008	20	$5.5-9.75$	1.104(2)
04 September 2008	20	$3.5-6.50$	1.112(2)
04 September 2008	16	$3.5-6.50$	1.110(2)
04 September 2008	11	$3.5-6.50$	1.107(5)
04 September 2008	6	$3.5-6.50$	1.105(3)
04 September 2008	3	$3.5-6.50$	1.108(1)
05 September 2008	SVP	$3.5-6.50$	1.109(1)
05 September 2008	SVP	$5.5-9.75$	1.109(1)
09 September 2008	SVP	$5.5-9.75$	1.109(1)

Table 6.3: List of all wavelength-resolved conversion rate measurements. The stated error of each temperture indicates the stability of the temperature during the scan.

done by controlling and monitoring directly important parameters – temperature, pressure of the isolation vacuum, pressure of the extraction line – and by returning from time to time to a standard measurement. In particular we worried that the pressure of $\sim 3 \cdot 10^{-6}$ mbar in the extraction line will lead to gas freezing out on the extraction window and tubing. This should be recognisable in a decrease of count rate with time. A well-reproducible indicator with high statistics is the integral UCN count rate of the one-phonon peak at SVP. Five times during the experiment we have measured the UCN production rates in the vicinity of the single-phonon-peak for SVP.

6.2.7 Measurement of time constants and background

Measurements to investigate changes in the emptying time constant t_e with changing converter pressure and temperature have been carried out additionally to the sole conversion rate scans. These measurements were performed at high UCN statistics in the single-phonon-peak. From measurements at constant selector speeds with very low UCN count rates and high cold neutron flux ($\omega = 20489$ rpm, $+5°$) it is possible to deduce a conservative upper limit for the beam-dependent background. These measurements have been done for SVP and 20 bar.

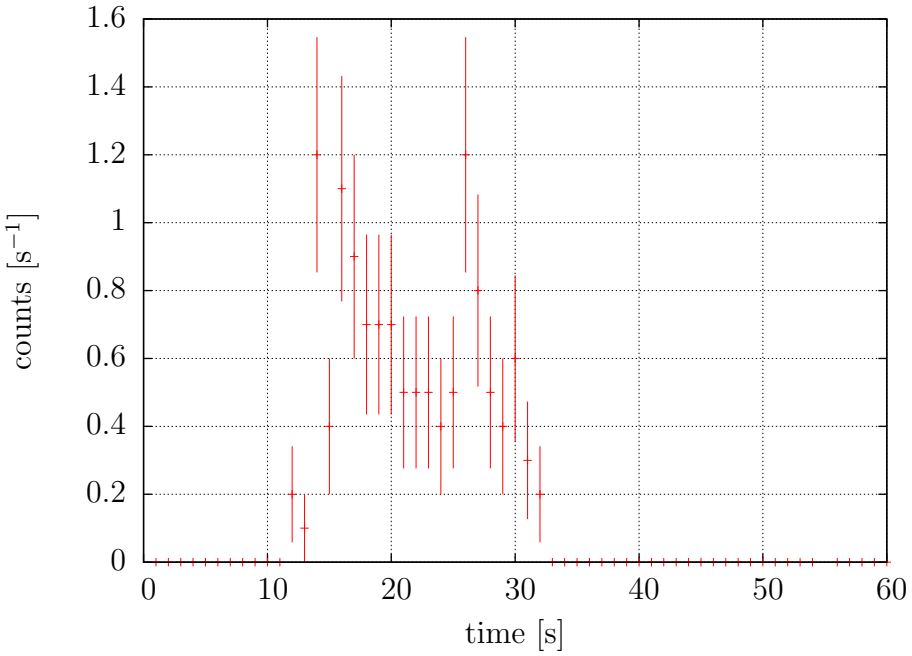

Figure 6.13: Measurement at $T = 2.05$ K, SVP in the single-phonon-peak. Up-scattering reduces the UCN count rate significantly compared to measurement at lower temperatures (see Fig. 6.12). As UCN are stored only for very short times, this measurement can be used to estimate the background with closed cold neutron shutter. The measurement scheme deviates from the standard described in Sec. 6.2.5. Here the CN shutter is closed th first 10 s, then opened for 20 s, and closed again while the counting continuous for 30 s.

6.3 Data Analysis

6.3.1 Background

One motivation for measurements with high statistics at selector speeds where the UCN production is very weak was to estimate beam-dependent background. A second type of measurements at high temperature with large UCN statistics and significant up-scattering of UCN allows to estimate the beam-independent background. A measurement at $T = 2.05(5)$ K in the maximum of the conversion rate curve is shown in Fig. 6.13.

At this temperature the UCN loss by up-scattering through absorption of thermal excitations in the liquid is the most important loss mechanism. Therefore the number of UCN which are actually detected inside the UCN detector is strongly reduced, whereas the number of cold neutrons which are scattered into the UCN detector remain the same as at low temperatures. As UCN are only stored for very short times, all counts after $\Delta t = 5 \cdot \tau \approx 4$ s after the closing of the beam shutter are background. The same is the case

for all counts before opening of the beam. Therefore, this measurement can be used to estimate a upper background limit using Poisson-statisics and 0 counts in the time intervalls without beam. This gives a limit of $\bar{r}_{\mathrm{bg}} \leq 7.7 \cdot 10^{-3}$ s^{-1} (C.L. 95%) for beam-independent background with closed neutron beam. This is derived from the null measurements in the range 0 s $< t <$ 10 s and 35 s $< t <$ 60 s. Each time slice of $\Delta t = 1$ s was measured ten times, the total measurement time was 350 s. This gives a beam-independent background of $\bar{r}_{\mathrm{bg}} = 0^{+3.9}_{-0.0} \cdot 10^{-3}$ s^{-1}.

The CN beam-dependent background $y_{\mathrm{bgd}}(\omega)$ is estimated from fits to the exponential growth of UCN count rate after opening the beam shutter (shown in Fig. 6.14a). If there is any beam-dependent background it should have an instantaneously step as signature, whereas the UCN counts follow a simple exponential growth. The relative background-to-signal ratio is highest in the count rate minimum at 20489 rpm ≈ 7.5Å of the conversion curve. This data point should give the best sensitivity for the background, but it is possible to deduce values also for other wavelengths.

In all measurements the cold neutron shutter is completely open at $t_{\triangleleft} =$ 10.8 s and closed at $t = 50.8$ s. This can be found by analysing the beam monitor data. In the first seconds, after opening, UCN have to pass along the guides before they can be counted in the detector. Once the spectrum of detected neutrons is similar to the one in the converter volume the rise will be proportional to $1 - \exp(-(t - t_{\triangleleft})/\tau_{\mathrm{e}})$. This process can approximatively be described by:

$$\dot{N}(t) = \begin{cases} y_{\mathrm{bgd}}(\omega) + \bar{r}_{\mathrm{bg}} + \frac{t-t_{\triangleleft}}{\zeta} \cdot N_0 \left(1 - \mathrm{e}^{-\frac{t-t_{\triangleleft}}{\tau_{\mathrm{e}}}}\right) & : \quad t_{\triangleleft} \leq t < t_{\triangleleft} + \zeta \\ y_{\mathrm{bgd}}(\omega) + \bar{r}_{\mathrm{bg}} + N_0 \left(1 - \mathrm{e}^{-\frac{t-t_{\triangleleft}}{\tau_{\mathrm{e}}}}\right) & : \quad t_{\triangleleft} + \zeta \leq t \end{cases} \tag{6.10}$$

where the first part describes a linear ramp from $t_{\triangleleft}$ to ζ the moment the full accessible UCN spectrum is detected. This description is choosen to account for the initial process of UCN passing throught the extraction system with different velocities after opening the CN-shutter this process can not be described with $\dot{N}(t) \propto 1 - \exp(-(t - t_{\triangleleft})/\tau_{\mathrm{e}})$. After a time ζ the velocity distribution of UCN counted in the detector will be nearly identical to that in the conversion volume. Then it is possible to describe the remaining increase in count rate with the second part of Eq.(6.10).

For minimisation of correlations the determination of the beam-dependent background for a given velocity speed with its corresponding capture flux was done in three steps:

1. The time constant τ_{e} describing the storage lifetime of the entire system is constant for different selector speeds. It can be therefore be deter-

mined for all selector speeds from a fit of the exponential function:

$$\dot{N}(t) = \dot{N}_0 \mathrm{e}^{-\frac{(t-t_0)}{\tau_\mathrm{e}}},$$

to the decreasing count rate $\dot{N}(t)$ after the the cold neutron shutter is closed at $t_0 = 50.8$ s. The fitting range is: 50.8 s – 65 s.

2. The saturation count rate $N_\infty = N_0 + y_\mathrm{bgd}(\omega) + \bar{r}_\mathrm{bg}$ is determined in the interval 25 s to 49 s, with a fit to

$$N_\infty(1 - \exp(-(t - t_0)/\tau_\mathrm{e}),$$

where τ_e is given by the first fit.

3. Finally, Eq.(6.10) is fitted to the data in the interval 10.8 s to 22 s to determine the last two free parameters ζ and $y_\mathrm{bgd}(\omega)$.

Four measurements, at $17727, 20489, 28300$ rpm at $\gamma' = +5°$ and 28300 rpm at $\gamma' = -5°$, with sufficient statistics have been made. They are shown in Fig. 6.14b. The beam-dependent background should, in first approximation as the efficiency $\epsilon \ll 1$ of the UCN detector, be proportional to the incoming capture flux of cold neutrons:

$$y_\mathrm{bgd}(\omega) = k \cdot \Phi_\mathrm{CN}(\omega). \tag{6.11}$$

Note that Φ_CN is the independent variable, for which the count rate of the beam monitor can be taken, and ω only its label. A linear fit of Eq.(6.11) to the four data points gives $k = (5.6 \pm 6.0) \cdot 10^{-7}$ with a reduced–$\chi^2 = 1.38$ (see Fig. 6.14b).

The UCN count rate of all measurements are corrected for a beam-dependent background $y_\mathrm{bgd}(\omega)$ from Eq.(6.11) and an beam-independent one of $\bar{r}_\mathrm{bg} = 0^{+3.9}_{-0.0} \cdot 10^{-3}$ s^{-1} the previous estimation.

6.3.2 Temporal decrease of UCN count rates

We have remeasured the UCN production rates in the vicinity of the single phonon peak at saturated vapour pressure several times. In Fig. 6.15, the time-dependence of the count rate in the peak is shown.

The time dependence can be described by an exponential function:

$$\dot{N}\,(t) = \dot{N}_0 \cdot \mathrm{e}^{-\frac{t}{\mathcal{T}}} + A_0,$$

with the time constant $\mathcal{T}$ and a large constant contribution A_0. This large constant offset could be interpreted that the gas is not freezing out on the

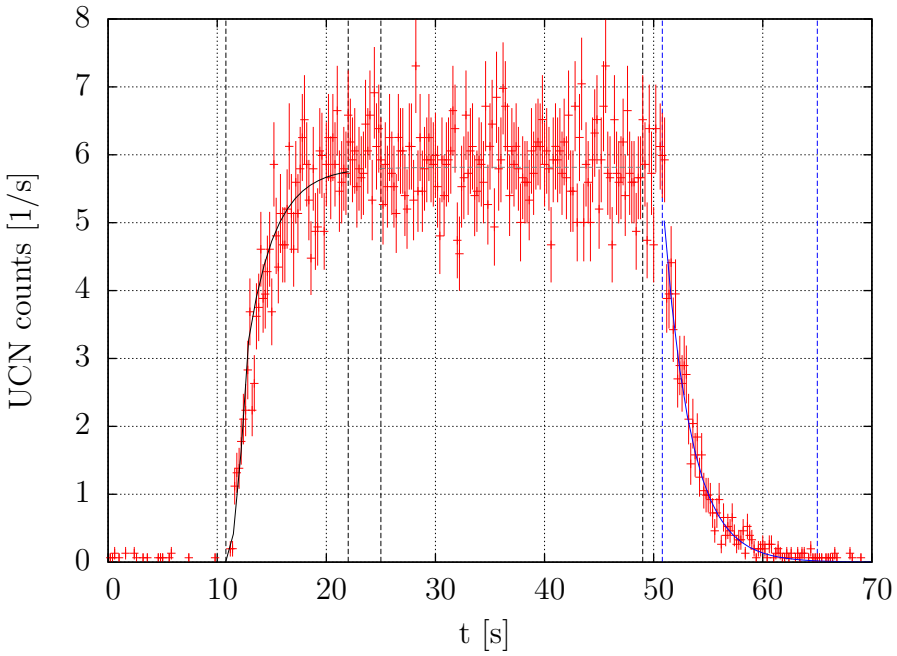

(a) Background fit procedure.

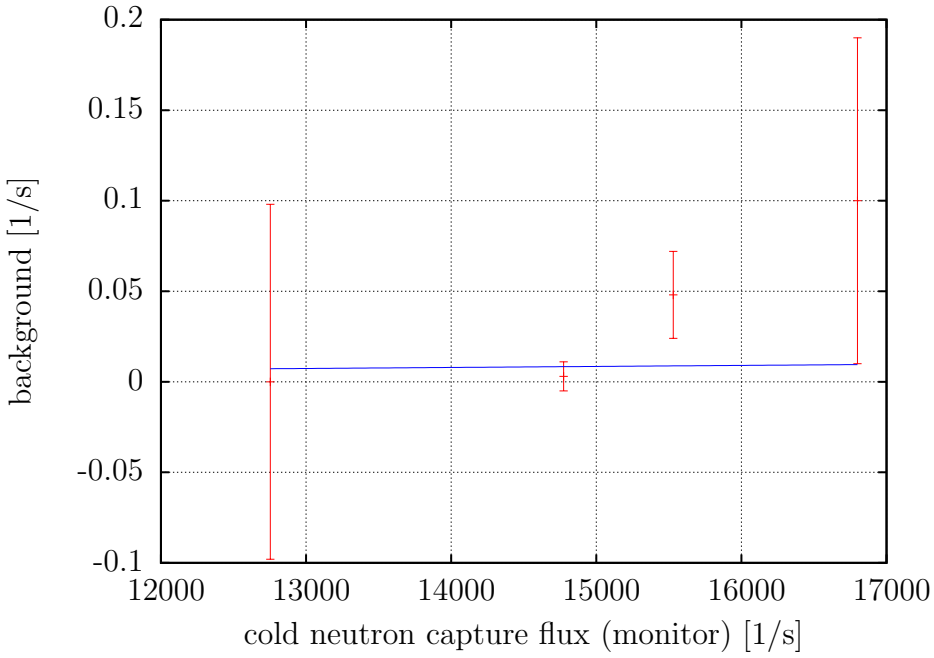

(b) Beam dependent background.

Figure 6.14: (a) Sum of individual measurements at $\omega = 17727$ rpm. The vertical lines indicate the three different fit ranges used to determine the beam-dependent background. The solid lines in these ranges are the best fits to the data, each with a reduced-χ^2 close to unity. (b) Estimation for CN-flux dependent background from fits to $y_{\mathrm{bgd}}(\omega)$ at $\omega = 17727, 20489, 28300$ rpm at $\gamma' = +5°$ and 28300 rpm at $\gamma' = -5°$. The cold neutron capture flux increases with decreasing wavelength.

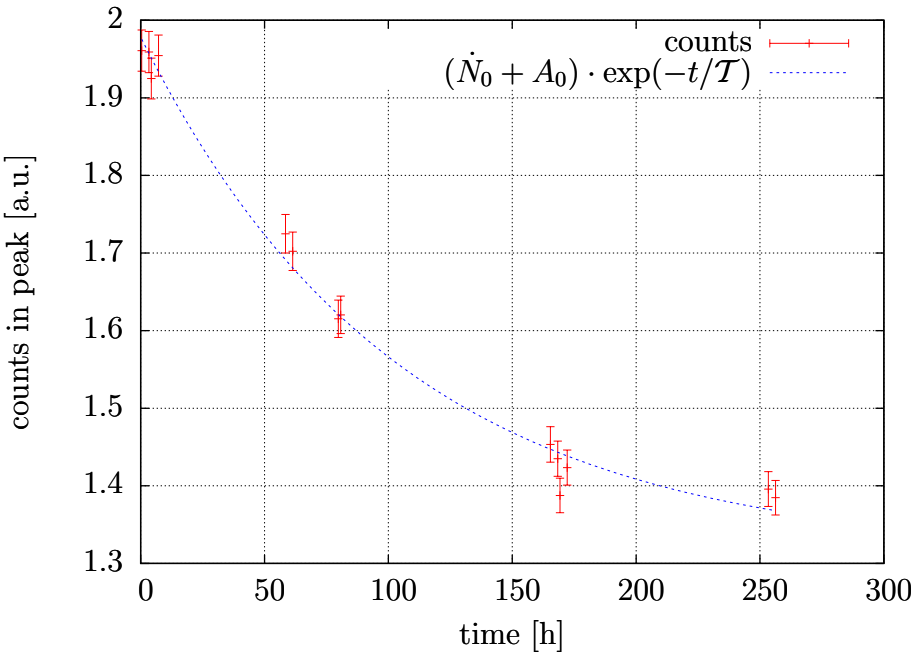

Figure 6.15: Temporal decrease single-phonon peak count rate at SVP. Each point cooresponds to the integral over the single-phonon peak of a single scan at SVP (rotation speeds $f < 20489$ rpm). They often occur in groups, as one measurement consists of several scans. The exponential fit has a reduced $\chi^2 = 1.19$ for the values $\dot{N}_0 = 0.67(3)$ s^{-1}, $A_0 = 1.31(3)$ s^{-1}, and $\mathcal{T} = 104(12)$ h.

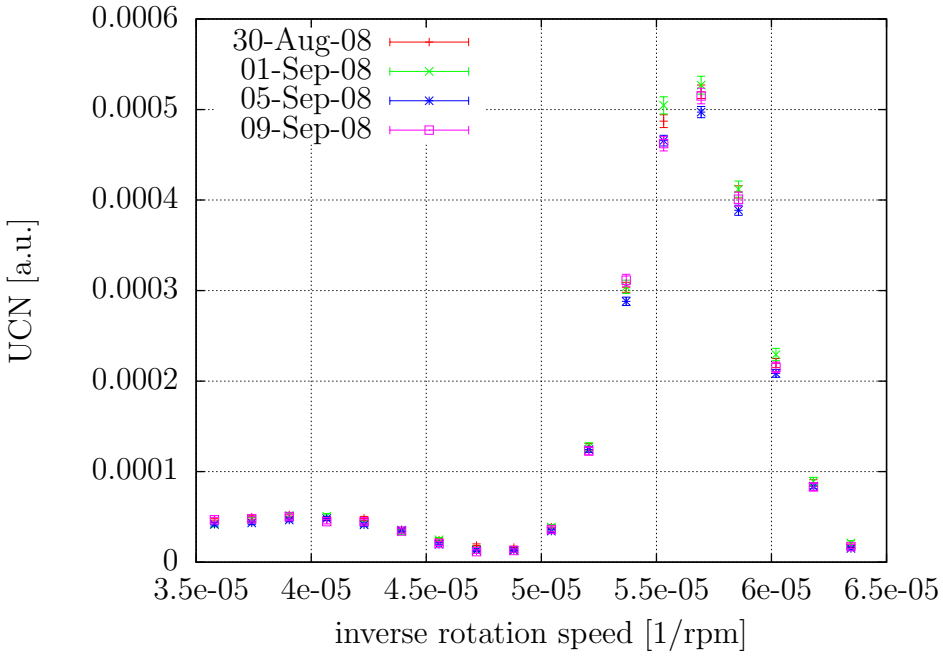

Figure 6.16: Control measurements of the peak area at saturated vapour pressure, corrected for the temporal decrease in extraction efficiency.

transmission window but somewhere on the stainless steel exit tubes. In this case, a part of the UCN would not be affected, corresponding to A_0. The result was used to correct the intensities in all measurements by scaling factors depending on the time of the individual measurement. The uncertainty of the scaling factor (5% from the fit in Fig. 6.15), was considered as systematic error. In Fig. 6.16 all control measurements are shown, corrected for temporal decrease in extraction efficiency.

6.3.3 Conversion from time-of-flight to wavelength

The time-of-flight can be transformed to a corresponding wavelength with:

$$\lambda = \frac{h}{m_{\mathrm{n}} v} \tag{6.12}$$

where $v = (t - t_0)/d$ is the mean neutron velocity. The finite time offset $t_0 = 150(30)$ μs was determined with a reduced-χ^2 fit of two lines with a common intersection at t_0 to the data from the measurement described in Sec. 6.2.3. This combined fit has a reduced-$\chi^2 = 4$. Fitting a line only to the data for $\omega = 15600$ rpm yields the same value for t_0 with a smaller error (± 17 μs) and smaller reduced-$\chi^2 = 1.34$. Using this t_0 with the flight distance $d = 2.00(1)$ m one obtains values for λ.

6.3.4 Cold neutron spectrum inside the converter volume

With the time-of-flight measurements made for different selector settings, it is possible to deduce for each selector velocity a corresponding mean wavelength. It is important to keep in mind that each of these wavelength-"labels" corresponds to a spread cold neutron spectrum, and not to this wavelength alone.

For the full and correct interpretation of the measured wavelength-resolved UCN production rate it is cardinal to know for each selected wavelength the exact spectrum inside the conversion volume. Each time-of-flight spectrum $\Phi_{\mathrm{tof}}(t)$ measured at the exit of the cryostat is the convolution of the spectrum inside the converter volume $\Phi(\lambda)$ and the chopper opening function $A(t)$, weighted with the function describing the finite depth w of the detector $D(\lambda, d, w)$ at the distance d:

$$\Phi_{\mathrm{tof}}(t) = \int \mathrm{d}t'\, A(t-t') \left(\int \mathrm{d}\lambda\, \Phi(\lambda) D(\lambda, d, w) \right). \tag{6.13}$$

The opening function of the chopper can be described as a rounded triangular (see Fig. 6.4 and Eq.(6.6)) with a base line of $\Delta t = 720(30)$ μs. The detection function is given by:

$$D(\lambda, d, w) = \mathcal{H}\left(\frac{d \cdot \lambda m_{\mathrm{n}}}{h} - \frac{d - w/2}{v} \right) \cdot \mathcal{H}\left(\frac{d + w/2}{v} - \frac{d \cdot \lambda m_{\mathrm{n}}}{h} \right) \cdot \epsilon,$$

where v is the velocity of the neutron detected, $d = 2.00(1)$ m is the length of the flight path, $w = 44(1)$ mm the width of the detector, and ϵ a normalisation factor. The effect of the detector is a blurring of the spectrum, stronger for long wavelengths, but in general negligible compared to the spread from the chopper opening function. Therefore the data was only deconvoluted with the chopper opening function using the `deconvlucy(`$\Phi_{\mathrm{tof}}(t), A(t)$`,5)` algorithm from MATLAB[2][Leu08]. This algorithm uses the convolution theorem:

$$\mathcal{F}(f \otimes g) = \mathcal{F}(f)\mathcal{F}(g), \tag{6.14}$$

which states that the Fourier transform of the convolution of f and g is identical to the multiplication of the Fourier transformed of f and g. In particular the algorithm is based on maximising the likelihood of the resulting ToF spectrum being an instance of the original ToF spectrum inside the

[2]Matlab version 7.5 from MathWorks, see http://www.mathworks.com,

pressure [bar]	peak position [Å]	w(FWHM) [Å]	intensity [10^{-3}/CN-monitor]	relative intensity
SVP	8.69(1)	0.81(2)	2.57(3)	1.000
6	8.30(1)	0.77(2)	1.83(2)	0.712(5)
11	8.17(1)	0.78(1)	1.46(2)	0.568(4)
16	8.09(1)	0.80(2)	1.22(2)	0.475(4)
20	8.07(1)	0.84(6)	1.04(2)	0.405(3)

Table 6.4: Pressure dependence of single-phonon peak position and intensity. The width w comes from the convolution with the incident wavelength distribution.

converter under Poisson statistics. This is done in five iterations to avoid artefacts from noise. Concomitant it smoothens the data. A comparison of measured to deconvoluted spectra for two wavelength is shown in Fig. 6.17.

For the transformation of the time scale to wavelength scale I use the results from Sec. 6.3.3. After correcting for particle flux, I fit a Gaussian in the range $x_{\max}-1.2\sigma < x < x_{\max}+1.2\sigma$ to each spectrum to determine the peak position as wavelength-"label" of the spectrum. The large uncertainty of the accuracy of such a label is shown in Fig. 6.17b, from which it could be easily argued that the label should be shifted by ± 0.1 Å.

6.3.5 UCN conversion rates in superfluid helium under pressure

The shift of the prominent single-phonon peak in UCN production rate from slow rotation speeds to faster (long wavelength to shorter) with pressure is shown in Fig. 6.18. Simultaneously the intensity decreases. As it is the only prominent peak it can be identified as the contribution from single phonon processes to the differential UCN production rate. It may be fitted with a Gaussian function. In Tab. 6.4 its peak position, width, and intensity (peak area) for each pressure is given.

The calculated relative intensities listed in Tab. 3.1 of Chapter 3.3 are in good agreement with the measured ones. The relative intensity for $6, 11$ bar and 16 bar are slightly smaller than the calculated values for $5, 10$ bar and 15 bar which is expected as the intensity decreases with pressure.

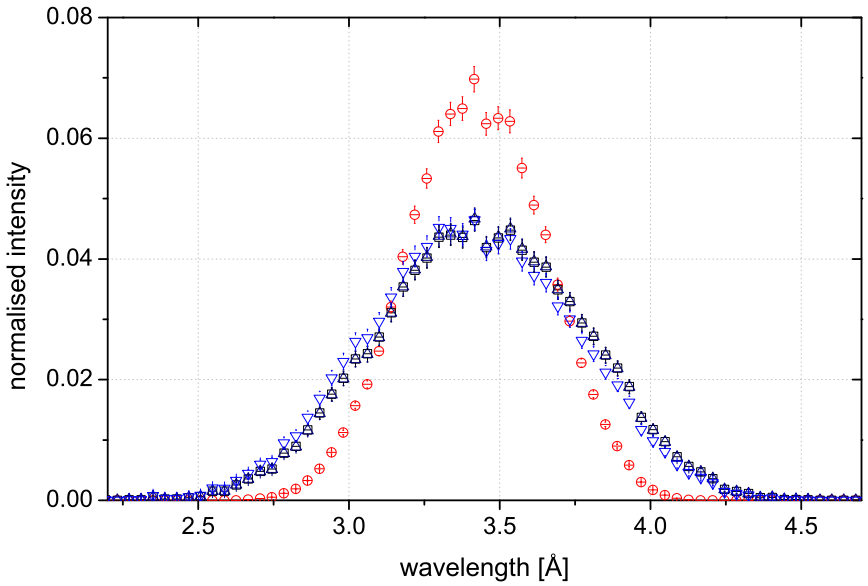

(a) $\lambda \approx 3.5$Å

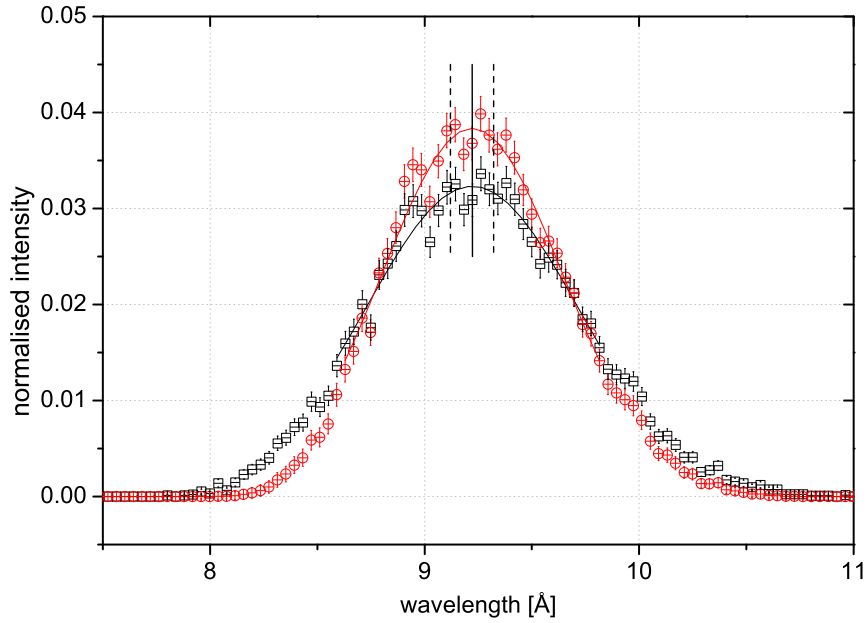

(b) $\lambda \approx 9.2$Å

Figure 6.17: ToF spectra at 3.5 Å (a) and 9.2 Å (b) before (⊟) and after deconvolution (⊖). In (a) the corrections for deadtime of the detector (△) and particle flux (▽) are also shown. The lines in (b) are least-χ^2 fits of a Gaussian function to the peak, the vertical line indicate the uncertainty for a "wavelength-label" (±0.1Å) for this spectrum.

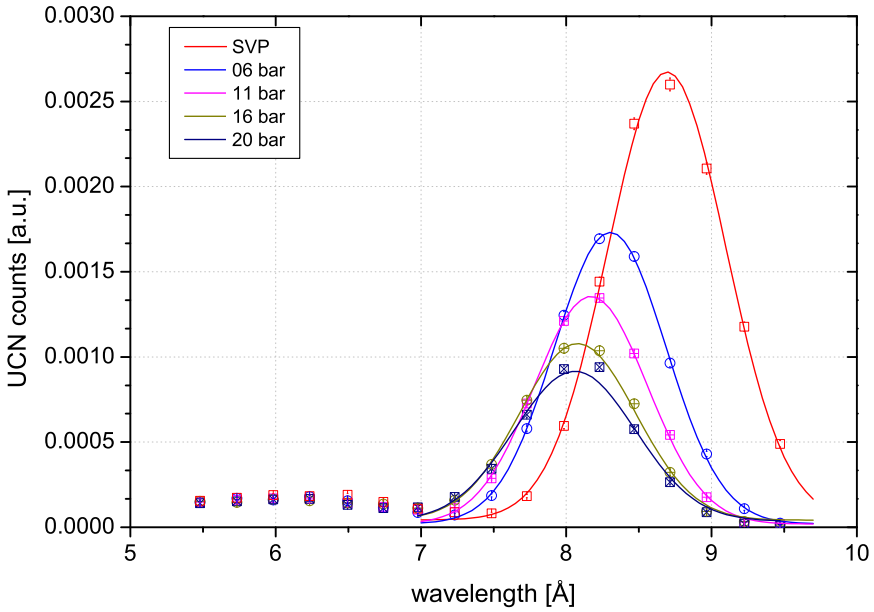

Figure 6.18: Decrease in intensity of the prominent peak of the UCN production rates with pressure for SVP (□) and $p = 6\,(\bigcirc), 11\,(\boxplus), 16\,(\oplus)$ bar, and 20 (⊠) bar.

6.3.6 Comparison with UCN production rates calculated from inelastic scattering data

A direct comparison of measured UCN production rates to rates expected from calculation with the deduced UCN scattering function (Sec. 3.3), can only be made if the wavelength distribution of the incoming beam is correctly taken into account. This can be done for each selector speed by integration over Eq.(2.23):

$$\frac{\mathrm{d}P_{\mathrm{II}}\,(V_{\mathrm{c}})}{\mathrm{d}\lambda_{\mathrm{i}}} = N\sigma\, V_{\mathrm{c}} \frac{2}{3\lambda_{\mathrm{c}}} \left(\frac{\mathrm{d}\Phi}{\mathrm{d}\lambda_{\mathrm{i}}}\right)_{\mathrm{TOF}} \lambda_{\mathrm{i}} \cdot s_{\mathrm{II}}(\lambda_{\mathrm{i}}), \tag{6.15}$$

where $(\mathrm{d}\Phi/\mathrm{d}\lambda_{\mathrm{i}})_{\mathrm{TOF}}$ is the ToF-spectrum after deconvolution. For the calculations I have used for $s_{\mathrm{II}}(\lambda_{\mathrm{i}})$ interpolated scattering data in the range $\lambda > 4.5$ Å and the analytic expression Eq.(3.4) for shorter wavelength. Thus I get for each setting of the velocity selector a value of the expected UCN production rate that can be compared directly with the measured values. In Fig. 6.19 the calculated and measured UCN production rates for all pressures are compared.

The measured UCN production rates are normalised with the particle flux

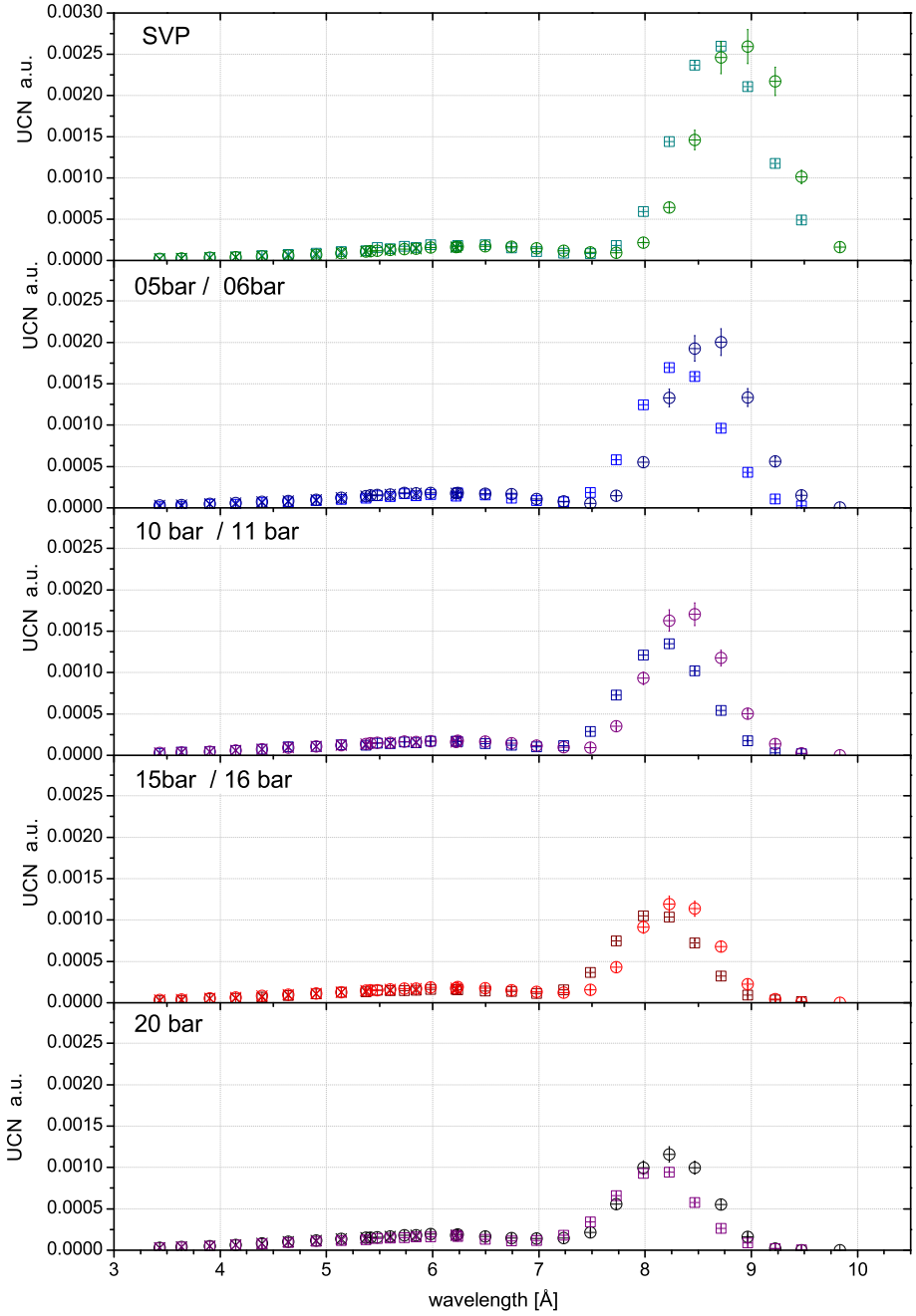

Figure 6.19: Comparison of measured differential UCN production rates.(⊞,⊠): calculated UCN production rates. (⊕,⊗) measured UCN production rates. Where $+, \times$ indicates $\gamma' = +5°$ and $\gamma' = -5°$ selector angle, respectively.

pressure [bar]	peak position measured [Å]	peak position calculated [Å]
SVP	8.69(1)	8.92(2)
06	8.30(1)	8.54(4)
11	8.17(1)	8.39(2)
16	8.09(1)	8.30(2)
20	8.07(1)	8.26(2)

Table 6.5: Measured and calculated UCN production rates for p = SVP, 6, 11, 16 bar and 20 bar. The position of the single-phonon peak is determined by a Gaussian fit to the peak range. The calculated positions for $p = 6, 11,$,and 16 bar are values obtained from interpolation with an exponential decay of the values in Tab. 3.1.

measured simultaneously with the monitor detector at the exit of the cold neutron guide. The calculated UCN production rates are normalised by a common factor $1.34 \cdot 10^6$ to scale the measured rates. This scaling factor was not measured, as this would require an absolute knowledge of extraction efficiency. It was defined by matching the maximum count rate of the measurement to the calculated maximum countrate at SVP. An systematic error of 10% can be estimated in comprison with an average scaling factor of $1.21 \cdot 10^6$ for all pressures. The indicated error for the calculated rate is derived from the uncertainty of the inelastic neutron scattering data (see Sec. 3.3). Note that the errors of the calculated points in the single-phonon region are correlated since they depend on the error of the intensity of $S^* = Z(Q)$ for $Q = 2\pi/\lambda_c$ from the Gibbs data [Gib96]. The absolute position of the spectra is dependent on the calibration of the wavelength scale described in Sec. 6.3.3. The positions of the measured single-phonon peak (see Tab. 6.5), estimated with a Gaussian fit to the peak, are displaced to shorter wavelength compared to the calculated ones for all pressures.

They are shifted in average by $\Delta\lambda \approx 0.22$ Å to shorter wavelength. The measured relative single-phonon production intensity for He-II under pressure with respect to the measurement at SVP is in general smaller than deduced from the Gibbs data. The multiphonon ranges agree well to the expectations, although for increasing wavelength the points are increasingly shifted to longer wavelength compared to the calculated.

Assuming that the point of intersection of the dispersion relation of He-II with the free neutron dispersion relation, derived from the inelastic neutron scattering data, is correct in the case of SVP and 20 bar it is possible to find new values for the time-of-flight path length d and the offset t_0. With $d = 1.965$ m and $t_0 = 167$ μs the calculated and measured UCN rates have a high degree of accordance (see Fig.6.20, where an average scaling factor was used). The only exception are the measurement at 6 bar and less the one at 11 bar which seam to be shifted to shorter wavelength. This can be

expected, as the change of the dispersion relation between 5 bar and 6 bar and between 10 bar and 11 bar is of greater importance as for higher pressures (see Fig. 3.7). Thus the shift in the intersection of the free neutron dispersion relation with the He-II dispersion relation is visible between the results from the scattering data and the direct UCN data. For the measurements at 16 bar the intersection point is also shifted with respect to 15 bar, but as the change in the He-II dispersion relation in this pressure range is less pronounced it is hardly visible in our measurement.

6.4 Discussion

The measured cold neutron to UCN conversion rate in He-II under pressure agrees good to the predictions made from inelastic neutron scattering data. Only the wavelength-dependency does not correspond. The dispersion curve of superfluid helium and therefore also its intersection with the free neutron dispersion curve is known with a high accuracy from several measurements. It is very likely that the disagreement of the wavelength dependency has its origin in our measurement or in my analysis.

The most trivial explanation is a wrong measurement of the length of the flight-path of the time-of-flight measurements. Correcting this length by -3.5 cm brings the wavelength scales in accordance with expectations. However, an incorrect measurement of this magnitude should have been apparent during measurement and can therefore be most likely excluded as explanation.

An alternative explanation is an systematic, wavelength-dependent shift of the wavelength scale to shorter wavelength. This could have its origin in the asymmetry of the spectrum. Fitting these with symmetric Gaussians probably give maxima at too short wavelengths for each Tof spectrum. This asymmetry is a result of the convolution of the initial asymmetric white spectrum with the opening functions of the velocity selector and the chopper. The transformation by the detector function further increases the asymmetry. Calculation made together with K. Leung [Leu08] show that the transformation of the spectrum by the detection function increases with wavelength. Nevertheless, it would account only for 0.15 Å of the observed shift of ~ 0.23 Å, even if the transformation is taken as a pure shift of the ToF spectra, instead of an asymmetric blurring. Combining this with an asymmetric determination of the most probable wavelength might allow to determine "wavelength-labels" which better accord with predictions.

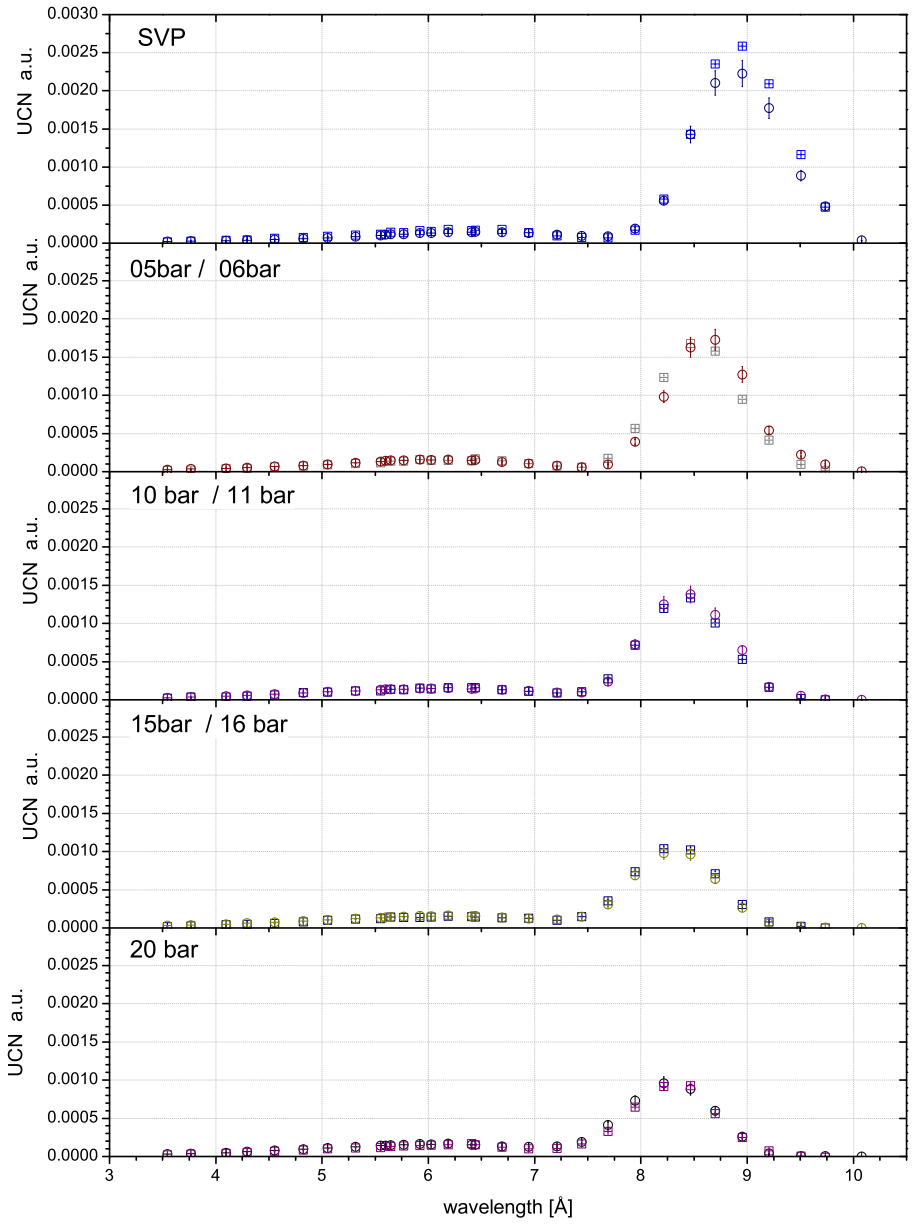

Figure 6.20: Comparison of measured and calculated differential UCN rates with fine tuned ToF parameters to match positions of single-phonon peaks at SVP and 20 bar. The general scaling factor to match calculated to measured rates is average over all 5 pressures.

Chapter 7

Implementation of a new UCN source at the ILL

Initially within the framework for a new instrument, GRANIT a gravitational spectrometer, a more powerful source for the ILL had to be developed. The conception and developments made to bring ILL back to the forefront of UCN physics are described in the following paragraphs. The chapter follows in large parts Ref. [Sch08a].

7.1 A UCN source for GRANIT and maybe more

The solutions for Schrödinger's equation for a neutron bouncing on a reflecting horizontal surface in the Earth's gravitational field are given by Airy functions [Flü71, Lus78]. This textbook example of bound energy states in a linear potential has been demonstrated experimentally at the high flux reactor of the Institut Laue Langevin [Nes02, Nes03]. A new gravitational spectrometer, GRANIT [Nes06, Kre08], is being built to investigate these quantum states further, and to induce resonant transitions between gravitationally bound quantum states. Proposed applications are a refined measurement of the electrical charge of the neutron, the search for the axion [Bae07, Bae08] and other additional forces beyond the standard model. Experiments at ILL's present facility PF2 for ultracold neutrons are limited by counting statistics and systematic effects due to vibrations [Pig07]. The source will be placed on a dedicated 8.9 Å beam in the level C of the reactor building. A second beam for a second source is foreseen for the future.

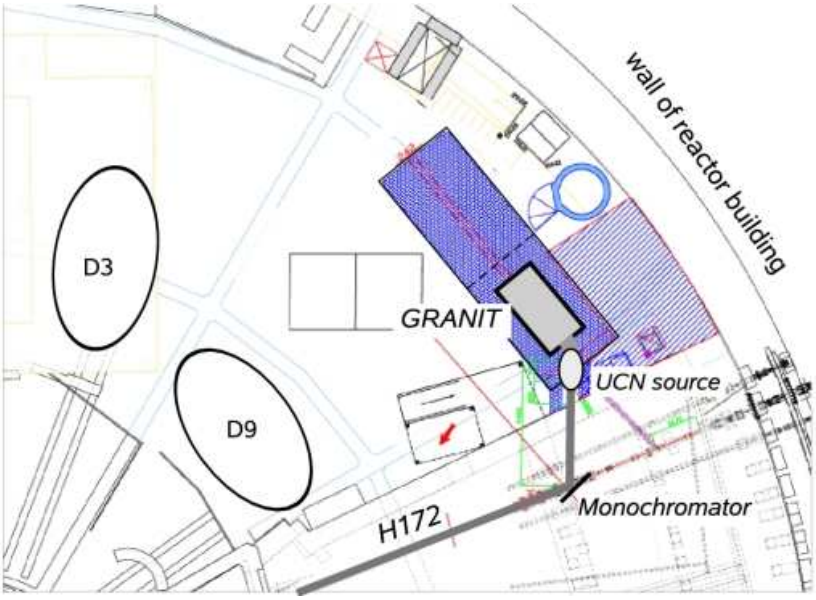

Figure 7.1: Setting of the monochromator, the source, and GRANIT inside level C of the ILL. (For more details see: www.ill.fr/pages/science/imgs/PlanInstILL.gif)

7.2 Source concept

The UCN source employs cold neutrons from the neutron beam H172 on level C of the high flux reactor at the ILL (see Fig. 7.1). A crystal monochromator, positioned 12 m downstream from the horizontal liquid-deuterium cold source situated in-pile reflects neutrons with 8.9 Å out of the direct beam. It feeds a secondary, 4.5 m long neutron guide equipped with $m = 2$ supermirror coatings. The superfluid-helium UCN converter with its special UCN extraction system is installed at the end of this guide. The individual components of the source implementation are described in the following subsections.

7.2.1 Neutron monochromator

As it has been shown in the previous chapters the main contribution to the UCN production requires only a narrow range of wavelengths around 8.9 Å. Using a monochromator and a secondary guide strongly reduces the background with respect to a converter placed in the direct, white beam. The price to be paid is a reduction in intensity due to imperfection of monochromator and secondary guide, and due to omission of multi-phonon processes [Bak03, Sch08b].

Crystal monochromators reflect neutrons of the desired wavelengths away from the primary beam under the d-spacing dependent Bragg angle:

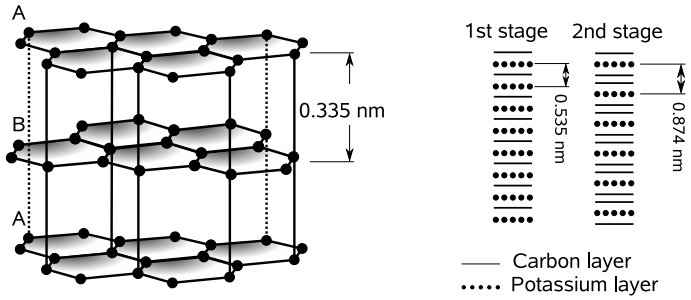

Figure 7.2: Crystal structure of graphite and staging of GiC. The intercalant diffuses into the graphite and thus increases the lattice spacing. Different stages of GiC can be produced. The stage number refers to the number of unperturbed graphite layer between two layers of intercalant atoms.

$$\theta_{\mathrm{B}} = \arcsin\left(\frac{n\lambda}{2d}\right). \tag{7.1}$$

The d-spacing of a monochromator for $\lambda = 8.9$ Å has to be $d > \lambda/2 = 4.45$ Å. In a perfect single crystal the line width for Bragg reflected neutrons is extremely small, $\Delta k/k = 10^{-4}$ [Gol47] leading to a very narrow acceptance angle of incident neutrons:

$$\frac{\Delta k}{k} = \cot\theta \Delta\theta. \tag{7.2}$$

The incident beam has a divergence of typically $\pm 2°$ at 8.9 Å due to the $m = 2$ supermirrors used in the guide. Therefore a "mosaic crystal" [Gol47] is used. Such a crystal can be regarded as a collection of microscopically small perfect crystals with differing angles ϵ with respect to the overall crystal orientation. Although the angular distribution is in general arbitrary, it resembles a cylindrically symmetric Gaussian distribution with a width η, called the mosaicity. To obtain a high acceptance the mosaicity should be in the range of the divergence of the incident beam [Lis94]. A high reflectivity of the crystal for 8.9 Å neutrons is required, too. Mica and graphite intercalated compounds (GiC) with alkali metals both match the requirements for the lattice spacing. However, due to the too small mosaicity $\approx 0.3°$ of mica we are using a potassium-intercalated graphite monochromator of the type already employed at the ILL[1] and NIST [Boe83, Mat04]. For highly oriented pyrolytic graphite, $d = 3.35$ Å with a typical mosaicity of $1° - 2°$. The d-spacing is increased by placing guest species in between graphite layers (see Fig. 7.2). This process is called intercalation.

Alkali intercalated graphite compounds are conveniently produced using the

[1]Instrument DB21: A low resolution biological diffractometer http://www.ill.eu/db21/

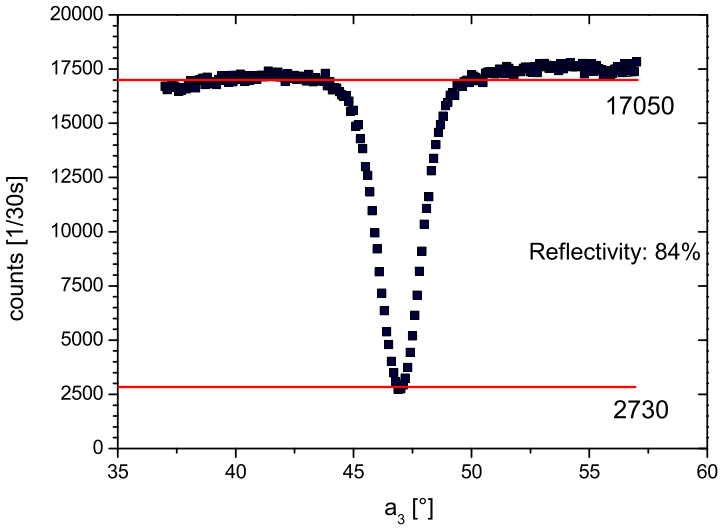

Figure 7.3: Reflectivity of a stage-2 potassioum-intercalated graphit crystal, measured in transmission with 5.9 Å neutrons on the three-axis inelastic spectrometer IN12 of the Insitut Laue Langevin.

"two-bulb" technique, where the graphite is maintained at a temperature T_c which is higher than T_a of the alkali metal [Hér55]. The stage which is formed depends on the temperature difference $\Delta T = T_c - T_a$ and the quantity of potassium available. For stage-1, stage-2 we are employing 5 g, 1 g ampoules of potassium at $T_a = 255 \pm 3$ °C and $\Delta T_1 = 10 \pm 3$ °C, $\Delta T_2 = 102 \pm 3$ °C, respectively.

The monochromator consists of 18 stage-2 potassium intercalated graphite crystals ($C_{24}K$) providing a lattice spacing of $d = 8.74$ Å giving a take-off angle of $2\theta = 61.2°$. The typical mosaic spread of the produced crystals is $\eta = 1.5° - 2.2°$ which matches the incident divergence of beam H172 at 8.9 Å. Furthermore the thermal-neutron absorption cross sections of carbon (0.0035 barn) and potassium (2.1 barn) are small. The crystals are mounted pair-wise onto graphite bars which then are screwed into an indium-sealed aluminium box. First crystals with a peak reflectivity of $r \geq 80$ % (see Fig. 7.3) have been produced.

A second monochromator with a take-off angle of $2\theta = 112.5°$ made of a set of stage-1 crystals (C_8K, $d = 5.35$ Å) will be placed close to the first one on a rotary table. The two monochromators can be interchanged making two separate 8.9 Å beam ports available at H172 (see Fig. 7.1). The second beam will feed a position for further tests and developments on liquid helium based UCN-sources, and later for the cryo-EDM experiment [v.d08].

7.2.2 Secondary neutron guide, UCN converter and cryostat

General requirements for producing a high density of UCN in a converter vessel filled with superfluid-helium are an intense incident beam, a high optical potential of the walls of the vessel, and a small loss-per-bounce coefficient μ. A converter vessel with polished, flat wall surfaces may have a better acceptance for a divergent incident beam. In Sec. 5.4 I have discussed that rough surfaces seem to support faster UCN extraction better compared to polished ones [Zim08], which is interesting especially for short sources. A converging secondary neutron guide may increase the flux density of 8.9 Å neutrons at the entrance to the converter. However, the increased divergence might result in a strong decrease of flux density along the converter for rough and/or low-Fermi-potential walls.

Monte Carlo simulations were performed to investigate UCN production for various guide geometries and wall properties (see Fig. 7.4). Taking into account also other constraints we decided to employ a 1 m long assembly of 5 rectangular BeO tubes, closed at the entrance and the exit of the cold beam by 1 mm thick Be foils, thus taking advantage of the high Fermi potential of these materials (261 neV and 252 neV, respectively). The flux incident on the monochromator at 8.9 Å, $\mathrm{d}\Phi/\mathrm{d}\lambda|_{\lambda^*} = 6 \cdot 10^8 \mathrm{s}^{-1}\mathrm{cm}^{-2}\text{Å}^{-1}$, was calculated from known cold-source data and a transmission simulation for the existing guide. The peak reflectivity of ≥ 80 % of the monochromator corresponds to an integral reflectivity of ~ 50 % for the divergent 8.9 Å beam. The neutron guide between monochromator and source converges over a length of 4.5 m from a $80 \times 80\mathrm{mm}^2$ to the cross section indicated in Fig. 7.4.

The simulations, made with "complicated guide"[2], show that, for a conversion volume with the properties defined above, with a cross section of $70{\times}70$ mm^2 and taking $\mu = 1 \cdot 10^{-4}$, we expect an UCN density of $\rho_{\mathrm{calc}} \geq 2500$ cm^{-3}. The guide between monochromator and source will therefore be build accordingly.

UCN are extracted from the converter through specular tubes into an intermediate volume (see Fig. 7.5). To suppress heat load from thermal radiation along the tube we use an UCN shutter thermally anchored to the 4 K screen of the cryostat. The intermediate volume, at room temperature, is equipped with a second UCN shutter at the entrance. Both shutters are operated in sequential mode to establish and maintain a high UCN density inside the intermediate volume. The UCN yield of our cold window-free, vertical UCN extraction is much improved with respect to an older scheme with horizontal UCN extraction through foils [Kil87]. In this early trial the extraction efficiency was very low which probably was caused by freezing out of gas on the

[2] A ray trace Monte Carlo code developed and maintained by Ken H. Andersen.

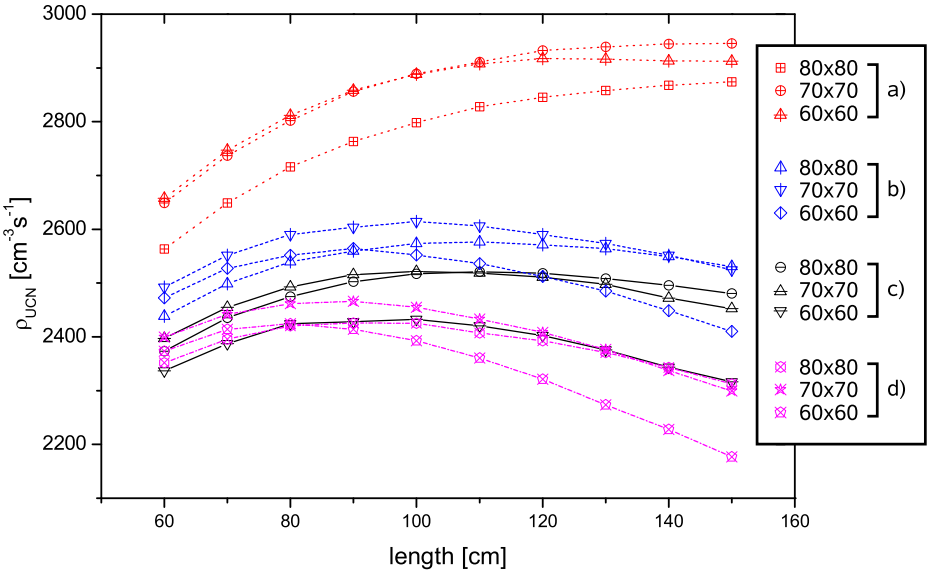

Figure 7.4: Simulation of UCN-density as a function of length and cross section of the conversion volume, for four different combinations of wall coatings of guide and conversion volume: a) m=2 side walls and m=3 top and bottom wall of guide, m=2 conversion volume; b) m=3 guide, m=1 conversion volume; c) m=3 guide, m=0 conversion volume; d) m=2 side walls and m=3 top and bottom wall of guide, m=0 conversion volume. The beam after the monochromator is taken to have a Gaussian divergence $\alpha = 1.8°$ and a differential flux of $\mathrm{d}\Phi/\mathrm{d}\lambda|_{\lambda^*} = 3 \cdot 10^8$ cm^{-2}s^{-1} Å^{-1}. The higher the m-value the higher the density, but the gain for a volume of 100 cm length is negligible. However, the combination of a high m-value and an increased length of the conversion volume increases the density.

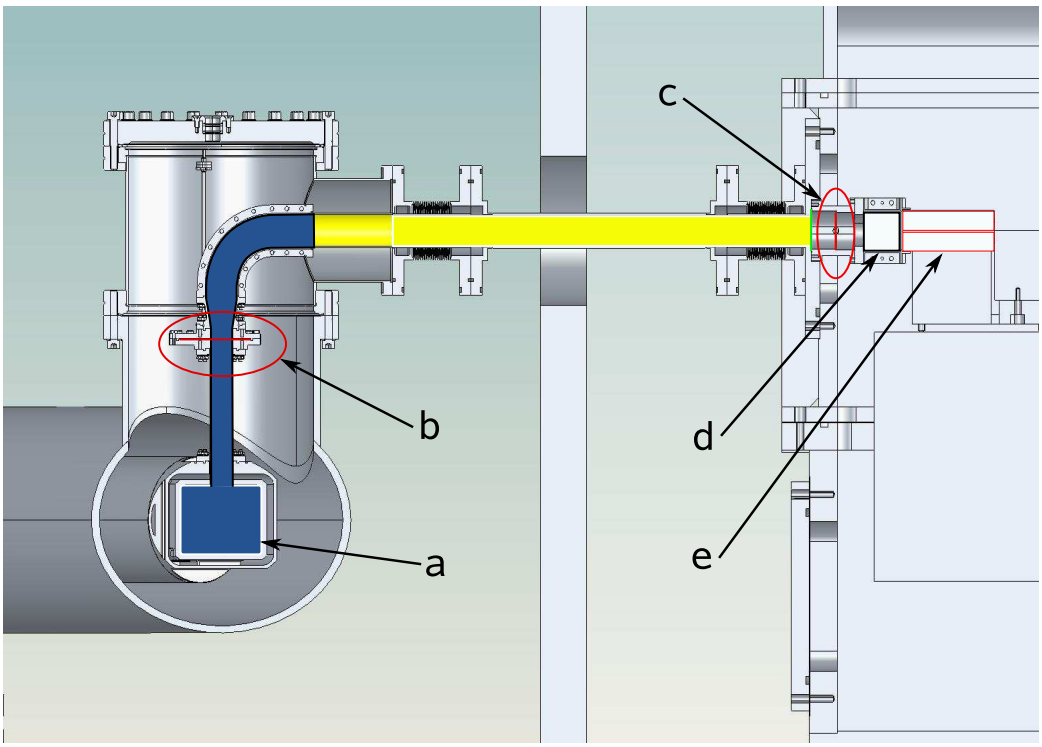

Figure 7.5: Drawing of the UCN extraction system: a – UCN production volume (cut), b – cold UCN shutter, c – room temperature UCN shutter, d – intermediate volume, e – semidiffuse channel. The cold part of the extraction system is marked in blue, the room-temperature part in yellow.

cold foils. A bent in the extraction guide reduces background from directly scattered cold neutrons. For filling and cooling the converter volume with liquid helium we employ the cryostat described in Chapter 5.

7.2.3 UCN selection with semidiffuse channel

The first experiments with the gravitational spectrometer GRANIT require a quasi-continuous flux of UCN within a narrow phase space element, for which a special UCN extraction system has been developed. UCN from the converter are guided to the intermediate volume by a highly polished nickel or diamond-like carbon (DLC) coated guide (Fig. 7.5). The intermediate volume is made of rough DLC-coated aluminium plates, providing mixing in the phase space of stored neutrons. The optimum size of the volume was determined by simulations with Geant4UCN [Atc05b] to be 40×40 mm^2, the length 300 mm is given by the dimensions of the spectrometer.

UCN are extracted from the intermediate volume via a narrow horizontal semidiffuse extraction channel described in [SW07, Bar08]. Measurements have shown that such a channel increases the storage time inside the inter-

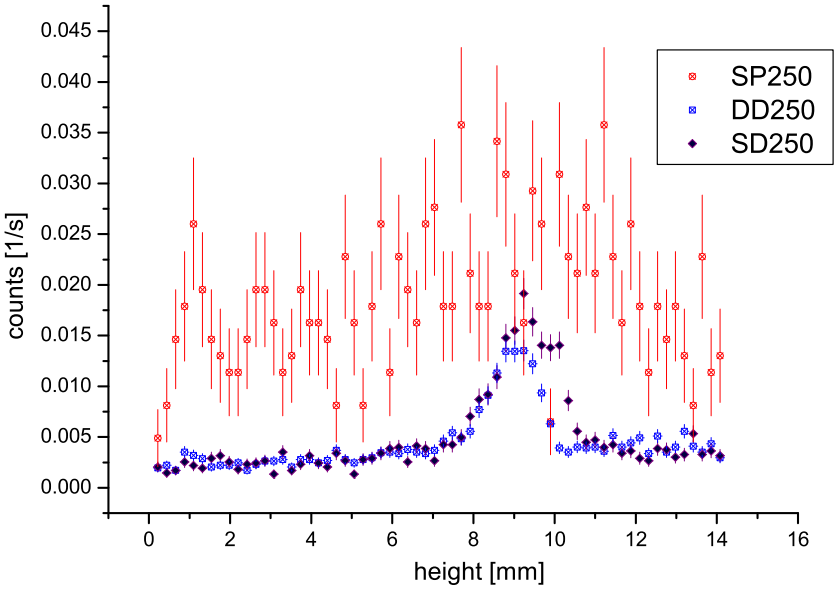

Figure 7.6: Transmission through channels with height $h = 250$ μm, length $l = 30$ mm and width $w = 61$ mm measured with a high resolution UCN detector (pixel size: $55 \times 55 \mu m^2$) [Jak08]. The integral transmission with two mirror like surfaces (**SP**) is a factor 5 bigger than with two rough surfaces (**DD**) inside the channel. In a configuration with a mirror like surface on bottom and a rough surface on top (**SD**) all desired quantum states can pass into the spectrometer.

mediate volume since more than 80% of the neutrons incident on the channel are reflected back. These neutrons are lost in conventional collimation systems whereas they increase the UCN density here and in turn the flux of extracted neutrons.

The phase-space selectivity of the extraction channel is demonstrated in Fig. 7.6. For GRANIT it will be made of DLC coated quartz plates, with the lower surfaces polished, and the upper ones rough. The channel dimensions are $h = 200$ μm, $l = 100$ mm, $w = 300$ mm. We expect a reflectivity $r \geq 80$ % for neutrons with a vertical energy component $E_\perp \geq mgh = 20$ peV with respect to the surface of the bottom mirror.

7.3 Outlook

Prototypes of monochromator crystals, the converter, and the semidiffuse channel have all been tested separately. The design of the full setup is finalised, and the components are being produced. Calculations with an

incident differential flux $\mathrm{d}\Phi/\mathrm{d}\lambda|_{\lambda^*} = 6 \cdot 10^8$ $\mathrm{s}^{-1}\mathrm{cm}^{-2}\,\mathrm{Å}^{-1}$ on the monochromator give a UCN density of $\rho_{\mathrm{UCN}} \approx 2500$ cm^{-3} in the converter and up to $\rho_{\mathrm{int}} = 800$ cm^{-3} in the intermediate volume. This yields an available phase-space density of $\Gamma_{\mathrm{He}} \approx 0.2$ $\mathrm{cm}^{-3}(\mathrm{m/s})^{-3}$ for the critical velocity of 7 m/s of the used materials. Compared to the phase-space density $\Gamma_{\mathrm{Turbine}} \approx 0.013$ $\mathrm{cm}^{-3}(\mathrm{m/s})^{-3}$ of the UCN turbine at the ILL this is more than a factor ten of improvement. This calculation assumes perfect conditions and in all parts optimal transmissions. The integration of source, intermediate volume and extraction channel is a challenging task, and further optimisation may be needed to approach the calculated densities.

Chapter 8

Summary and outlook

In this theses cold neutron to ultracold neutron conversion in superfluid helium at various pressures has been investigated. Two different approaches have been chosen: firstly, the derivation of UCN production rates from inelastic neutron scattering data; secondly, the direct measurement of these on an intense cold neutron beam.

In a first experiment at the "Neutronenquelle Heinz Maier-Leibnitz" it was shown that an efficient extraction of UCN from a superfluid helium at saturated vapour pressure is achievable – a prerequisite for the second experiment and for future experiments with UCN in vacuum. An extraction efficiency of ~ 40 % was realised with electropolished stainless steel tubes. This value can be further improved if an extraction system with highly specular surface coatings is employed.

The same cryostat and experimental setup, modified to withstand pressures up to 30 bar, was then used at the Institut Laue Langevin to measure the wavelength-dependent UCN production rate at SVP and $p = 6, 11, 16, 20$ bar. The results from these measurement in general agree very good with the prediction made from inelastic neutron scattering data. The single-phonon peak moves to higher incident wavelength and decreases in intensity with pressure. The multiphonon range does not change within the presicion of the taken data. However, a discrepancy in absolut positions of the curves sremains most probably resulting from the wavelength calibration. The positions of measured to predicted single-phonon peaks at all pressures is displaced by ~ 0.23 Å.

These observations lead to the conclusion that UCN production in superfluid helium on a typical polychromatic cold neutron beam does most likely not increase with pressure, a result which agrees with the predictions from neutron inelastic scattering data. For a cold neutron spectrum similar to the one of PF1b it is not attractive to use superfluid helium under pressure as ultracold neutron converter. The integral production rate for a source at

PF1b decreases from 13.9(9) $cm^{-3}s^{-1}$ for SVP to 11.1(8) $cm^{-3}s^{-1}$ at 20 bar. Furthermore, the up-scattering rate will increase with pressure, reducing the UCN storage time and density.

A more promising strategy to further improve UCN sources based on He-II is the use of the entire cold neutrons spectrum and magnetic storage. In the outline of the new source designed for the gravitational spectrometer GRANIT I estimate a UCN density of $\rho_{\mathrm{UCN}} \approx 2500\ cm^{-3}$. This value quadruples considering the contributions from multiphonons and the omission of the monochromator. With a conversion vessel made from a magnetic multipol the UCN storage time and therefore the UCN density will increase further. The loss of a factor 2 due to the storage of only one spin state can is of no importants for most experiments.

For future investigations of potential UCN converters I strongly emphasis the prior use of classical neutron scattering techniques or the dedicated reanalysis of existing data. This is of even greater importance in non-liquid converters like solid helium or solid oxygen where crystal orientation and temperature dependent lattice types play a important role.

List of Figures

2.1 Phase diagram of ^{4}He. 11

2.2 Phonon–roton dispersion relation of superfluid helium 12

2.3 Scattering diagrams for single phonon absorption, phonon absorption and reemission, and roton absorption and phonon emission. 17

3.1 Sketch of triple-axis spectrometer 22

3.2 Sketch of time-of-flight spectrometer 23

3.3 $(\boldsymbol{q} - E)$ range of IN6 24

3.4 Dynamic scattering function of He-II at 10 bar 25

3.5 $S(q, \hbar\omega)$ for $q = 0.90$ Å^{-1} and $q = 0.95$ Å^{-1} 26

3.6 Slices of $S(q, \omega)$ for $q = \sqrt{2m_\mathrm{n} \cdot \omega/\hbar}$, at 0.5 K. 27

3.7 Intersection of the free neutron dipsersion relation $E_\mathrm{n}(k_\mathrm{i})$ with dispersion curves of superfluid helium $E_\mathrm{He}(q)$ at 0.5 K and $p = \mathrm{SVP}, 5, 10, 15$ bar and 20 bar. 28

3.8 Multiphonon scattering functions $s_\mathrm{II}(\lambda)$. 31

3.9 Temperature dependence of the scattering function $s_(\lambda)$. . . . 33

4.1 Sketch of the cryogenic system of the prototype cryostat. . . . 37

4.2 Overall view of the prototype cryostat at the LN1 beam line of the “Neutronenquelle Heinz Maier-Leibnitz”. 38

4.3 Simplified sketch of the cryostat with converter volume and extraction chimney. 44

4.4 Flowchart of ^{3}He cycle. 45

4.5 Heat exchanger inside the ^{3}He evaporation stage. 46

4.6 Sketch of superleak and cold switch. 47

4.7 Typical cooldown and continuous operation of the prototype cryostat. 48

5.1 Schematic view of the setup for experiments on UCN extraction. 51

5.2 Photograph of converter vessel parts. 52

5.3 Differential cold neutron fluxes. 53

5.4 Typical "build-up" measurement here at 1.26 K. The red lines are fits of exponential decays to the emptying curves. 54

5.5 Continuous extraction of UCN for five different temperatures. 55

5.6 Integral UCN counts as a function of holding time t_{h} at 0.82 K. 56

5.7 Total number of UCN after the accumulation for a time t_{i}, for different temperatures. 59

5.8 Emptying time parameter τ_{e} as a function of irradiation time t_{i}. 61

5.9 Dependence of storage time on temperature T of the converter and comparison with theory. 62

6.1 Sketch of the experimental setup for measurements of pressure dependent UCN production rates. 70

6.2 Sketch of the Dornier velocity selector. 72

6.3 Sketch and photographs of the the conversion vessel. 75

6.4 Sketch of time-of-flight chopper. 77

6.5 Pulse height spectra of neutron detectors. 79

6.6 Sketch of beam profile measurement. 81

6.7 Beam profile measurements at the exit of the beam monitor for velocity selector speeds $f = 15600$ rpm and 28300 rpm. . . 82

6.8 Raw data from time-of-flight measurements for the two chopper angular settings. 84

6.9 Determination of time offset t_0 from changing the length of the flight path. 85

6.10 Typical change in temperature during one individual measurement (SVP 31-Sep-2008). The discrete step is caused by the resolution of the data acquisition. The typical accuracy at this temperature is 5 mK. 85

6.11 Typical change in temperature during an entire scan for some selected pressures and for examples from both wavelength ranges. 86

6.12 UCN detection vs. time for a typical individual measurement. 88

6.13 Background deduced from "hot" measurement. 90

6.14 Estimation for CN-flux dependent background. 93

6.15 Temporal decrease in single-phonon peak count rate at SVP. . 94

6.16 Control measurements of the peak area at saturated vapour pressure. 95

6.17 ToF spectra before and after deconvolution. 98

6.18 Decrease in intensity of the prominent peak of the UCN production rates with pressure for SVP (□) and $p = 6\,(\bigcirc), 11\,(\boxplus), 16\,(\oplus)$ bar, and 20 (⊠) bar. 99

6.19 Comparison of measured and calculated differential UCN production rates. 100

6.20 Comparison of measured and calculated differential UCN rates with fine tuned ToF parameters to match positions of single-phonon peaks at SVP and 20 bar. 103

7.1 Setting of the monochromator, the source, and GRANIT inside level C of the ILL. 105

7.2 Crystal structure of graphite and staging of GiC. 106

7.3 Reflectivity of a stage-2 potassioum-intercalated graphit crystal, measured in transmission with 5.9 Å neutrons on the three-axis inelastic spectrometer IN12 of the Insitut Laue Langevin. 107

7.4 Simulation of UCN-density as a function of length and cross section of the conversion volume, for four different combinations of wall coatings of guide and conversion volume. 109

7.5 Drawing of the UCN extraction system. 110

7.6 Transmission through channels with height $h = 250$ μm measured with a high resolution UCN detector 111

List of Tables

2.1 Neutron temperatures. 8

2.2 Pressure dependence of helium parameters. 13

3.1 Pressure dependence of single phonon production rate parameters 29

3.2 Calculated UCN production rates from multiphonon processes with the cold neutron spectrum from PF1b. 32

3.3 Fitting parameters of phenomenological expression for s_{II} . . . 32

3.4 Pressure dependence of first velocity of sound, Grüneisen constant, and Landau parameters. 35

5.1 UCN build up time, full data range. 60

5.2 UCN build up time, reduced data range. 60

5.3 Parameters for continuous measurements with fomblin coated converter bottle. 63

5.4 Production rates deduced with both methods. 64

6.1 Calculated wavelength ranges and resolutions accessible with rotation speeds between 15600 and 28300 rpm. 73

6.2 Comparison of neutron fluxes from gold foil activation and the corresponding monitor values. 82

6.3 List of all wavelength-resolved conversion rate measurements. . 88

6.4 Pressure dependence of single-phonon peak position and intensity. 97

6.5 Measured and calculated UCN production rates for SVP, and $p = 6, 11, 16, 20$ bar. 101

Bibliography

[Abe01] Y. Abe and N. Morishima. Quantitative evaluation of ultracold neutron production and storage in superfluid helium. *Nuclear Instruments and Methods in Physics Research A* **463**, 293–298 (May 2001).

[Abe06] H. Abele, D. Dubbers, H. Häse, M. Klein, A. Knöpfler, M. Kreuz, T. Lauer, B. Märkisch, D. Mund, V. Nesvizhevsky, A. Petoukhov, C. Schmidt, M. Schumann, and T. Soldner. Characterization of a ballistic supermirror neutron guide. *Nuclear Instruments and Methods in Physics Research A* **562**, 407–417 (June 2006).

[Abr70] B. M. Abraham, Y. Eckstein, J. B. Ketterson, M. Kuchnir, and P. R. Roach. Velocity of sound, density, and Grüneisen constant in liquid He-4. *Phys. Rev. A* **1**(2), 250–257 (Feb 1970).

[Age78] P. Ageron, W. Mampe, R. Golub, and J. M. Pendelbury. Measurement of the ultra cold neutron production rate in an external liquid helium source. *Physics Letters A* **66**, 469–471 (June 1978).

[Age89] P. Ageron. Cold neutron sources at ILL. *Nuclear Instruments and Methods in Physics Research A* **284**, 197–199 (November 1989).

[And96] K. H. Andersen, J. Bossy, J. C. Cook, O. G. Randl, and J.-L. Ragazzoni. High-Resolution Measurements of Rotons in He-4. *Physical Review Letters* **77**, 4043–4045 (November 1996).

[Arz00] S. Arzumanov, L. Bondarenko, S. Chernyavsky, W. Drexel, A. Fomin, P. Geltenbort, V. Morozov, Y. Panin, J. Pendlebury, and K. Schreckenbach. Neutron life time value measured by storing ultracold neutrons with detection of inelastically scattered neutrons. *Physics Letters B* **483**, 15–22 (June 2000).

[Atc05a] F. Atchison, B. Blau, K. Bodek, B. van den Brandt, T. Brys, F. Chapuis, M. Daum, P. Fierlinger, A. Fuchs, P. Geltenbort, D. George, W. Gloor, S. Grigoriev, P. Hautle, U. Heidelberger, G. Heidenreich, F. Heinrich, R. Henneck, S. Heule, Th. Hofmann, M. Horvat, F. Jenni, St. Joray, R. Kaech, M. Kasprzak, K. Kirch,

S. Kistryn, K. Kohlik, J. Kohout, J. A. Konter, G. Kotrle, G. Khne, M. Kuzniak, R. Maag, I. Mironov, H. Obermeier, Ch. Perret1, A. Pichlmaier, Ch. Plonka, R. Reiser, U. Rohrer, U. Sigrist, S. Staudenmann, P. Suter, H. Spitzer, J. Ulrich, M. Wohlmuther, S. Zelenika, J. Zmeskal, G. Zsigmond, and J. Zuellig. The PSI UCN source. In *ICANS-XVII, Santa Fe* (2005).

[Atc05b] F. Atchison, T. Bryś, M. Daum, P. Fierlinger, A. Fomin, R. Henneck, K. Kirch, M. Kuźniak, and A. Pichlmaier. The simulation of ultracold neutron experiments using GEANT4. *Nuclear Instruments and Methods in Physics Research A* **552**, 513–521 (November 2005).

[Bae07] S. Baeßler, V. V. Nesvizhevsky, K. V. Protasov, and A. Y. Voronin. Constraint on the coupling of axionlike particles to matter via an ultracold neutron gravitational experiment. *Physical Review D* **75**(7), 075006–+ (April 2007).

[Bae08] S Baeßler *et al. submitted to NIM A* (2008).

[Bak03] C. A. Baker, S. N. Balashov, J. Butterworth, P. Geltenbort, K. Green, P. G. Harris, M. G. D. van der Grinten, P. S. Iaydjiev, S. N. Ivanov, J. M. Pendlebury, D. B. Shiers, M. A. H. Tucker, and H. Yoshiki. Experimental measurement of ultracold neutron production in superfluid ^4He. *Physics Letters A* **308**, 67–74 (February 2003).

[Bak06] C. A. Baker, D. D. Doyle, P. Geltenbort, K. Green, M. G. D. van der Grinten, P. G. Harris, P. Iaydjiev, S. N. Ivanov, D. J. R. May, J. M. Pendlebury, J. D. Richardson, D. Shiers, and K. F. Smith. Improved Experimental Limit on the Electric Dipole Moment of the Neutron. *Physical Review Letters* **97**(13), 131801–+ (September 2006).

[Bar08] J. Barnard and V. Nesvizhevsky. Analysis of a method for extracting angularly collimated UCNs from a volume without losing the density inside. *Nuclear Instruments and Methods in Physics Research A* **591**, 431–435 (June 2008).

[Bed84] K. Bedell, D. Pines, and A. Zawadowski. Pseudopotential theory of interacting roton pairs in superfluid ^{4}He. *Phys. Rev. B* **29**(1), 102–122 (Jan 1984).

[Bod08] K. Bodek, M. Daum, R. Henneck, S. Heule, M. Kasprzak, K. Kirch, A. Knecht, M. Kuźniak, B. Lauss, M. Meier, G. Petzoldt, M. Schneider, and G. Zsigmond. Storage of ultracold neutrons in high resistivity, non-magnetic materials with high Fermi

potential. *Nuclear Instruments and Methods in Physics Research A* **597**, 222–226 (December 2008).

[Boe83] A. Boeuf, A. Freund, R. Caciuffo, A. Hamwi, and P. Touzain. Intercalated pyrolytic graphite for neutron monochromatisation. *Synthetic Metals* **8**, 307 (1983).

[Cau08] F. Caupin, J. Boronat, and K. H. Andersen. Static Structure Factor and Static Response Function of Superfluid Helium 4: a Comparative Analysis. *Journal of Low Temperature Physics* **152**, 108–121 (April 2008).

[Coh57] M. Cohen and R. P. Feynman. Theory of Inelastic Scattering of Cold Neutrons from Liquid Helium. *Physical Review* **107**, 13–24 (July 1957).

[Die72] O. W. Dietrich, E. H. Graf, C. H. Huang, and L. Passell. Neutron Scattering by Rotons in Liquid Helium. *Physical Review AS* **5**, 1377–1391 (March 1972).

[Fam75] Fereydoon Family. Sum rules and high-frequency behavior of dynamic structure function of quantum fluids. *Phys. Rev. Lett.* **34**(22), 1374–1377 (Jun 1975).

[Flü71] S. Flügge. *Practical Quantum Mechanics*, volume 1. Springer-Verlag, Berlin (1971).

[Fre07] A. Frei, Y. Sobolev, I. Altarev, K. Eberhardt, A. Gschrey, E. Gutsmiedl, R. Hackl, G. Hampel, F. J. Hartmann, W. Heil, J. V. Kratz, T. Lauer, A. Liźon Aguilar, A. R. Müller, S. Paul, Y. Pokotilovski, W. Schmid, L. Tassini, D. Tortorella, N. Trautmann, U. Trinks, and N. Wiehl. First production of ultracold neutrons with a solid deuterium source at the pulsed reactor TRIGA Mainz. *European Physical Journal A* **34**, 119–127 (November 2007).

[Fri89] H. Friedrich, V. Wagner, and P. Wille. A high-performance neutron velocity selector. *Physica B Condensed Matter* **156**, 547–549 (January 1989).

[Gib96] M. R. Gibbs. *The collective excitations of superfluid ^{4}He: The dependence on pressure and the effect of restricted geometry.* PhD thesis, Keele University (1996).

[Gib99] M. R. Gibbs, K. H. Andersen, W. G. Stirling, and H. Schober. The collective excitations of normal and superfluid He4: the dependence on pressure and temperature. *Journal of Physics Condensed Matter* **11**, 603–628 (January 1999).

[Gib00] M. R. Gibbs, W. G. Stirling, K.H. Andersen, and Schober. Pressure dependence of the multiphonon excitations of superfluid ^{4}He. *J. of Low Temp. Phys.* **120**, 55 (2000).

[Gly95] H. Glyde. *Excitations in liquid and solid helium.* Oxford University Press (1995).

[Gol47] M. L. Goldberger and F. Seitz. Theory of the Refraction and the Diffraction of Neutrons by Crystals. *Physical Review* **71**, 294–310 (March 1947).

[Gol75] R. Golub and J. M. Pendlebury. Super-thermal sources of ultra-cold neutrons. *Physics Letters A* **53**, 133–135 (June 1975).

[Gol77] R. Golub and J. M. Pendlebury. The interaction of Ultra-Cold Neutrons (UCN) with liquid helium and a superthermal UCN source. *Physics Letters A* **62**, 337–339 (September 1977).

[Gol79a] R. Golub. Lifetime of a Neutron at rest in pure Helium 4. technical report 79GO25T, ILL (1979).

[Gol79b] R. Golub. On the storage of neutrons in superfluid ^{4}He. *Physics Letters A* **72**, 387–390 (July 1979).

[Gol91] R. Golub, D.J. Richardson, and S.K. Lamoreaux. *Ultra-Cold Neutrons.* Adam Hilger, Bristol, Philadelphia, and New York (1991).

[Hér55] A. Hérold. Recherches sur les composés d'insertion du graphite. *Bull. Soc. Chim. Fr.* 5^e **série**, 999 (1955).

[Ign90] V.K. Ignatovich. *The Physics of Ultracold Neutrons.* Clarendon, Oxford (1990).

[Jak08] J. Jakubek, P. Schmidt-Wellenburg, P. Geltenbort, M. Platkevic, C. Plonka-Spehr, J. Solc, and T. Soldner. *Nucl. Instr. and Meth. in Phys. Res. A* page doi:10.1016/j.nima.2008.12.078 (2008).

[Kel98] T. Keller, R. Golub, F. Mezei, and R. Gähler. A neutron resonance spin-echo spectrometer (NRSE) with tiltable fields. *Physica B Condensed Matter* **241**, 101–103 (April 1998).

[Kel04] T. Keller, K. Habicht, R. Golub, and F. Mezei. Roton and phonon linewidths in superfluid ^{4}He. *Europhysics Letters* **67**, 773–778 (September 2004).

[Kil87] A. I. Kilvington, R. Golub, W. Mampe, and P. Ageron. Scattering of ultra-cold neutrons (UCN) by superfluid helium at temperatures around 1 K. *Physics Letters A* **125**, 416–420 (November 1987).

[Kor02] E. Korobkina, R. Golub, B. W. Wehring, and A. R. Young. Production of UCN by downscattering in superfluid He-4. *Physics Letters A* **301**, 462–469 (September 2002).

[Kre08] M. Kreuz, V. V. Nesvizhevsky, P. Schmidt-Wellenburg, T. Soldner, M. Thomas, H. G. Börner, F. Naraghi, G. Pignol, K. V. Protasov, D. Reybreyend, F. Vezzu, J. M., L. Flaminio, C. Michel, L. Pinard, A. Remillieux, S. Baeßler, A. M. Gagarski, L. A. Grigorieva, A. M. Kuzmina, A. E. Meyerovich, L. P. Mezhov-Deglin, G. A. Petrov, A. V. Strelkov, and A. Yu. Voronin. A method to measure the resonance transitions between the gravitationally bound quantum states of neutrons in the GRANIT spectrometer. *accepted by NIM A* (2008).

[Lan41] L. Landau. Theory of the Superfluidity of Helium II. *Physical Review* **60**, 356–358 (August 1941).

[Lan49] L.D. Landau and I.M. Khalatnikov. The theory of the viscosity of helium II: I. Collisions of elementary excitations in helium II. *JETP* page 637 (1949).

[Leu08] K. Leung. *privat communication* (2008).

[Lis94] K.-D. Liss and A. Magerl. Can a gradient crystal compete with a mosaic crystal as a monochromator in neutron- or X-ray diffraction? *Nuclear Instruments and Methods in Physics Research A* **338**, 90–98 (January 1994).

[Liu98] C.-Y. Liu, G. D. Cates, A. R. Young, P. Geltenbort, T. J. Bowles, G. Greene, R. E. Hill, S. K. Lamoreaux, C. L. Morris, S. J. Seestrom, A. Garcia, R. B. Vogelaar, and B. Fujikawa. A Solid Deuterium Superthermal Source of Ultra-Cold Neutrons Coupled to Spallation Targets at LANSCE. *APS Meeting Abstracts* pages 210–+ (October 1998).

[Lon54] F. London. *Superfluids*, volume 2 (1954).

[Lov84] S.W. Lovesey. *Theory of neutron scattering from condensed matter*. Oxford University Press (1984).

[Lus69] V. I. Luschikov, Pokotilovsky Yu. N., Strelkov A. V., and Shapiro F. L. Observation of Ultracold Neutrons. *JETP Letters* **9**, 23–26 (January 1969).

[Lus78] V. I. Luschikov and A. I. Frank. Quantum effects occurring when ultracold neutrons are stored on a plane. *JETP Lett.* **28**, 559–+ (November 1978).

[Mam89] W. Mampe, P. Ageron, C. Bates, J. M. Pendlebury, and A. Steyerl. Neutron lifetime measured with stored ultracold neutrons. *Phys. Rev. Lett.* **63**(6), 593–596 (Aug 1989).

[Mar73] Humphrey J. Maris. Hydrodynamics of superfluid helium below 0.6 k. ii. velocity and attenuation of ultrasonic waves. *Phys. Rev. A* **8**(5), 2629–2639 (Nov 1973).

[Mar77] H. J. Maris. Phonon-phonon interactions in liquid helium. *Reviews of Modern Physics* **49**, 341–360 (April 1977).

[Mas02] Y. Masuda, T. Kitagaki, K. Hatanaka, M. Higuchi, S. Ishimoto, Y. Kiyanagi, K. Morimoto, S. Muto, and M. Yoshimura. Spallation Ultracold-Neutron Production in Superfluid Helium. *Physical Review Letters* **89**, B4801+ (December 2002).

[Mat04] C. E. H. Mattoni, C. P. Adams, K. J. Alvine, J. M. Doyle, S. N. Dzhosyuk, R. Golub, E. Korobkina, D. N. McKinsey, A. K. Thompson, L. Yang, H. Zabel, and P. R. Huffman. A long wavelength neutron monochromator for superthermal production of ultracold neutrons. *Physica B Condensed Matter* **344**, 343–357 (February 2004).

[Mez80] F. Mezei. High-resolution study of excitations in superfluid *he*4 by the neutron spin-echo technique. *Phys. Rev. Lett.* **44**(24), 1601–1604 (Jun 1980).

[Mez91] F. Mezei, B. Farago, and C. Lartigue. *Excitations in Two-Dimensional and Three-Dimensional Quantum Fluids*, volume 257 of *NATO ASI Ser. B.* Plenum, New York (1991).

[Mil62] Allen Miller, David Pines, and Philippe Nozières. Elementary excitations in liquid helium. *Phys. Rev.* **127**(5), 1452–1464 (Sep 1962).

[Nes02] V. V. Nesvizhevsky, H. G. Börner, A. K. Petukhov, H. Abele, S. Baeßler, F. J. Rueß, T. Stöferle, A. Westphal, A. M. Gagarski, G. A. Petrov, and A. V. Strelkov. Quantum states of neutrons in the Earth's gravitational field. *Nature* **415**, 297–299 (January 2002).

[Nes03] V. V. Nesvizhevsky, H. G. Börner, A. M. Gagarski, A. K. Petoukhov, G. A. Petrov, H. Abele, S. Baeßler, G. Divkovic, F. J. Rueß, T. Stöferle, A. Westphal, A. V. Strelkov, K. V. Protasov, and A. Y. Voronin. Measurement of quantum states of neutrons in the Earth's gravitational field. *Physical Review D* **67**(10), 102002–+ (May 2003).

[Nes06] V. V. Nesvizhevsky and K. V. Protasov. *Quantum states of neutrons in the earth's gravitational field: state of the art, application, perspective, in: D.C. Moore, Trends in quantum gravity search.* Nova Science Publishers, New York (2006).

[Pen82] M. Pendlebury. *internal note* (1982).

[Pig07] G. Pignol, K. V. Protasov, D. Rebreyend, F. Vezzu, V. V. Nesvizhevsky, A. K. Petukhov, H. G. Börner, T. Soldner, P. Schmidt-Wellenburg, M. Kreuz, D. Forest, P. Ganau, J. M. Mackowski, C. Michel, J. L. Montorio, N. Morgado, L. Pinard, A. Remillieux, A. M. Gagarski, G. A. Petrov, A. M. Kusmina, A. V. Strelkov, H. Abele, S. Baeßler, and A. Y. Voronin. GRANIT project: a trap for gravitational quantum states of UCN. *ArXiv e-prints 0708.2541* (August 2007).

[Pla54] G. Placzek and L. van Hove. Crystal Dynamics and Inelastic Scattering of Neutrons. *Physical Review* **93**, 1207–1214 (March 1954).

[Pok03] Y. N. Pokotilovski. Investigation of liquid fluoropolymers as possible materials for low-temperature liquid-wall chambers for ultracold neutron storage. *Soviet Journal of Experimental and Theoretical Physics* **96**, 172–179 (February 2003).

[Rah62] A. Rahman, K. S. Singwi, and A. Sjölander. Theory of slow neutron scattering by liquids. i. *Phys. Rev.* **126**(3), 986–996 (May 1962).

[Sau04] A. Saunders, J. M. Anaya, T. J. Bowles, B. W. Filippone, P. Geltenbort, R. E. Hill, M. Hino, S. Hoedl, G. E. Hogan, T. M. Ito, K. W. Jones, T. Kawai, K. Kirch, S. K. Lamoreaux, C.-Y. Liu, M. Makela, L. J. Marek, J. W. Martin, C. L. Morris, R. N. Mortensen, A. Pichlmaier, S. J. Seestrom, A. Serebrov, D. Smith, W. Teasdale, B. Tipton, R. B. Vogelaar, A. R. Young, and J. Yuan. Demonstration of a solid deuterium source of ultra-cold neutrons. *Physics Letters B* **593**, 55–60 (July 2004).

[Sch03] W. Schott, J. M. Pendlebury, I. Altarev, S. Gröger, E. Gutsmiedl, F. J. Hartmann, S. Paul, G. Petzoldt, P. Schmidt-Wellenburg, and U. Trinks. UCN production in superfluid helium. *European Physical Journal A* **16**, 599–601 (2003).

[Sch06] P. Schmidt-Wellenburg and O. Zimmer. Helium liquefaction with a commercial 4 K Gifford-McMahon cryocooler. *Cryogenics* **46**, 799–803 (November 2006).

[Sch08a] P. Schmidt-Wellenburg, K. H. Andersen, P. Courtois, M. Kreuz, S. Mironov, V. V. Nesvizhevsky, G. Pignol, K. V. Protasov,

T. Soldner, F. Vezzu, and O. Zimmer. Ultracold-neutron infrastructure for the gravitational spectrometer GRANIT. *ArXiv e-prints 0811.1635, accepted to NIM A* (November 2008).

[Sch08b] P. Schmidt-Wellenburg, K. H. Andersen, and O. Zimmer. UCN production by multiphonon processes in superfluid Helium under pressure. *ArXiv e-prints 0811.4332, accepted by NIM A* (November 2008).

[Sea92] V.F. Sears. Neutron scattering lengths and cross sections. *Neutron News* **3**, 26 (1992).

[Ser05] A. Serebrov, V. Varlamov, A. Kharitonov, A. Fomin, Y. Pokotilovski, P. Geltenbort, J. Butterworth, I. Krasnoschekova, M. Lasakov, R. Tal'Daev, A. Vassiljev, and O. Zherebtsov. Measurement of the neutron lifetime using a gravitational trap and a low-temperature Fomblin coating. *Physics Letters B* **605**, 72–78 (January 2005).

[Sol08] T. Soldner. *privat communication* (2008).

[Ste69] A. Steyerl. Measurements of total cross sections for very slow neutrons with velocities from 100 m/sec to 5 m/sec. *Physics Letters B* **29**, 33–35 (March 1969).

[Ste75] A. Steyerl. A "neutron turbine" as an efficient source of ultracold neutrons. *Nuclear Instruments and Methods* **125**, 461–469 (April 1975).

[Ste86] A. Steyerl, H. Nagel, F.-X. Schreiber, K.-A. Steinhauser, R. Ghler, W. Glser, P. Ageron, J.M. Astruc, W. Drexel, G. Gervais, and W. Mampe. A new source of cold and ultracold neutrons. *Phys. Lett. A* **116**, 347 (1986).

[Sti94] W. G. Stirling and K. H. Andersen. Neutron scattering studies of the excitations of liquid ^{4}He . *Journal of Physics Condensed Matter* **6**, A63–A70 (June 1994).

[SW07] P. Schmidt-Wellenburg, J. Barnard, P. Geltenbort, V.V. Nesvizhevsky, C. Plonka, T. Soldner, and O. Zimmer. *Nuclear Instruments and Methods in Physics Research A* **577**, 623 (2007).

[Tor84] J.P. Torre and G. Chanin. Heat switch for liquid-helium temperatures. *Rev. Sci. Instrum.* **55(2)**, 213 (1984).

[Tri00] U. Trinks, F. J. Hartmann, S. Paul, and W. Schott. Concepts of UCN sources for the FRM-II. *Nuclear Instruments and Methods in Physics Research A* **440**, 666–673 (February 2000).

[v.d08] M v.d. Grinten. *submitted to NIM A* (2008).

[Vig66] James H. Vignos and Henry A. Fairbank. Sound measurements in liquid and solid ^{3}He, ^{4}He, and ^{3}He-^{4}He mixtures. *Phys. Rev.* **147**(1), 185–197 (Jul 1966).

[Wag92] V. Wagner, H. Friedrich, and P. Wille. Performance of a high-tech neutron velocity selector. *Physica B Condensed Matter* **180**, 938–940 (June 1992).

[Wil87] J. Wilks and D.S. Betts. *An Introduction to Liquid Helium*. Clarendon Press, London, 2. edition (1987).

[Yao06] W.-M. Yao, C. Amsler, and D. Asner *et al.* Review of Particle Physics. *Journal of Physics G* **33**, 1+ (2006).

[Yos03] H. Yoshiki. The cross sections for one phonon emission and absorption by slow neutrons in superfluid liquid helium. *Computer Physics Communications* **151**, 141 (2003).

[Zei06] K. Zeitelhack, C. Schanzer, A. Kastenmüller, A. Röhrmoser, C. Daniel, J. Franke, E. Gutsmiedl, V. Kudryashov, D. Maier, D. Päthe, W. Petry, T. Schöffel, K. Schreckenbach, A. Urban, and U. Wildgruber. Measurement of neutron flux and beam divergence at the cold neutron guide system of the new Munich research reactor FRM-II. *Nuclear Instruments and Methods in Physics Research A* **560**, 444–453 (May 2006).

[Zel59] Ya.B. Zeldovich. Cold neutron storage. *Zhur. Eksptl. i Teoret. Fiz.* **36**, 1952 (1959).

[Zim07] O. Zimmer, K. Baumann, M. Fertl, B. Franke, S. Mironov, C. Plonka, D. Rich, P. Schmidt-Wellenburg, H.-F. Wirth, and B. van den Brandt. Superfluid-Helium Converter for Accumulation and Extraction of Ultracold Neutrons. *Physical Review Letters* **99**(10), 104801–+ (September 2007).

[Zim08] O. Zimmer, P. Schmidt-Wellenburg, M. Assmann, M. Fertl, J. Klenke, S. Mironov, H. . Wirth, and B. van den Brandt. Accumulation and extraction of ultracold neutrons from a superfluid helium converter coated with fluorinated grease. *ArXiv e-prints 0801.4839* (January 2008).